

AD-A138 288

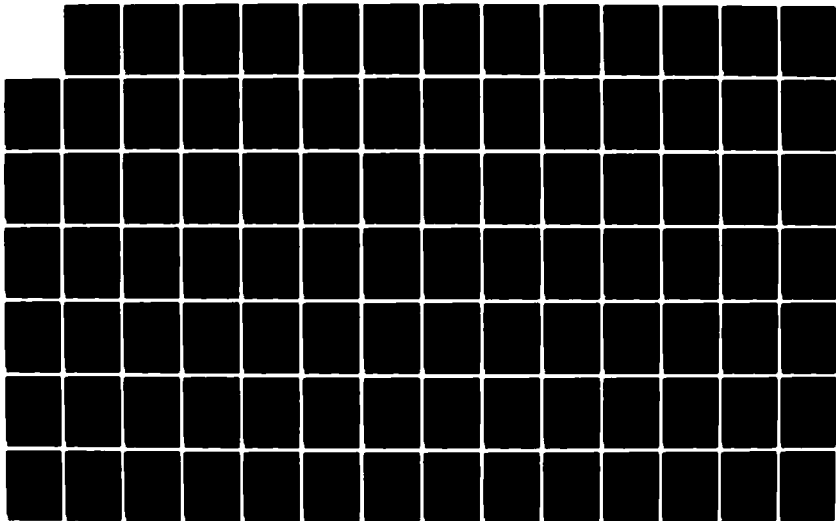
SPIRE DATA EVALUATION AND NUCLEAR IR FLUORESCENCE
PROCESSES(U) LOCKHEED MISSILES AND SPACE CO INC
SUNNYVALE CA J B KUMER ET AL. 30 NOV 82 LMSC-D913086
DNA-6237F DNA001-79-C-0033

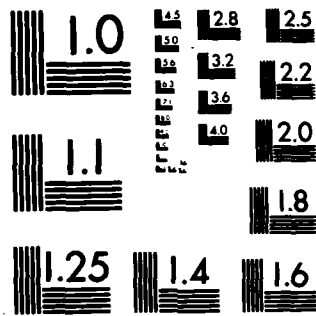
1/2

UNCLASSIFIED

F/G 18/3

NL





MICROCOPY RESOLUTION TEST CHART
NATIONAL BUREAU OF STANDARDS-1963-A

(12)

AD A138288

DNA 6237F

**SPIRE DATA EVALUATION AND NUCLEAR
IR FLUORSCENCE PROCESSES**

J. B. Kumer
T. C. James
Lockheed Missiles and Space Co., Inc.
P.O. Box 504
Sunnyvale, California 94086

30 November 1982

Final Report for Period 2 January 1979-30 November 1982

CONTRACT No. DNA 001-79-C-0033

APPROVED FOR PUBLIC RELEASE;
DISTRIBUTION UNLIMITED.

DTIC
S FEB 24 1984 D
A

THIS WORK WAS SPONSORED BY THE DEFENSE NUCLEAR AGENCY
UNDER RDT&E RMSS CODE B322079464 S99QAXHI00247 H2590D.

Prepared for
Director
DEFENSE NUCLEAR AGENCY
Washington, DC 20305

DTIC FILE COPY

84 01 26 029

Destroy this report when it is no longer needed. Do not return to sender.

PLEASE NOTIFY THE DEFENSE NUCLEAR AGENCY,
ATTN: STTI, WASHINGTON, D.C. 20305, IF
YOUR ADDRESS IS INCORRECT, IF YOU WISH TO
BE DELETED FROM THE DISTRIBUTION LIST, OR
IF THE ADDRESSEE IS NO LONGER EMPLOYED BY
YOUR ORGANIZATION.



UNCLASSIFIED

SECURITY CLASSIFICATION OF THIS PAGE (When Data Entered)

REPORT DOCUMENTATION PAGE		READ INSTRUCTIONS BEFORE COMPLETING FORM	
1. REPORT NUMBER DNA 6237F	2. GOVT ACCESSION NO. ADA 138 288	3. RECIPIENT'S CATALOG NUMBER	
4. TITLE (and Subtitle) SPIRE DATA EVALUATION AND NUCLEAR IR FLUORESCENCE PROCESSES		5. TYPE OF REPORT & PERIOD COVERED Final Report for Period 2 Jan 79—30 Nov 82	
		6. PERFORMING ORG. REPORT NUMBER LMSC-D913086	
7. AUTHOR(s) J. B. Kumer T. C. James		8. CONTRACT OR GRANT NUMBER(s) DNA 001-79-C-0033	
		10. PROGRAM ELEMENT, PROJECT, TASK AREA & WORK UNIT NUMBERS Subtask S99QAXHI002-47	
9. PERFORMING ORGANIZATION NAME AND ADDRESS Lockheed Missiles and Space Co., Inc. P.O. Box 504 Sunnyvale, California 94086		12. REPORT DATE 30 November 1982	
11. CONTROLLING OFFICE NAME AND ADDRESS Director Defense Nuclear Washington, DC 20305		13. NUMBER OF PAGES 118	
		15. SECURITY CLASS (of this report) UNCLASSIFIED	
14. MONITORING AGENCY NAME & ADDRESS (if different from Controlling Office)		15a. DECLASSIFICATION/DOWNGRADING SCHEDULE N/A since UNCLASSIFIED	
16. DISTRIBUTION STATEMENT (of this Report) Approved for public release; distribution unlimited.			
17. DISTRIBUTION STATEMENT (of the abstract entered in Block 20, if different from Report)			
18. SUPPLEMENTARY NOTES This work was sponsored by the Defense Nuclear Agency under RDT&E RMSS Code B322079464 S99QAXHI00247 H2590D.			
19. KEY WORDS (Continue on reverse side if necessary and identify by block number) SPIRE High Altitude Infrared Radiance Spectral Earthlimb Emission Nuclear Effects Atmospheric Atmospheric Infrared Backgrounds Non-LTE Infrared Emission High Altitude Radiance Model Infrared Emission Mechanisms Fireball Light Fluorescence			
20. ABSTRACT (Continue on reverse side if necessary and identify by block number) This report focuses on two major subject areas. The first of these includes the analysis and interpretation of spectral earthlimb emission data obtained in the DNA sponsored SPIRE experiment, and the implications of this analysis for application to cases of interest to the AFGL/DNA community. These would include quantitative specification of ambient non-LTE mechanisms for high altitude infrared radiance, which would also become important infrared background effects in the nuclear case, as well as quantitative identification of deficiencies in the current AFGL High Altitude Infrared Radiance Model.			

DD FORM 1473
1 JAN 73

EDITION OF 1 NOV 65 IS OBSOLETE

UNCLASSIFIED

SECURITY CLASSIFICATION OF THIS PAGE (When Data Entered)

UNCLASSIFIED

SECURITY CLASSIFICATION OF THIS PAGE(When Data Entered)

19. SUPPLEMENTARY NOTES (Continued)

Solar Fluorescence	OH Airglow	Vibraluminescence
CO ₂ Infrared Emission	Chemiluminescence	Earthlimb Radiance
H ₂ O Infrared Emission	Resonance Scattering	

20. ABSTRACT (Continued)

The second subject area involves a supporting laboratory experiment to obtain data pertinent to understanding the nuclear effect of fluorescence of fireball light. The laboratory experiment also directly supports the analysis and interpretation of the SPIRE data and the interpretation and analysis of high resolution spectral earthlimb emission data that are expected to be obtained in forthcoming DNA sponsored high resolution spectral earthlimb emission experiments.

Analysis and interpretation of spectral earthlimb emission data obtained in the SPIRE experiment was aimed at quantifying the role of CO₂⁽⁷⁾ in the formation of the non-LTE earthlimb at wavelengths 15, 4.3 and 2.7 μm. Non-LTE mechanisms for CO₂ emission in these wavelength regions were verified and in some cases upgraded by comparison between predictions and the SPIRE data. Implications of this analysis for the gravity wave-induced horizontal structure in the 15-μm earthlimb and for improving the current High Altitude Radiance Model were also presented.

Analysis of the 15-μm SPIRE data confirmed that two mechanisms were required to be incorporated into the pre-SPIRE model to improve it, namely (1) the detailed altitude dependence of the line and band shape for the 15-μm radiative transfer calculation, and (2) the rate constant for quenching the CO₂ (010) by atomic oxygen was required to be considerably larger at mesospheric temperatures than T^{-1/3} extrapolation from high temperature laboratory data would predict. Three mechanisms were found to dominate the sunlit 4.3-μm earthlimb; these are (1) absorption and subsequent reemission by CO₂, primarily in the 001-000 fundamental band of the major 626 CO₂ isotopic specie at altitudes above 105 km and primarily by 'hot bands' and the bands of minor isotopic species at lower altitudes, (2) the fluorescence of sunlight at 2.7 μm, and to a lesser extent, 2.0 and 1.6 μm sunlight in the altitude range below 105 km, and (3) the transfer of excitation from oxygen singlet D to N₂ vibration via a quenching collision, O('D) + N₂ is important in the 55 to 65 km altitude range. Analysis of the night time 4.3-μm data indicated that (1) the transfer of excitation from OH(V > 0) to N₂(V=1) is required to model the data in the 75 to 90 km altitude region, and (2) a second mechanism is required to model the data at higher altitudes. Direct absorption of sunlight and a "Chapman-like" mechanism were found to be inadequate for this purpose. Our initial analysis of the sunlit 2.7-μm SPIRE data stimulated a coordinated effort within the AFGL/DNA community to understand this aspect of the SPIRE data. This culminated in a combined and complimentary effort by R. Sharma, T. Degges and ourselves in arriving at an understanding of the sunlit 2.7-μm SPIRE data. The major mechanisms were determined by this triad to be (1) the fluorescence of 2.0 and 1.6-μm sunlight by CO₂, (2) the resonance scattering of 2.7-μm sunlight by H₂O, and (3) absorption and reemission of 2.7-μm sunlight by CO₂.

UNCLASSIFIED

SECURITY CLASSIFICATION OF THIS PAGE(When Data Entered)

UNCLASSIFIED

SECURITY CLASSIFICATION OF THIS PAGE(When Data Entered)

THIS PAGE IS INTENTIONALLY LEFT BLANK.

UNCLASSIFIED

SECURITY CLASSIFICATION OF THIS PAGE(When Data Entered)

PREFACE

We gratefully acknowledge the complete and enthusiastic cooperation of AFGL personnel in assisting us in this effort in every respect. In particular, we thank Bill Grieder and Dick Nadile for the preparation, documentation, and discussion of data that were necessary for us to perform this analysis. These data included SPIRE radiance data obtained by spectrally integrating over several bands of interest, as well as SPIRE orbit and attitude data. A large part of the success of our effort can be traced to extensive discussions of some of the more interesting aspects of the data analysis with Ramesh Sharma and Dick Nadile. Discussions with other members of the DNA/AFGL community, in particular George Caledonia and Tom Degges, also provided useful guidance and assistance.

TABLE OF CONTENTS

Section		Page
1	INTRODUCTION AND SUMMARY	7
	1.1 General Introduction	7
	1.2 Summary of the SPIRE Data Evaluation Report	7
	1.3 Summary of Laboratory Effort	8
2	SPIRE DATA EVALUATION AND IMPLICATIONS	10
	2.1 Detailed Qualitative Summary	10
	2.2 Analysis of SPIRE 15 μm Data	13
	2.2.1 Modification in our CO_2 15 μm Model Required to Achieve the Best Fit to the SPIRE Data	14
	2.2.2 Details of the Improved CO_2 15 μm Radiation Transport Model	24
	2.2.3 Further Improvements Required in Our 15 μm CO_2 Model	30
	2.3 Analysis of Sunlit SPIRE 4.3 μm Data	32
	2.3.1 Data Processing and Comparison	32
	2.3.2 Spectral Composition of the Sunlit	37
	2.3.3 General Discussion of the Comparison of the Data and the Predictions	40
	2.3.4 Mechanisms for CO_2 4.3 μm Fluorescence	42
	2.3.5 Mechanisms for the Sunlit Earthlimb Emission at 4.3 μm	43
	2.3.6 Vibrational Temperatures	47
	2.3.7 Band and Line Shape Altitude Dependence in the Limb Radiance Calculations	49
	2.3.8 Possibility of Azimuthal SPIRE Scan Pattern Misregistration	56

TABLE OF CONTENTS (Continued)

Section	Page
2.4 Analysis of the Night Time SPIRE 4.3 μm Data	63
2.4.1 Introduction	63
2.4.2 Comparison of Prediction and Data for Scans 2 and 8	65
2.4.3 Night Time Vibrational Temperatures	70
2.4.4 Comparison of the SPIRE and 4.3 μm Night Time Earthlimb Data	70
2.5 Analysis of Daytime CO_2 Contribution to the 2.7 μm Earthlimb	75
2.5.1 Estimated CO_2 Contribution to the Sunlit 2.7 μm Earthlimb	75
2.5.2 Preliminary Efforts to Spectrally Model the 2.7 μm Earthlimb	78
2.6 Horizontal Structure Considerations	81
2.7 Improvements Suggested in the Current High Altitude Infrared Radiance Model	84
3 LABORATORY STUDY OF CO_2 FLUORESCENCE	87
3.1 Experimental Objectives and Approach	87
3.2 Summary of Experimental Measurements	91
3.3 Results for VV Between N_2 ($V = 1$) and $^{13}\text{C}^{16}\text{O}_2$	97
3.4 Conclusions and Suggestions for Future Studies	103
4 REFERENCES	106

LIST OF ILLUSTRATIONS

Figure		Page
2-1	Composite of 14.05 to 16 μm Spectrally Integrated Radiance Data From all the SPIRE Scans	15
2-2	Temperature Model Used for Modeling Analysis of the SPIRE Data	17
2-3	Number Density Models Used for the Modeling Analysis of the SPIRE Data	18
2-4	Calculation Based on the Pre-SPIRE Model That Uses the Old Rate Coefficients and Altitude Independent Line and Band Shapes Compared With the SPIRE Data	21
2-5	Calculation Improved on Pre-SPIRE Model	22
2-6	Final Version of the Calculation Compared With the SPIRE Data	23
2-7	Geometry and Formulation of the Basic Non-LTE Radiation Transport Equations	25
2-8	Computation of the Radiation Transport Equation Kernel Function Matrix Elements	26
2-9	Computation of Escape Function and Transmission Function Matrix Elements	28
2-10	Earthlimb Radiance Geometry and Calculation	31
2-11	The Data for Scan 9 Compared With Our Predictions	33
2-12	Same as Fig. 2-11 Except for Scan 10	34
2-13	Same as Fig. 2-11 Except for Scan 11	35
2-14	Same as Fig. 2-11 Except for Scan 12	36
2-15	Contributions to CO_2 4.3 μm Earthlimb Fluorescence	44
2-16	The Contributions From Each of the Mechanisms Numbered 1 Through 9 on Table 2-4 Are Plotted as a Function of Altitude	45

LIST OF ILLUSTRATIONS (Continued)

Figure		Page
2-17	The Contributions From Each of the Mechanisms Numbered 1 Through 9 on Table 2-4, Plotted as a Function of Altitude	46
2-18	Vibrational Temperatures and Atmospheric Kinetic Temperature for Scan 9	48
2-19	The Quantity σN_l for Earthlimb Geometry and the Earthlimb Viewing Width Function $W(\sigma N)$ Calculated by Utilizing Assumptions for the Line and Band Shapes	52
2-20	The Earthlimb Path Mass Averaged Value for the Lorentz Parameter Plotted Versus Tangent Altitude	53
2-21	Same as Fig. 2-11 Except Calculations Utilizes the Same Altitude Independent Line and Band Shapes	54
2-22	SPIRE Spectral Earthlimb Radiance Data in the 3.9 to 4.1 μm Window Version Plotted Versus Tangent Altitude	58
2-23	Same as Fig. 2-11 Except for Reduced Solar Elevation Angles	59
2-24	Same as Fig. 2-12 Except for Reduced Solar Elevation Angles	60
2-25	Same as Fig. 2-13 Except for Reduced Solar Elevation Angles	61
2-26	Same as Fig. 2-14 Except for Reduced Solar Elevation Angles	62
2-27	The 4.3 μm Data for Dark Scan 2 Given by Curve 1	66
2-28	Same as Fig. 2-27 Except the OH Airglow-Related Mechanism 2 in Table 2-5	67
2-29	Same as Fig. 2-28 Except the Chapman-Like Airglow-Related Mechanism in Table 2-5	68
2-30	Same as Fig. 2-29 Except the Data are From Scan 9	71
2-31	Atmospheric Kinetic Temperature (Curve 1), N_2 and CO_2 (001) Vibrational Temperatures Shown Here	72
2-32	Atmospheric Kinetic Temperature (Curve 1), N_2 and CO_2 Vibrational Temperatures Shown Here	73
2-33	Atmospheric Kinetic Temperature (Curve 1), N_2 and CO_2 Vibrational Temperatures Shown Here	74

LIST OF ILLUSTRATIONS (Continued)

Figure		Page
2-34	Predictions for the CO ₂ Contribution (Curve 1) to the Sunlit 2.7 μm Earthlimb	77
2-35	The Contribution to the Sunlit 2.7 μm Spectral Earthlimb Due to Absorption and Reemission of Sunlight by CO ₂ is Shown Here	79
2-36	Earthlimb Radiance in the 14 to 16 μm Region	83
3-1	Experimental Arrangement for Measurement of Fluorescence at 4.3 μm	94
3-2	Multiple Pass Cell	94
3-3	Geometry and Electronics for Two-Channel Run	96
3-4	Plot of the Rate of Emission of 4.3 μm Radiation as a Function of Time	101
3-5	Plot of the Emission of 4.3 μm Radiation as a Function of Time	102

LIST OF TABLES

Table		Page
2-1	Conditions Used for Calculations	19
2-2	References for Rate Constants Utilized in the CO ₂ 15 μm Model	19
2-3	The CO ₂ 4.3 μm Bands	38
2-4	Mechanisms for Daytime Excitation of CO ₂ v ₃ in the Upper Atmosphere	39
2-5	Mechanisms for Night Time Excitation of CO ₂ v ₃ in the Upper Atmosphere	69

Section 1
INTRODUCTION AND SUMMARY

1.1 GENERAL INTRODUCTION

In this report we document progress we have made in two major subject areas. The first of these includes the analysis and interpretation of spectral earthlimb emission data obtained in the DNA sponsored SPIRE experiment, and the implications of this analysis for application to cases of interest to the AFGL/DNA community. The second subject area involves a supporting laboratory experiment to obtain data pertinent to understanding the nuclear effect of fluorescence of fireball light. The laboratory experiment also directly supports the analysis and interpretation of the SPIRE data and the interpretation and analysis of high resolution spectral earthlimb emission data that are expected to be obtained in forthcoming DNA sponsored experiments, such as the SPIRIT and related experiments.

1.2 SUMMARY OF THE SPIRE DATA EVALUATION EFFORT

Analysis and interpretation of spectral earthlimb emission data obtained in the SPIRE experiment was the principal thrust of this effort. The analysis was aimed at quantifying the role of CO₂ in the formation of the non-LTE earthlimb at wavelengths 15, 4.3 and 2.7 μm . Non-LTE mechanisms for CO₂ emission in these wavelength regions were verified and in some cases upgraded, by comparison between predictions and the SPIRE data. Implications of this analysis for the gravity wave-induced horizontal structure in the 15 μm earthlimb were also presented.

Analysis of the 15 μm SPIRE data confirmed that two mechanisms were required to be incorporated into the pre-SPIRE model to improve it, namely (1) the detailed altitude dependence of the line and band shape for the 15 μm radiative transfer calculation, and (2) the rate constant for quenching the CO₂ (010) by atomic oxygen was required to be considerably larger at

mesospheric temperatures than $T^{-1/3}$ extrapolation from high temperature laboratory data would predict. Three mechanisms were found to dominate the sunlit 4.3 μm earthlimb; these are (1) absorption and subsequent reemission by CO_2 , primarily in the 001-000 fundamental band of the major 626 CO_2 isotopic species at altitudes above 105 km and primarily by weak 'hot bands' and minor isotopic species at lower altitudes, (2) the fluorescence of sunlight at 2.7 μm , and to a lesser extent, 2.0 and 1.6 μm sunlight in the altitude range below 105 km, and (3) the transfer of excitation from oxygen singlet D to N_2 vibration via a quenching collision, $\text{O}('D) + \text{N}_2$ is important in the 55 to 65 km altitude range. Analysis of the night time 4.3 μm data indicated that (1) the transfer of excitation from $\text{OH}(V > 0)$ to $\text{N}_2(V=1)$ is required to model the data in the 75 to 90 km altitude region, and (2) a second mechanism is required to model the data at higher altitudes. Direct absorption of sunlight and a "Chapman-like" mechanism were found to be inadequate for this purpose. Our initial analysis of the sunlit 2.7 μm SPIRE data stimulated a coordinated effort within the AFGL/DNA community to understand this aspect of the SPIRE data. This culminated in a combined and complimentary effort by R. Sharma, T. Degges and ourselves in arriving at an understanding of the sunlit 2.7 μm SPIRE data. The major mechanisms were determined by this triad to be (1) the fluorescence of 2.0 and 1.6 μm sunlight by CO_2 , (2) the resonance scattering of 2.7 μm sunlight by H_2O , and (3) absorption and reemission of 2.7 μm sunlight by CO_2 .

Quantitative details are given in section 2.0 below, previewed by a detailed qualitative summary in section 2.1.

1.3 SUMMARY OF LABORATORY EFFORT

We have conducted laboratory studies of the fluorescence of CO_2 at 4.3 μm resulting from initial excitation of the 101 band due to absorption of laser light near 2.7 μm . By utilizing a pulsed laser source at 2.7 μm we have been able to observe the resulting fluorescence at 4.3 μm and thereby provide direct laboratory confirmation of this mechanism which is a major contributor to the earthlimb radiance from CO_2 near 80 km altitude.

Our report discusses several experiments designed to verify the branching ratio for radiation at 4.3 μm versus reemission at 2.7 μm . Several experimental difficulties pertinent to this measurement are discussed. We also describe measurements of the rate of decay of the 4.3 μm emissions for $^{13}\text{CO}_2$ and $^{12}\text{CO}_2$ in the presence of N_2 and the interpretation of these results as they relate to the rate of vibrational energy transfer between CO_2 and N_2 . Additional possibilities for enhanced understanding of the mechanisms related to CO_2 emission which would involve measurements of several LWIR bands of CO_2 are discussed.

Section 2 SPIRE DATA EVALUATION AND IMPLICATIONS

2.1 DETAILED QUALITATIVE SUMMARY

Analysis of the 15 μm SPIRE data given in section 2.2 below shows that our pre-SPIRE non-LTE model for the CO_2 15 μm earthlimb was deficient in two aspects. First, the altitude dependence of the line and band shape needed to be accounted for in our radiative transfer model. Second, we also needed to utilize an updated rate constant for the quenching of $\text{CO}_2(010)$ by atomic oxygen. This updated rate constant is required to be much faster at mesospheric temperatures than the rate recommended by Taylor (1974) on the basis of the extrapolation from high temperature laboratory data that the log of the rate constant is proportional to $T^{-1/3}$.

That the first of these effects might be important was first suggested at a DNA meeting some years back by T. Degges in discussion of effects seen in 15 μm zenith radiance data that had been obtained in a rocket borne experiment on 3/22/73 (Rogers et al., 1976). In subsequent analysis of these 15 μm zenith radiance data and another set obtained 2/14/74 (Rogers et al., 1977) we incorporated the effects of altitude dependence in the line and band shape. But we found there was still indication that some further improvements were required to achieve satisfactory agreement with the 15 μm zenith radiance data sets. To this end we proposed that a much faster rate constant at mesospheric temperatures for the quenching of $\text{CO}_2(010)$ by atomic oxygen than was recommended by Taylor (1974) on the basis of extrapolation from high temperature laboratory data could indeed provide the key to achieving satisfactory agreement with the two 15 μm zenith radiance data sets.

Recent laboratory measurements (Simpson, 1980; Allen et al., 1980) of quenching of $\text{CO}_2(010)$ by N_2 have shown that high temperature results of this rate constant could not be extrapolated to low mesospheric temperatures by

the method recommended by Taylor, and that in fact, the extrapolation severely underpredicted the low temperature rate constant, as we had suggested might be the case for the quenching by atomic oxygen as based on our analysis of the 15 μm zenith radiance data. Based on the Simpson data, Sharma and Nadile, (1980) proposed a square root dependence at low temperature for the quenching by atomic oxygen, normalized to achieve a reasonable fit to the SPIRE 15 μm data. Sharma developed a non-LTE model for the CO_2 15 μm earthlimb that utilized both the altitude dependent line and band shape for radiative transfer for the CO_2 15 μm radiation, and also the faster rate constants at mesospheric temperatures for quenching by N_2 , O_2 and most importantly, by atomic oxygen. He utilized this model to achieve a much better understanding and fit to the SPIRE 15 μm data than had been achieved by earlier pre-SPIRE calculations. In the work we report here in section 2.2 we provide independent confirmation for the results obtained by Sharma.

The comparison of our predictions and the daytime SPIRE 4.3 μm data that we report in section 2.3 below confirms the predictions of James and Kumer (1973) that the fluorescence of 2.7 μm sunlight by CO_2 is a major mechanism for producing the daytime 4.3 μm earthlimb on the tangent altitude interval from approximately 60 to 110 km. The role of fluorescence of 2.7 μm sunlight by minor isotopic CO_2 species, and the role of fluorescence of 2.0 and 1.6 μm sunlight by CO_2 are also considered. These are shown to be significant, but not dominant mechanisms for producing the daytime 4.3 μm earthlimb. The contribution of "weak" CO_2 4.3 μm bands is seen to be approximately as important as fluorescence of shorter wavelength sunlight for producing the daytime 4.3 μm earthlimb for tangent altitudes less than approximately 110 km. This result could be inferred from the papers of Kumer (1977a) and Caledonia et al. (1982). For tangent altitudes greater than approximately 65 km the primary weak band excitation mechanism is absorption of 4.3 μm sunlight. This is also the primary excitation mechanism for the strong CO_2 626 00 $\bar{7}$ -000 4.3 μm band in that altitude region. In the 55 to 65 km altitude region the excitation of $\text{N}_2(\text{V}=1)$ by transfer of energy from oxygen singlet D is found to be a major contributor for excitation of CO_2 4.3 μm emission as predicted by Kumer (1977a). It was found that a better fit to the data could

be achieved in the altitude region less than 80 km by utilizing an earthlimb radiance calculation that accounts for altitude dependence in line and band shape. An analytic approximation for the radiative transfer width and transmission functions (defined in the paper by Kumer and James, 1974) derived from work done by Neuendorffer (1982) was utilized for this purpose. The approximation also utilizes the mass path averaging technique to approximate the line and band shape parameters for a given earthlimb viewing line of sight as suggested by Weinreb (1982).

In general we slightly overpredicted the daytime 4.3 μm data for all four sunlit scans. We investigated the possibility that this resulted from some uncertainty in the knowledge of the azimuth of the SPIRE scan pattern such that the pattern was rotated further than thought from the sun thereby requiring lower solar elevation angles for our calculation than were actually prescribed by AFGL personnel. Careful study indicated this was not the case. We now believe our general overprediction is most likely the result of a minor inaccuracy in absolute radiometric calibration.

The analysis of the night time 4.3 μm earthlimb in Section 2.4 supports the theory of Kumer et al. (1978) that the principal night time CO_2 4.3 μm excitation mechanism in the approximate region 75 to 90 km is the transfer of vibration from the OH airglow upper states $\text{OH}(V > 0)$ to $\text{N}_2(V=1)$ followed by subsequent transfer to the $\text{CO}_2(v_3)$ states. At higher altitude an additional source of excitation is required to model the data. In our analysis we showed that direct absorption of sunlight could not be responsible for this additional source. We also showed that a "Chapman-like" airglow related source could not be responsible for the additional excitation.

In section 2.5 we discuss our work in modeling the CO_2 contribution to the sunlit 2.7 μm earthlimb. In our first efforts at modeling the daytime CO_2 contribution to the 2.7 μm earthlimb we showed (Kumer, 1981) that absorption and reemission of 2.7 μm sunlight by the 626 CO_2 specie would severely underpredict the SPIRE data. This stimulated the community to reconsider the problem. Sharma (1981) showed that the CO_2 contribution would be

considerably enhanced by considering fluorescence of 2.0 and 1.6 μm sunlight. Degges (1981) showed there was a very significant contribution to the daytime 2.7 μm earthlimb due to absorption of 2.7 μm sunlight by H_2O followed by subsequent reemission. We showed that an additional enhancement in the model could be obtained by considering the absorption and reemission of sunlight at 2.7 μm by the minor isotopic CO_2 species. Sharma (1981) pulled all these results together and showed that the combination of these effects can in fact reasonably account for the SPIRE daytime 2.7 μm earthlimb data.

In section 2.6 we considered a simplified implication of the SPIRE data. Looking ahead to problems of interest such as that of the horizontal structure in limb radiances at various wavelengths we utilized what we had learned in the 15 μm region to generate an example of the horizontal structure that might be caused in the 15 μm region by a gravity wave. For the simplified gravity wave model we utilized a cross section of data (Noxon, 1978; Faire et al., 1972; Petersen 1979) from the literature on the perturbation effects of gravity waves on the ambient temperature profiles and the simple theory of Hines (1960) to relate temperature and density perturbations. These data suggested that a model with a temperature perturbation of 40 deg at 95 km and wavelengths of 140 km horizontally and 20 km vertically is not unreasonable. This example gravity wave is consistent with description of the data, and the theory of the phenomenon presented in Chapter 5 in the report (AFGL-TR-81-0207, Atmospheric Infrared Radiance Variability, edited by Humphrey et al., 1981), which is devoted to structure and wave-like phenomena in the upper atmosphere. For this model we perturbed the SPIRE model atmosphere for two cases differing by π in phase and performed 15 μm limb radiance calculations for these two cases. Significant horizontal radiance structure was noted as the result of this exercise.

2.2 ANALYSIS OF SPIRE 15 μm DATA

The discussion in section 2.2 focusses on the analysis of the final version of firm computer processed spectrally integrated SPIRE data in the 14 to 16 μm band as prepared by Sharma and Nadile, 1980. The final version of the

Nadire SPIRE 14 to 16 μm data and a representation of these data that we will use in subsequent comparisons with our calculations is shown in Fig. 2-1. An overall numerical correction factor of 2, discovered by Dave Green in 1981, has been applied to the data shown on Fig. 2-1.

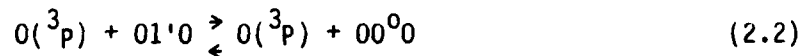
2.2.1 Modifications in our CO_2 15 μm Model Required to Achieve the Best Fit to the SPIRE DATA

A major point of interest in the SPIRE 15 μm data is the prominent plateau-like structure which appears in the 90- to 110-km region, this feature was not predicted by pre-SPIRE non-LTE models of the 15- μm CO_2 earthlimb. In this report we provide evidence for upgrading the pre-SPIRE model by two effects (1) inclusion of altitude dependence in the CO_2 rotational population and in the absorption line shape, and (2) the use of a faster rate for quenching by $\text{O}(^3\text{P})$ of the CO_2 upper state 01^0 for 15- μm radiation than earlier literature recommended estimates (Taylor, 1974).

The principal excitation mechanisms for CO_2 15- μm emission in the earth upper atmosphere include absorption of earth shine and excitation by thermal collisions with the more abundant species in the earth's atmosphere, i.e.,



and



These reactions proceeding to the right result in the quenching component due to constituent M at a rate $Q_{iM} = K_i [M]$ where M may be O_2 , N_2 , or $\text{O}(^3\text{P})$, and where i correspondingly is 1 or 2. Proceeding to the left excitation by thermal collisions is given by $X_{im} = 2 k_i B_k [M]$ where B_k is the Boltzmann factor associated with the local atmospheric kinetic temperature, and factor 2 accounts for the increased degeneracy in the upper level 01^0 with respect to the lower 00^0 . For our discussion it is

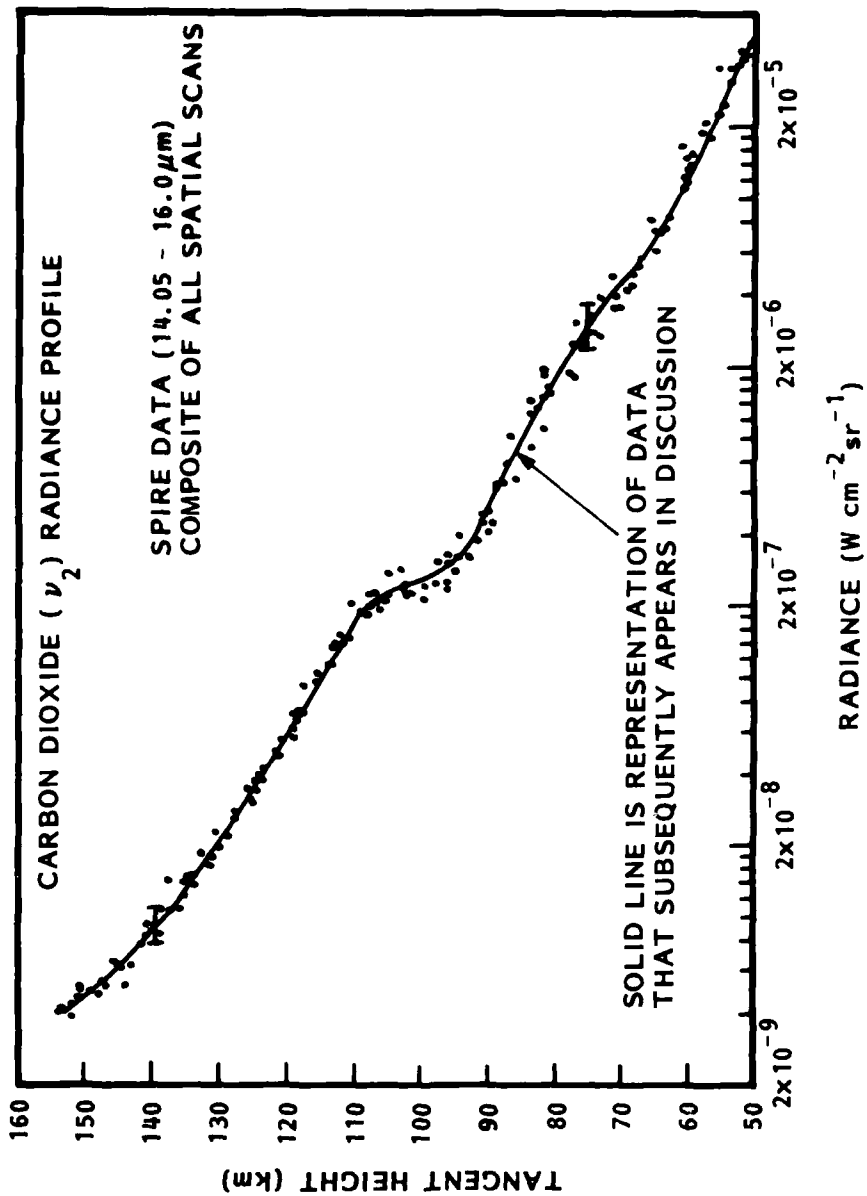


Figure 2-1 A composite of 14.05 to 16.0 μm spectrally integrated radiance data from all the SPIRE scans (from Sharma and Nadile, 6-27-1980) is given by the points, the solid line is a representation of these data that is utilized in subsequent discussion for comparison with predictions.

critically important to point out that at high altitudes ($Z \sim 75$) where $A/Q \gg 1$, i.e., where radiation rather than quenching dominates de-excitation of the $O1^0$ state, an increase in the quenching rate constants k_i actually results in an increase in CO_2 $15 \mu m$ emission.

Another complicating facet of the problem is that the CO_2 $15 \mu m$ emission is strongly self-absorbed along the limb viewing line of sight up to 120 km tangent altitude. Radiation transport that accounts for multiple absorption and re-emission of CO_2 $15 \mu m$ photons is required. We will review our detailed radiation transport formulation, which includes the temperature induced altitude variation in rotational population and absorption line shapes, in section 2.2.2 below.

The calculations we report here were performed with a model atmosphere for the SPIRE event that was utilized by Sharma and Nadile (1980).

This model atmosphere is shown on Figs. 2-2 and 2-3. The Refs. 2, 3, and 4 that are cited in Table 2-1 are given in Table 2-2. Calculations of the SPIRE 14- to 16- μm earthlimb above 65 km were performed for various conditions as listed in Table 2-1. The parameter "key" identifies these conditions in subsequent discussions. The parameter Z_b is the lower boundary of the calculations; blackbody radiation upward incident at Z_b is characterized by the atmospheric temperature at Z_b . The rate constant k_i for quenching of $O1^0$ by N_2 or O_2 and k_2 for quenching by O are given as a function of temperature T by the following:

Process	Reference		Analytic Approximations
M + 010	3	k_{1T}	$= 6.69 \times 10^{-10} \times \exp(-84.01/T^{1/3})$
M + 010	4	k_{1S}	$= k_{1T} + 10^{-16} \sqrt{T}$
O + 010	3	k_{2T}	$= 2.32 \times 10^{-9} \times \exp(-76.75/T^{1/3})$
O + 010	2	k_{2S}	$= k_{2T} + 10^{-14} \sqrt{T}$

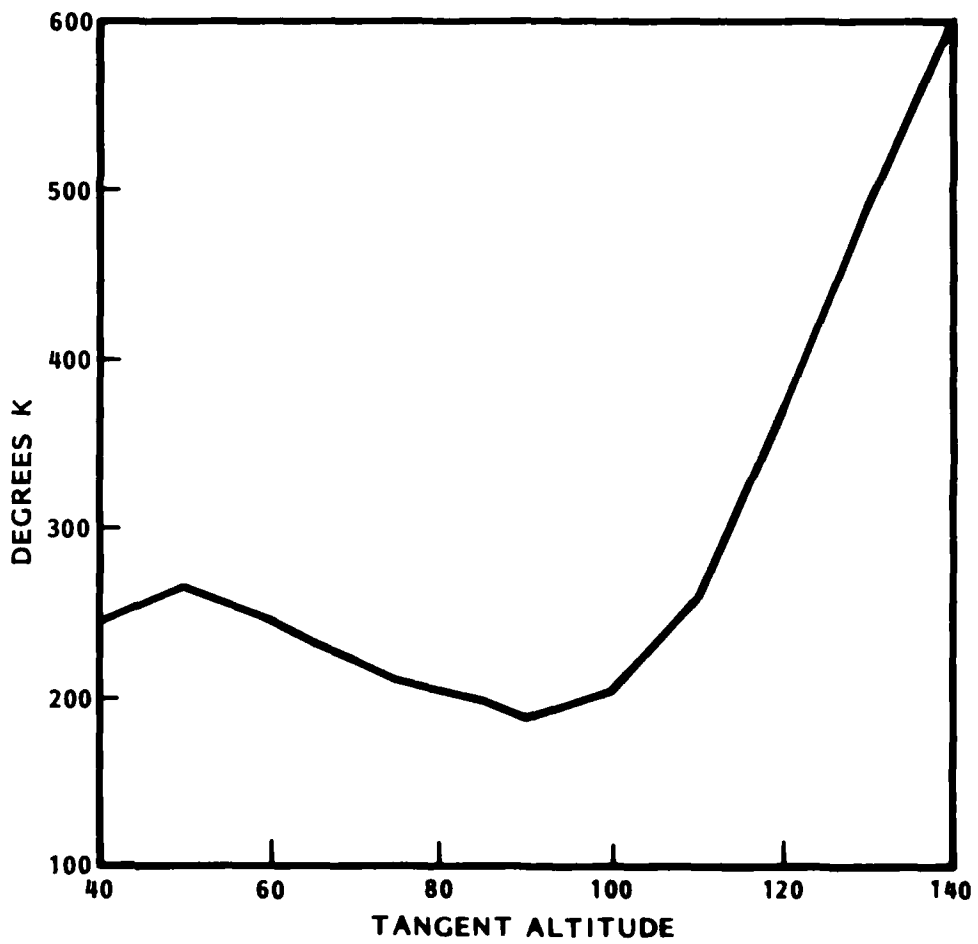


Figure 2-2 Temperature model used for modeling analysis of the SPIRE data (from Sharma and Nadile, 6-27-1980).

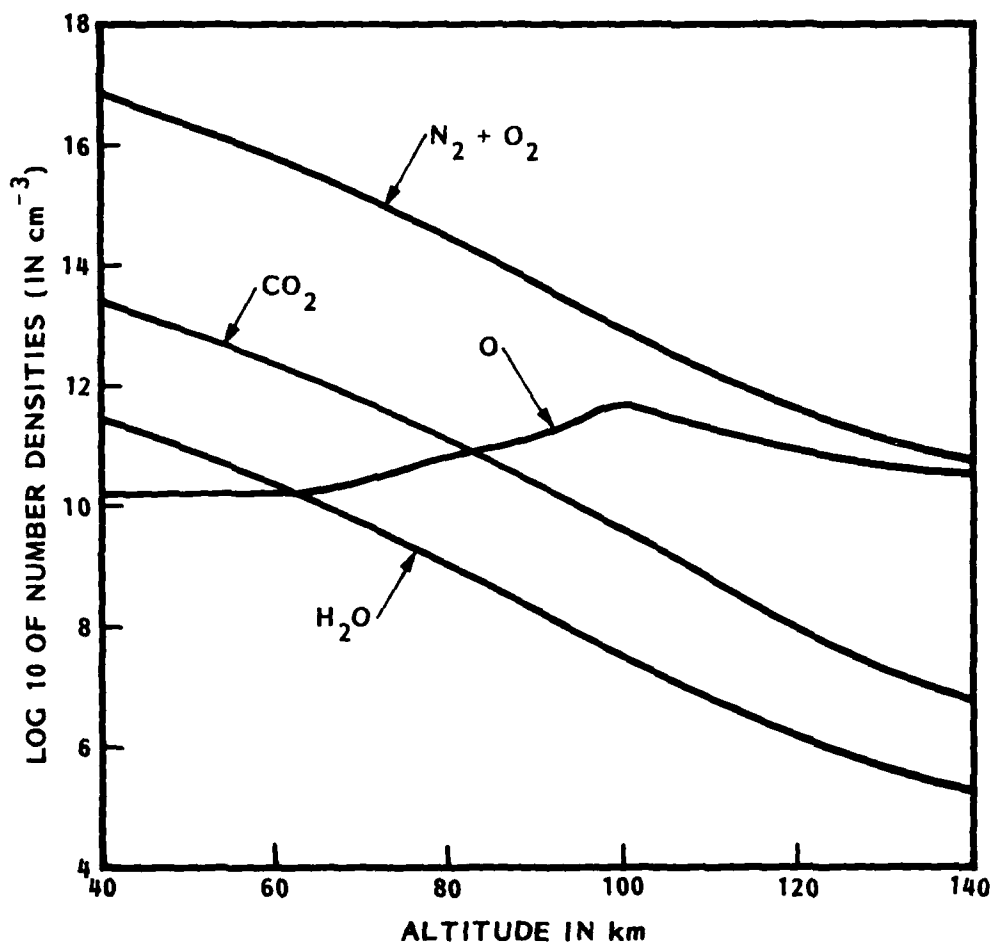


Figure 2-3 Number density models used for the modeling analysis of the SPIRE data (from Sharma and Nadile, 6-27-1980).

Table 2-1 CONDITIONS USED FOR CALCULATIONS

KEY Z _b	(km)	Rate Constants		Absorption Line and Band Shape(a)
		M+010	0+010	
1	65	Ref. 4	Ref. 2	Variable with altitude
2	65	Ref. 4	Ref. 3	Variable with altitude
3	65	Ref. 3	Ref. 3	Variable with altitude
3-LOLORP	65	Ref. 3	Ref. 3	Line shapes fixed by 65-km temperature and 65-km pressure broadening
3-HILORP	65	Ref. 3	Ref. 3	Line shapes fixed by 65-km temperature and 140-km pressure broadening
4-LOLORP	65	Ref. 4	Ref. 2	As in 3-LOLORP
4-HILORP	65	Ref. 4	Ref. 2	As in 3-HILORP
5	40	Ref. 4	Ref. 2	Variable with altitude
6-HILORP	40	Ref. 4	Ref. 2	Line shapes fixed by 40-km temperature and 140-km pressure broadening

(a) Distribution of rotational populations.

Table 2-2 REFERENCES FOR RATE CONSTANTS UTILIZED IN THE CO₂ 15 μm MODEL

2. R. Sharma and R. Nadile, "Carbon Dioxide (ν_2) Radiance Results Using a New Nonequilibrium Model," paper presented at DNA-AFGL Nuclear Weapon Effects Chemistry Conf., AFGL, Bedford, MA, 26 and 27 June 1980.
3. R. L. Taylor, "Energy Transfer Processes in the Stratosphere," Can. J. Chem., Vol. 52, 1974, p. 1436.
4. C. J. S. M. Simpson, private communications, 1980.

The analytic approximations to k_{1S} and k_{2S} were presented by Sharma at the 1980 DNA Chemistry Meeting. The analytic forms for K_{1S} and K_{2S} shown here are preliminary expressions derived by Sharma. The form for K_{1S} was selected by Sharma to have the same low temperature functional form as K_{1S} and to achieve a reasonable fit to the SPIRE data. We stress that the form that we show for K_{2S} is a preliminary version and that Sharma has probably updated this version in his more recent efforts to achieve a best fit to the SPIRE data.

Calculations in which variation in the CO_2 band and line absorption shapes as a function of altitude varying temperature and pressure are designated by key = 1, 2, 3, and 5. For comparison, some calculations performed with band and line shapes constant throughout the atmosphere are characterized by temperature T taken to be $T(Z_b)$ and by pressure broadening as given by Table 2-1.

Case key = 3-HILORP represents the pre-SPIRE model, which uses the old rate constants and non-varying line and band shapes; results of the calculation are compared to the data representation in Fig. 2-4. It can be seen that the plateau-like feature present in the data near 95 to 110 km is not at all present in the calculation. The case key = 2, which improves on the old model in that the recent Simpson data for reaction (1) is utilized and, in that the altitude variation in line and band shape is accounted for, is shown in Fig. 2-5. Here we see noted improvement between the predictions and data as compared to the pre-SPIRE results previously shown on Fig. 2-4. The best agreement however is achieved for the case key = 1 and is shown on Fig. 2-6. This case further includes a postulated low temperature enhancement in $O(^3P)$ rate constant k_2 for quenching $O1^1O$ as discussed above. We consider the case key = 1 as providing the best fit since details of the shape of the limb radiance profile are best reproduced by this case. A somewhat higher quality fit of the data could be achieved in this case by translating the SPIRE data set down by ~ 2 to 4 km. This is consistent with the stated experimental accuracy of absolute altitude determination for the SPIRE data.

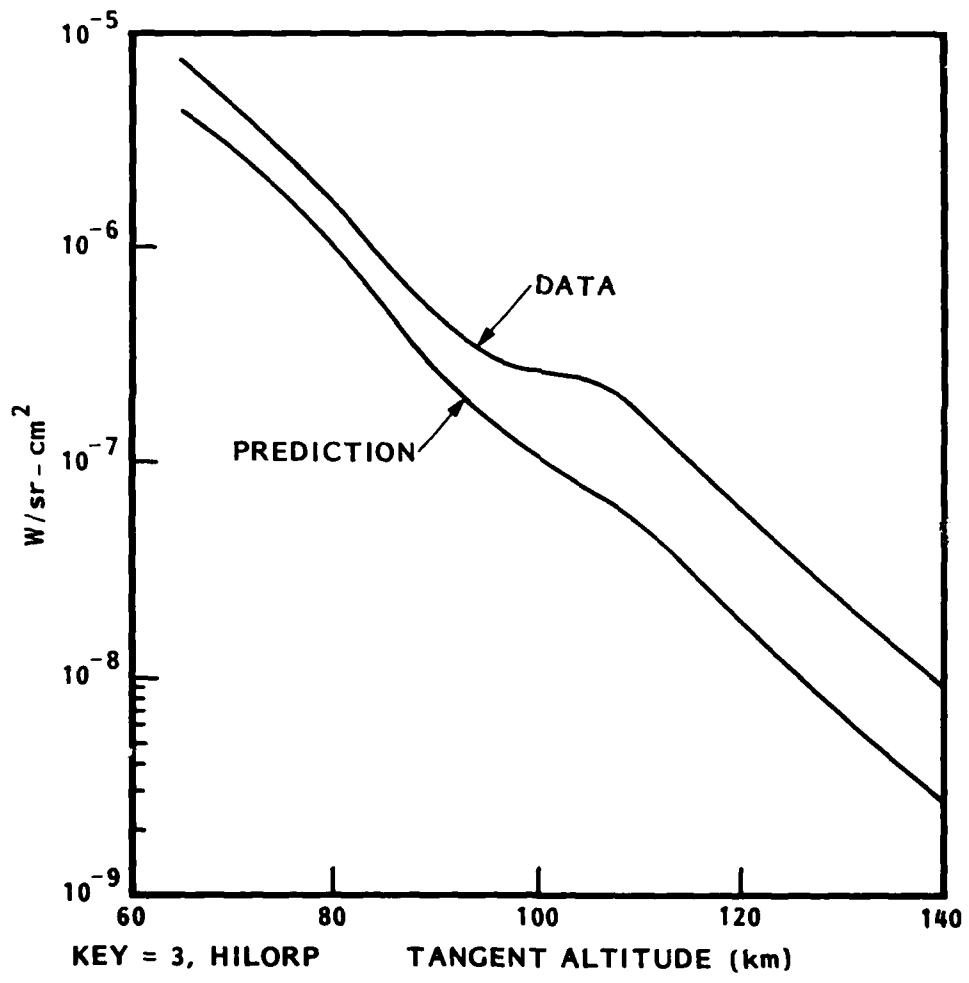


Figure 2-4 Calculation based on the pre-SPIRE model which uses the old rate coefficients and altitude independent line and band shapes is compared with the SPIRE data, key=3-HILORP.

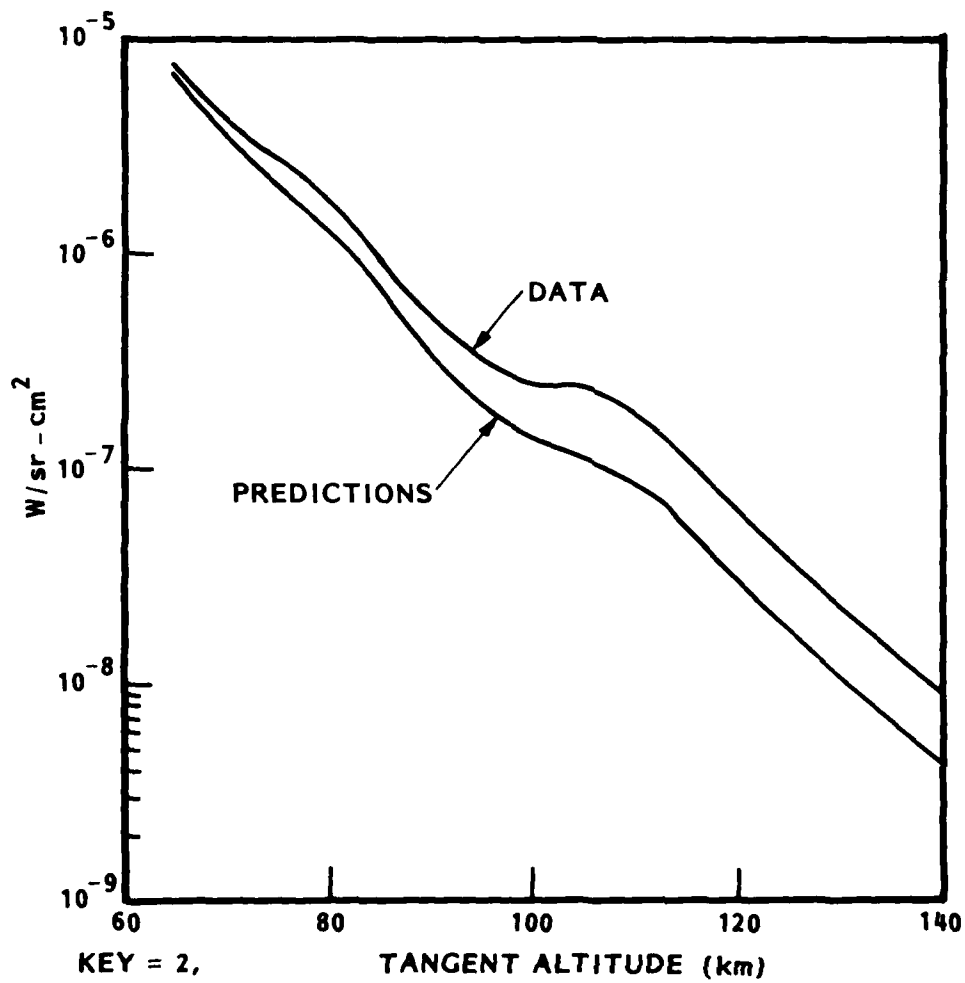


Figure 2-5 Calculation improved on pre-SPIRE model in that altitude dependence of line and band shape is accounted for, the old rate coefficients are utilized however, is compared with the SPIRE data, key=2.

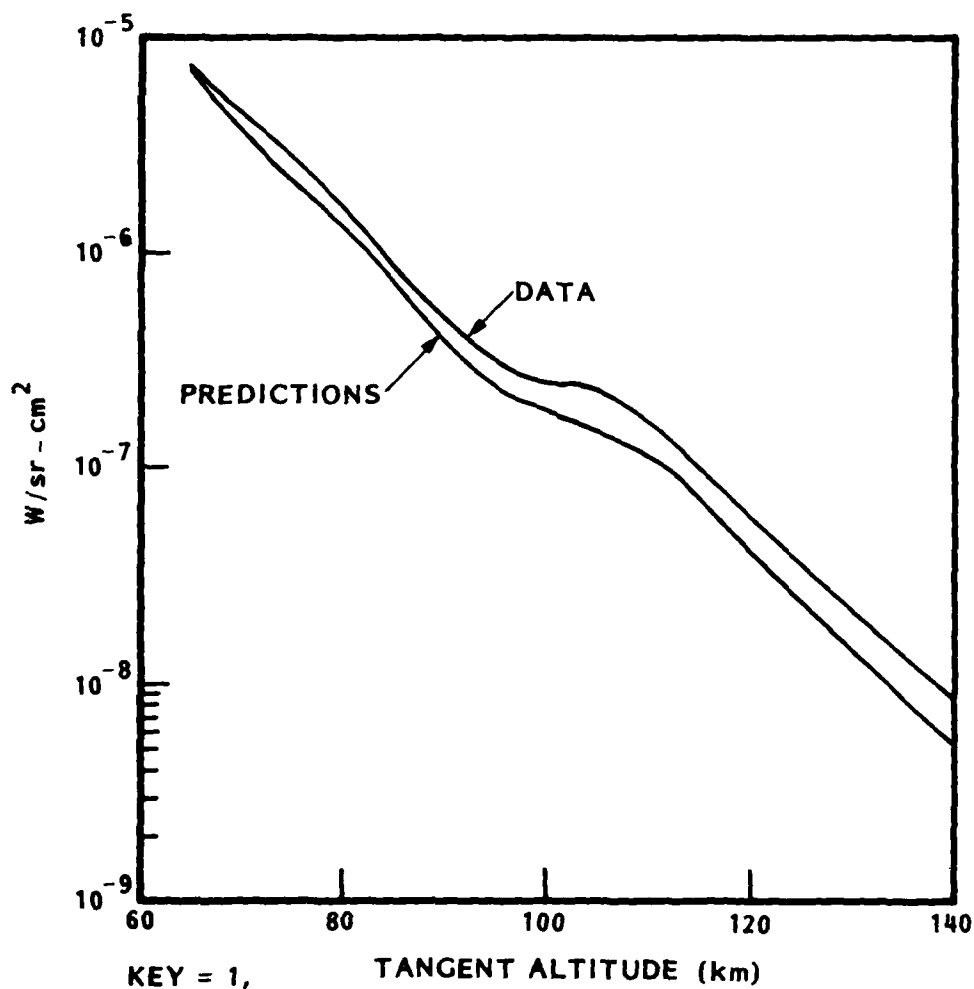


Figure 2-6 Final version of the calculation is compared with the SPIRE data , key=1. This version is improved over the pre-SPIRE model in that (1) altitude dependence of the line and band shapes is accounted for, and (2) the newer values for the rate constants as proposed by Sharma (discussed in the text) are utilized.

In this, our final report, we present results for the cases key = 1, 2, and 3-HILORP since these constitute a useful illustration of the improvements we have implemented in our 15 μm model. Exhaustively detailed results and further discussion of all the cases included in Table 2-1 have been presented in a previous contractual progress report. These results and the further discussion are available on request for the interested reader.

2.2.2 Details of the Improved CO_2 15 μm Radiation Transport Model

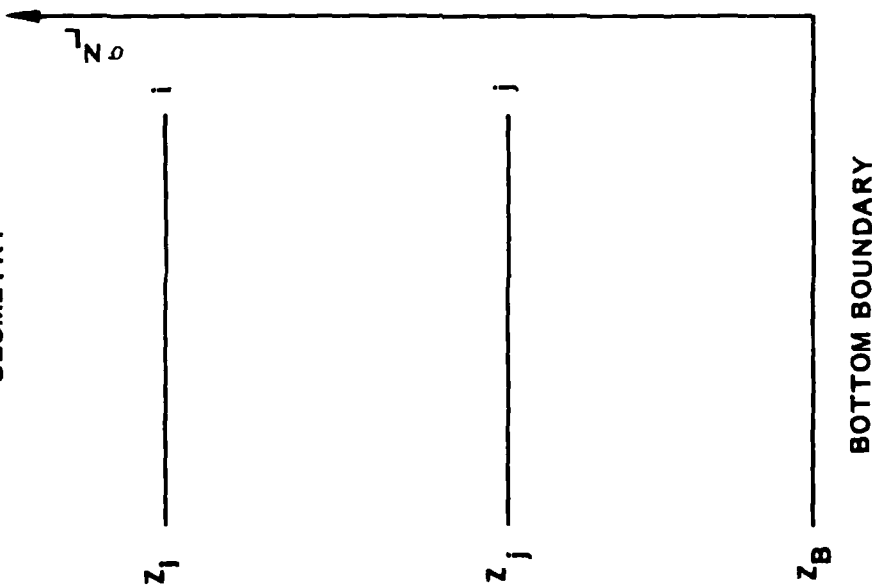
The ability to account for the temperature and pressure altitude dependent variation in the CO_2 010-000 line and band shape is one of the two major improvements in the models that are required to achieve an improved fit to the data. In this sub-section we discuss the implementation of the effect into the model in more detail.

The radiation transport problem breaks into two distinct steps: first, the non-LTE calculation of the altitude dependent population of upper state of the band, and second, the calculation of the observable radiance that results from this non-LTE solution. In step 1, multiple self absorption and emission of photons must be accounted for in general. In step 2, emission and self absorption of photons along the sensor line of sight must be accounted for.

Calculation of the Non-LTE Solution. On Fig. 2-7 we show the basic geometry and transport equation to determine S the excitation rate of CO_2 01'0 per unit $\sigma [\text{CO}_2]$ at altitude Z . The discretized matrix version of this integral radiative transport equation $\epsilon_j G_{ij} S_j = S_{oi}$ which actually must be solved on a digital computer in order to solve for S_i (i.e., the value of S at altitude Z_i) is also shown on Fig. 2-7.

The physics involved in the calculation of the radiative transport matrix elements are shown in Fig. 2-8. The nested loops in the computer program that are required for the calculation of the matrix elements H_{ij} and for the array T_j^i is also indicated on Fig. 2-8.

GEOMETRY



BASIC TRANSPORT EQUATION

$$S = S_0 + \int \sigma dN' H (IN' - NI) \Omega' S'$$

S IS EXCITATION RATE PER $\sigma [CO_2]$

ΩS IS VOLUME EMISSION PER $\sigma [CO_2]$

i.e., $\sigma dN = \sigma [CO_2] dz$

DISCRETE VERSION

$$S_i = S_{oi} + \sum_j H_{ij} W_j \Omega_j S_j$$

WHERE (FOR QUADRATURE)

$$\sum_j W_j = \sigma N_L = \int_{z_B} \sigma dN$$

AND

$$\int \sigma dN' H (IN' - NI) = \int \sigma dN H (IN' - NI) = \sum_{ij} H_{ij} W_j = 1 - E_i$$

FINALLY:

$$G_{ij} S_j \equiv S_i - (1 - E_i) \Omega_i S_i - \sum_j H_{ij} W_j (\Omega_j S_j - \Omega_i S_i) = S_{oi}$$

Figure 2-7 Geometry and formulation of the basic non-LTE radiation transport equations

FOR $i \neq j$ 4 NESTED LOOPS COMPUTE H_{ij}

$$H_{ij} = \frac{1}{2} \sum_B \sum_J g_J(z_i) g_J(z_j) \int_{\sqrt{\pi}}^{dx}$$

$$\{ \varphi(a_j, b_j, x) \varphi(a_j, b_j, x) s_B^2 b_j b_j E_1 (s_B \tau_j^{ij}(x)) \}$$

S_B ACCOUNTS FOR BRANCH P, R AND Q; $\Sigma S_B = 1$; $b_j = \nu_D(z_B) / \nu_D(z_i)$; $a_j = P(z_i) \gamma / \nu_D(z_i)$

$g_J(z_i)$ IS FRACTIONAL ROTATIONAL POPULATION, $\Sigma g_J = 1$; φ IS VOICHT FUNCTION

THE $\tau_j^{ij}(x) = \tau_j^i(x) - \tau_j^j(x)$ AND $\tau_j^i(x)$ ARE COMPUTED BY 3 NESTED LOOPS

$$\tau_j^{(i+1)}(x) = \tau_j^i(x) + \Delta \tau_j^{i(i+1)}(x) \text{ AND } \Delta \tau_j^{i(i+1)}(x) = \int_{z_i}^{z^{(i+1)}} dz [\text{CO}_2] g_J(z) \sigma b \varphi(a(z), bx)$$

Figure 2-8 Computation of the radiation transport equation kernel function matrix elements including temperature and pressure variation in line and band absorption profiles

Note that line shape altitude dependence is accounted for by the altitude dependent parameters b_i , a_i and $G_J(Z_i)$. The quantity b_i is the ratio of Doppler width $\nu_D(Z_b)$ at reference altitude Z_b to the width $\nu_D(Z_i)$ at the altitude Z_i . Here ν_D is the 1/2 e-fold Doppler width as used commonly in the astrophysical literature. The altitude dependent parameter a_i gives the ratio of the 1/2 maximum 1/2 width pressure broadened Lorentz line parameter $P(Z_i) \gamma (T[Z_i]/296^\circ)^{-1/2}$ to the Doppler width $\nu_D(Z_i)$. Here $P(Z_i)$ is the atmospheric pressure at altitude Z_i in units atm at altitude Z_i , $\gamma \sim 0.07 \text{ cm}^{-1}/\text{atm}$ is the pressure broadened Lorentz parameter for CO_2 by air at STP and the factor $(T(Z_i)/296^\circ)^{-1/2}$ accounts for temperature variation in γ . The Voigt line profile $\phi(a_i, b_i, x)$ then, with $x = (\nu - \nu_0)/\nu_D(Z_b)$, gives the altitude dependence of the line shape for a line centered at ν_0 . The altitude dependence of the band shape is given by $G_J(Z_i)$, the fractional rotation population of CO_2 in the level J . The quantities $G_J[T(Z_i)]$ and $\nu_D[T(Z_i)]$ are explicitly dependent on atmospheric kinetic (and rotational) temperature $T(Z_i)$, and derive their altitude dependence as the result of altitude dependence of the temperature.

Also note the exponential function $E_1(S_b \tau_j^{ij}(x))$ which occurs in the expression for H_{ij} ; this function relates emission and absorption between layer pairs i and j in a plane parallel atmosphere. This function has been defined and discussed in application to radiative transport in plane parallel atmospheres going back to the days to Milne. The property that $E_1(\tau)$ is proportional to $-\ln(\tau)$ for $\tau \rightarrow 0$ requires the use of the somewhat complicated expression for G_{ij} as given on Fig. 2-7. This expression exploits the fact that $\int_0^\tau d\tau' E_1(\tau') = E_2(0) - E_2(\tau)$ where $E_2(0) = 0.5$ and $E_2(\tau)$ decreases monotonically with increasing τ . This property is exploited by utilization of the escape function E_i as defined on Fig. 2-9. Note the alternate interpretation that $E_i = \sum_j H_{ij}$ in the limit that the j mesh goes to ∞ . Thus on a finite altitude mesh we can easily compute well behaved matrix elements $G_{ij} = -\sum H_{ij} W_i \varrho_j$ for $i \neq j$ and $G_{ii} = 1 - (1 - E_i) \varrho_i + \sum_{i \neq j} H_{ij} W_j \varrho_j$. The quantity ϱ_i is the fraction of de-excitation of the upper level at Z_i due to radiation. Total

PROBABILITY OF ESCAPE FROM LEVEL i

$$E_{ii} = \frac{1}{2} \int_{\sqrt{\pi}}^{\infty} b(z) \varphi(a(z), bx) \sum_B s_B \sum_J g_J(z) \left(E_2(s_B \tau_J^{ij}(x)) + E_2(s_B \tau_J^{iB}(x)) \right)$$

NEAR ZENITH RADIANCE OBSERVED AT z_i GIVEN BY

$$4\pi R(z_i) = W_i^F \Omega_i S_i + \sum T_{ij} W_j(\Omega_j S_j - \Omega_i S_i)$$

ELEMENTS OF THE T_{ij} MATRIX FOR THE CALCULATION OF NEAR ZENITH RADIANCE OBSERVED FROM LEVEL i ARE GIVEN BY

$$T_{ij} = \int_{\sqrt{\pi}}^{\infty} b_j \varphi(a_j, b_j x) \sum_B s_B \sum_J g_J(z_j) e^{-\mu_L^{-1} \tau_J^{ij}(x)} s_B$$

AND

$$W_i^F = \int_{\sqrt{\pi}}^{\infty} \sum_B s_B (1 - e^{-\mu_L^{-1} \tau_J^{iB}(x)}) s_B$$

Figure 2-9 Computation of escape function and transmission function matrix elements

de-excitation is due to the sum of the radiative and quenching processes. This is consistent with the definition of S_i as proportional to the total excitation rate at Z_i in our formulation of the problem. The quantities W_j are weighting factors required to perform the radiative transport integrals over altitude. More detail on the choice of the W_j is given in the paper by Kumer and James (1974). Note here that $\sum_j W_j = \int_{Z_b}^{\infty} \sigma [CO_2] dz = \sigma N_Z$ where $G_J S_B \sigma N_Z$ is the zenith optical depth at altitude Z_b at line center for a line in branch B (where B can be p, q or r) which originates from ground rotational level J. Detailed definitions and properties of the $E_n(\tau)$ can be found in standard texts such as Abramowitz and Stegun (Handbook of Mathematical Functions. U. S. Dept. of Commerce, U. S. Printing Office, Washington, D. C. 1966).

The element H_{ij} then is formed by an integral over all lines in the band, and over all frequencies in each line, it gives the contribution to S_j due to absorption at level Z_j of photons that are emitted from level Z_i . The calculation assumes that the lines in the band are non overlapping, that g_j applies for both the lower and upper states of the band, and that ϕ is the line profile for both absorption and emission at Z_j .

To calculate the solution S_i to the discretized radiative transport equation, equation $\sum_j G_{ij} S_j = S_{0i}$ then requires a computation of the matrix elements as described here and on Figs. 2-7 and 2-8, and a computation of the inhomogeneous term S_{0i} . This followed by a routine calculation of the inverse matrix G_{ij}^{-1} allows for calculation of the S_i via $S_i = \sum_j G_{ij}^{-1} S_{0j}$.

Given the G_{ij} it is easy to use standard matrix inversion routines that have been developed over the years by many different groups for matrix inversion to obtain the elements G_{ij}^{-1} .

The inhomogeneous elements S_{0i} are the result of absorption of earthshine which crosses the lower boundary Z_b , and a second mechanism, collisional

excitation. This second mechanism was discussed in considerable detail in section 2.2.1.

The details of calculating the contribution to S_{0j} due to the absorption of earthshine are given in our earlier papers (Kumer and James, 1974; Kumer 1977a and 1977b). In the present application we have upgraded this calculation to include the altitude dependence of the line shape $\phi(a_i, b_i, x)$ and band shape $G_j(z_i)$.

The Radiance Calculation. Once the non-LTE solution S_j has been computed the next step is to calculate the radiance, as might be observed by a rocket borne sensor in either a zenith or an earthlimb geometry, as is shown in Figs. 2-9 and 2-10 respectively. The formulation shown utilizes altitude dependent line and band shapes.

2.2.3 Further Improvements Required in Our 15 μm CO_2 Model

To date we have implemented the altitude dependent line and band shape formulation, as described in section 2.2.3 above, for just the CO_2 15 μm fundamental band $01^10 \rightarrow 00^00$. In our modeling effort, the results of which are shown on Figs. 2-4, 2-5, and 2-6, we found that hot bands, such as 02^20 01^10 , also contribute significantly to 15 μm CO_2 radiance. For these bands however we remain limited to our older formulation which does not account for altitude dependence in the line and band shapes.

In order to perform detailed spectral modeling of the SPIRE 15 μm data, and of data we anticipate will be obtained in the upcoming experiments such as CIRRIS and SPIRIT, we will need to upgrade our code to account for this effect in all the bands. The code also needs to be upgraded so that all isotopes can be dealt with in a single run rather than a number of separate runs.

At lower altitudes the radiance calculation needs to be modified to account for line overlap. We will show explicit examples of this effect and how it

LIMB OPTICAL DEPTHS

$$\tau_{LJ}^{ij}(x) = \int_{z_j}^{\infty} ds [CO_2] g_j(z) \sigma b(z) \varphi(a(z), b(z), x)$$

ARE COMPUTED BY NESTED LOOPS VIA (BLDTJX):

$$\tau_{LJ}^{ij}(x) = \tau_{LJ}^{i(j-1)}(x) + \int_{z_j}^{z_{j-1}} ds [CO_2] g_j(z) \sigma b(z) \varphi(a(z), b(z), x)$$

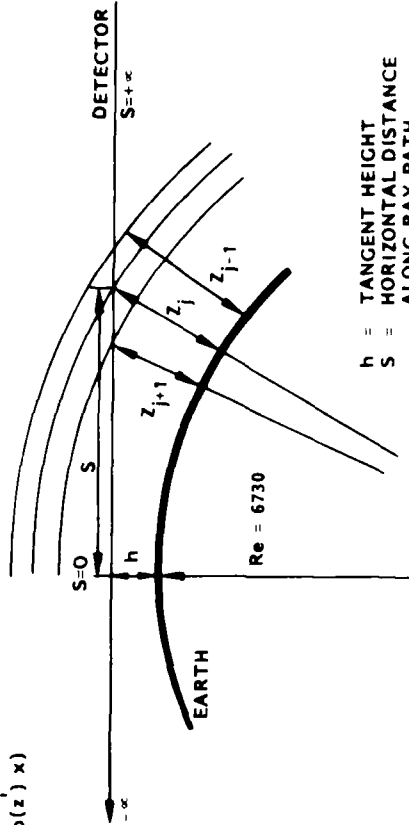
AND THEN (N NESTED LOOPS)

$$T_{LJ}^{LIMB} = \int_{-\infty}^{\infty} dx b_j \varphi(a_j, b_j, x) \sum_B S_B \sum g_j(z_j) (e^{-\tau_{LJ}^{ij}} S_B + e^{-S_B} (2\tau_{LJ}^{ix} - \tau_{LJ}^{ij}))$$

$$w_L^{LIMB} = \int_{-\infty}^{\infty} dx \sum_B S_B (1 - e^{-2\tau_{LJ}^{ix}}(x) S_B)$$

AND FINALLY

$$R-LIMB = w_L^{LIMB} \varrho_i S_i + \sum_{LJ} T_{LJ}^{LIMB} w_j \left(\frac{\partial S}{\partial z} \right)_j (\varrho_j S_j - \varrho_i S_i)$$



- h = TANGENT HEIGHT
- S = HORIZONTAL DISTANCE ALONG RAY PATH
- Z = HEIGHT CORRESPONDING TO DISTANCE S

Figure 2-10 Earthlimb radiance geometry and calculation

impacts analysis of 4.3 μm SPIRE data in section 2.3. The effect will be important in low altitude 15 μm data as well, particularly in the Q-branch region.

2.3 ANALYSIS OF SUNLIT SPIRE 4.3 μm DATA

2.3.1 Data Processing and Comparison

To assist us in this analysis Nadile and Grieder provided us with spectrally integrated SPIRE data on the following spectral pass bands.

Pass Band (μm)	Spectrometer
4.00 - 4.03	HS-2
4.03 - 4.45	HS-2
4.45 - 4.48	HS-2
3.90 - 4.10	NS-2
4.10 - 4.50	NS-2

A comparison of our prediction for spectrally integrated 4.3 μm earthlimb radiance with the spectrally integrated SPIRE NS-2 data for sunlit scans 9 through 12 are shown on Figs. 2-11 through 2-14. The data (curve 1 on Figs. 2-11 through 2-14) are given by

$$D = (0.4 \mu\text{m}) (R_{4.1-4.5} - 415 - R_{3.9-4.1})$$

where $R_{4.1-4.5}$ is the average spectral radiance from 4.1 to 4.5 μm provided to us by Nadile and Grieder and $R_{3.9-4.1}$ is the average spectral radiance from 3.9 to 4.1 μm . The $R_{3.9-4.1}$ is subtracted from $R_{4.1-4.5}$ in order to

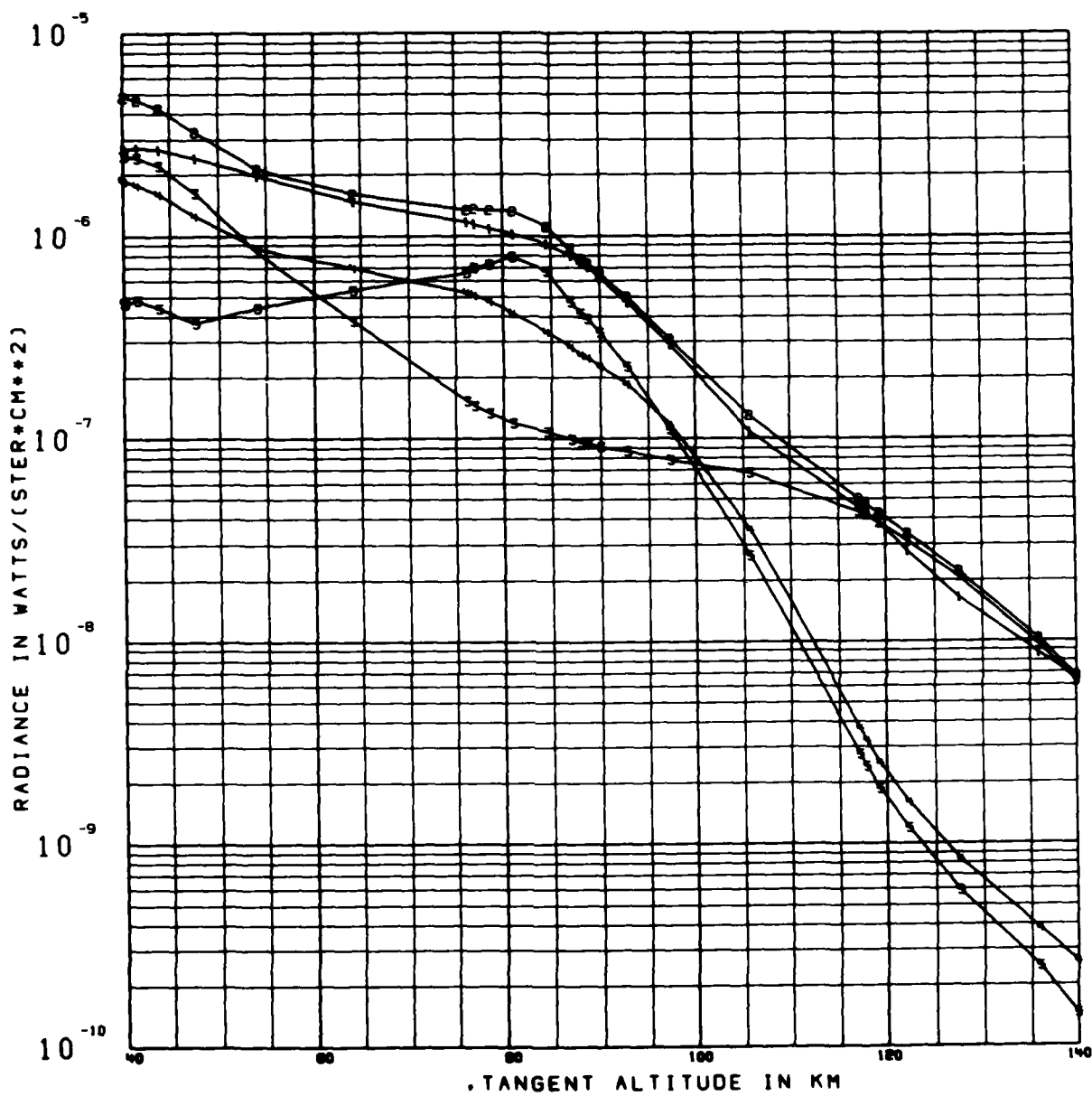


Figure 2-11 The data (curve 1) for scan 9 are compared with our predictions (curve 2). Curve 3 is the component of the predictions due to emission by the 626 CO₂ 001-000 band, curve 4 is the component due to the "weak" bands and curve 5 the solar fluorescence component.

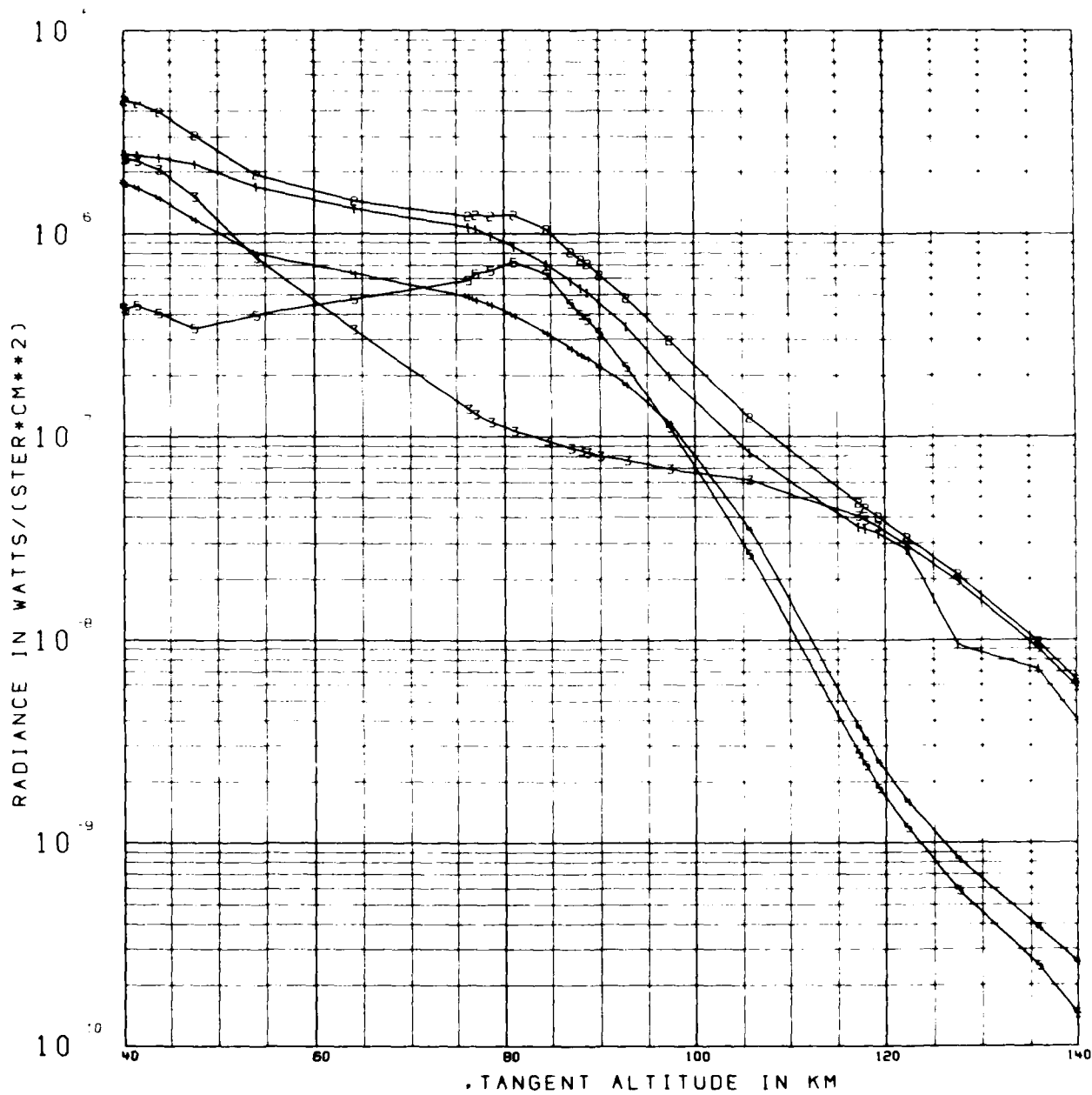


Figure 2-12 Same as Figure 2-11 except for scan 10.

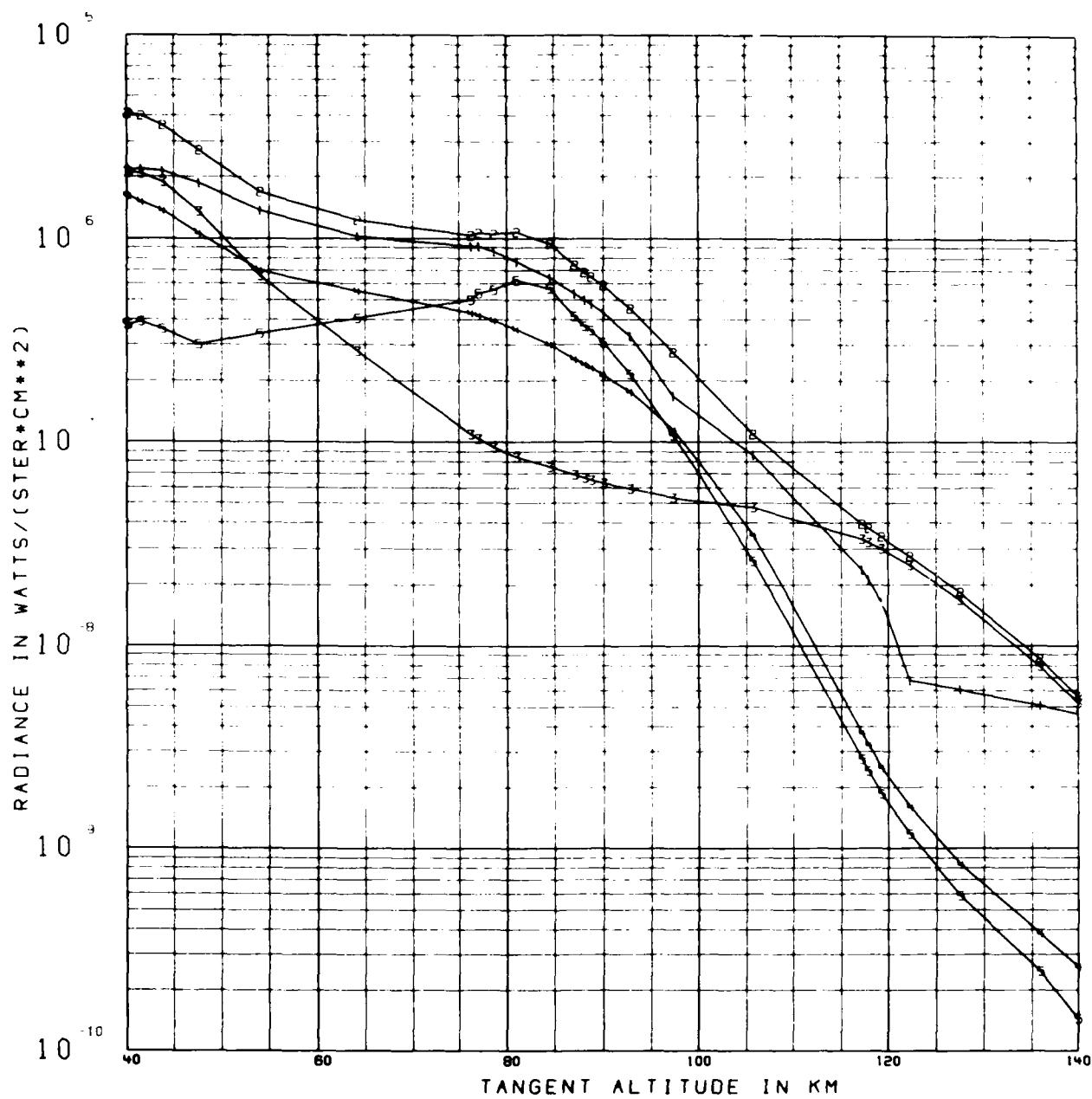


Figure 2-13 Same as Figure 2-11 except for scan 11.

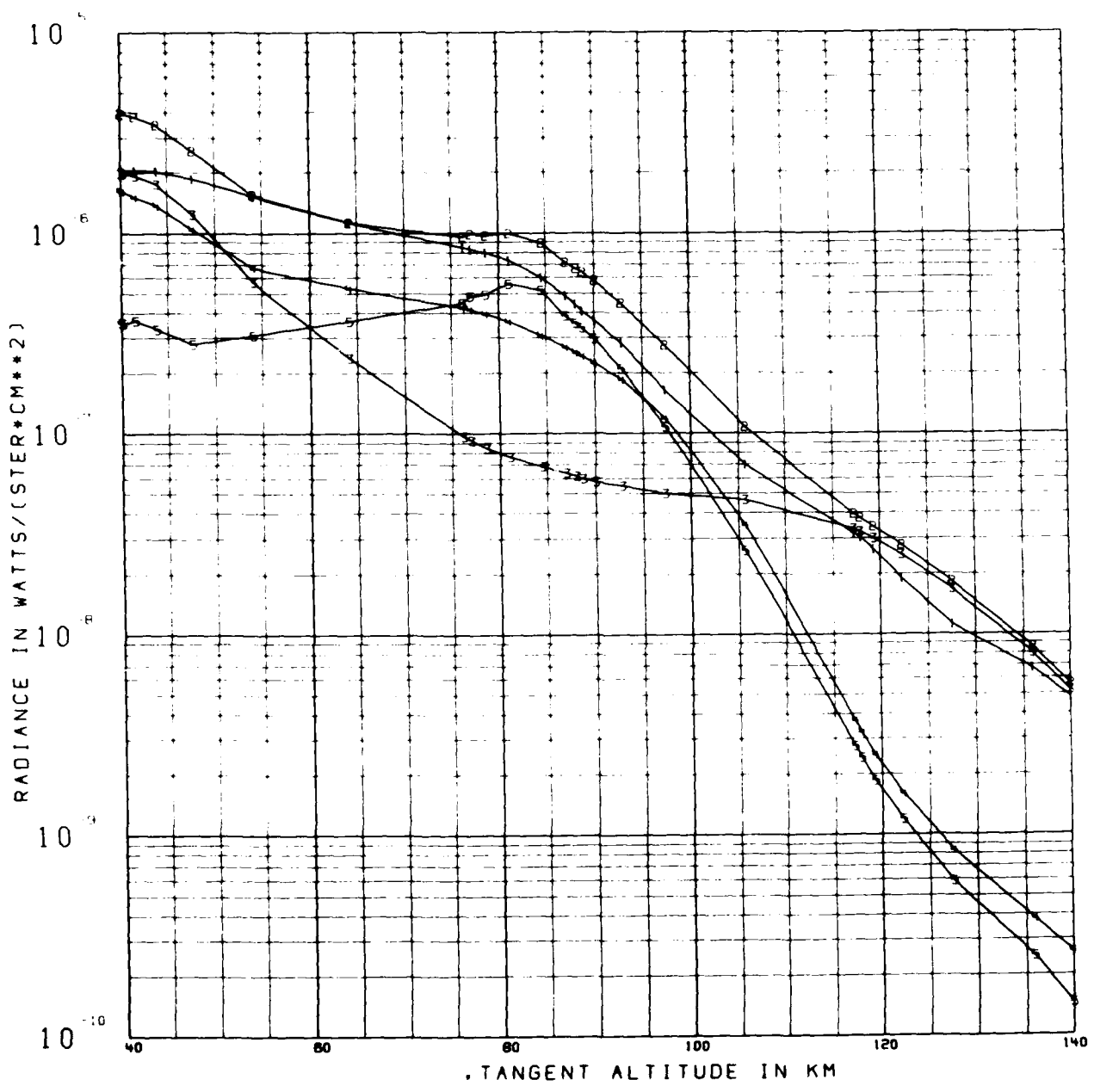


Figure 2-14 Same as Figure 2-11 except for scan 12.

provide a first order correction for DC offset in the spectral data. These predictions for scans 9 through 12 apply for solar elevation data that were also provided to us by Nadile and Grieder. The solar elevation data were a subset of comprehensive SPIRE attitude and trajectory data that were provided by Nadile and Grieder. The solar elevation angle at the tangent point of the sensor line of sight on the 40 to 140 km tangent altitude range are listed for scans 9 through 12 below:

Scan No.	Range of Solar Elevation (deg)
9	13.2 to 9.6
10	11.6 to 7.3
11	6.8 to 4.2
12	10.2 to 0.3

2.3.2 Spectral Composition of the Sunlit CO₂ 4.3 μm Earthlimb

Our predictions for the sunlit CO₂ 4.3 μm earthlimb are labelled by curve 2 on Fig. 2-11 through 2-14, and are broken into components that are curves 3 through 5. Curve 2 is the sum of these components. Some of the bands that we have included in our predictions of the sunlit 4.3 μm earthlimb are listed in Table 2-3. Curve 3 is the contribution from the fundamental band of the major CO₂ isotope, i.e., the 626 001-000 band. Curve 4 is the component that includes the "weak" bands no. 2 through 8 in Table 2-3. The principal excitation mechanism for the components labelled by curves 3 and 4 is the resonance scattering of sunlight, i.e., the absorption of sunlight at 4.3 μm by CO₂ followed by subsequent reemission at 4.3 μm. A number of other mechanisms contribute to the day time 4.3 μm earthlimb as was discussed by Kumer and James (1974). These are listed in Table 2-4 and will be discussed below in more detail in the perspective of their importance to understanding the SPIRE data. Curve 5 is the solar fluorescence contribution which is due to absorption of sunlight by CO₂ at wavelengths shorter than 4.3 μm followed

Table 2-3 THE CO₂ 4.3 μm BANDS

j	CO ₂ (jv ³) Transition	(j)	Isotope	Comment
1	00 ⁰ 1	00 ⁰ 0	626	} Strong Band
2	00 ⁰ 1	00 ⁰ 0	636	
3	00 ⁰ 1	00 ⁰ 0	628	
4	00 ⁰ 1	00 ⁰ 0	627	
5	01 ¹ 1	01 ¹ 0	626	} Weak Bands
6	01 ¹ 1	01 ¹ 0	636	
7	01 ¹ 1	01 ¹ 0	628	
8	01 ¹ 1	01 ¹ 0	627	
9	02 ² 1	02 ² 0	626	
10	02 ⁰ 1	02 ⁰ 0	626	} Fluorescent Bands
11	01 ⁰ 1	10 ⁰ 0	626	

by reemission at 4.3 μm. The contributions to curve 5 include bands 10 and 11 in Table 2-3. These are the contribution from the 626 isotope that result from absorption of sunlight at 2.7 μm followed by reemission at 4.3 μm. Curve 5 also includes contributions from the analogous minor isotopic bands that are not listed in Table 2-3. Other bands which have been included in the calculation labelled curve 5 are those CO₂ 4.3 μm fluorescence bands that result from absorption of sunlight at wavelengths 2.0 and 1.6 μm. The relative importance of these bands will be discussed in more detail below.

Verification that solar fluorescence of 2.7 μm sunlight is a major source of 4.3 μm earthlimb emission was a driving factor for performing the SPIRE experiment. The importance of this mechanism was predicted by James and Kumer (1973). It is seen that the fluorescence is in fact the major contribution near 80 km as was predicted.

Table 2-4 MECHANISMS FOR DAYTIME EXCITATION OF CO₂ v₃ IN THE UPPER ATMOSPHERE

Item	Mechanism
1	Thermal collisions with atmospheric species other than N ₂ .*
2	$N+NO \rightarrow N_2(v>0) + O$
3	$O(^1D)+N_2 \rightarrow O(^3P)+N_2(v>0)$
4	Thermal collisions with N ₂
5	Solar photo electron collisional excitation
6	CO ₂ (J)+hν(4.3 μm)→CO ₂ (Jv ₃), i.e., absorption of 4.3 μm sunlight in the CO ₂ "weak" bands
7	626(000)+hν(4.3 μm)→626(001), i.e., absorption of 4.3 μm sunlight in the fundamental band of the major isotopic specie of CO ₂
8	Absorption of 4.3 μm earthshine by atmospheric CO ₂
9	<p>Absorption of sunlight by CO₂ at wavelengths shorter than 4.3 μm, mainly at 2.7 μm but absorption at wavelengths 2.0 and 1.6 μm have also been included, to produce the combination states CO₂(Jv₃), next the J portion of the combination state is passed to CO₂ via a resonance collisional transfer, i.e.</p> $CO_2(Jv_3)+CO_2 \rightarrow CO_2(J)+CO_2(001)$ <p>, or CO₂(001) is obtained by the circuitous process;</p> $CO_2(Jv_3)+N_2 \rightarrow CO_2(J)+N_2(v=1)$ $N_2(v=1)+CO_2 \rightarrow N_2+CO_2(001)$ <p>, in each case the end product of interest is CO₂(001).</p>

*The mechanisms above, exclusive of mechanism 6, have been discussed in detail by Kumer and James (1974); mechanism 6 has been discussed in detail in papers by Kumer (1977ab).

It is also seen that the "weak" bands contribute approximately the same amount to the limb radiance near 80 km as does the fluorescence component. Both the "weak" band and the fluorescence emission dominate the contribution due to the 626 001-000 band for altitudes less than 100 km. The "weak" band contribution to the sunlit CO₂ 4.3 μm earthlimb emission was not addressed in the original James and Kumer (1973) paper, but its importance could be inferred from the later papers by Kumer (1977a and 1977b). Analogously, Caledonia, Green, and Murphy (1982) point out that the weak bands are the dominant contributors to CO₂ 4.3 μm emission that is observed in laboratory experiments that involve heavily self absorbed CO₂ mass path lengths. Here, our analysis of the SPIRE data indicates that the 4.3 μm CO₂ mass path for earthlimb geometry is large enough to produce significant effects for altitudes less than or equal to approximately 110 km. The pertinent effect is that the "weak" bands make up almost 1/2 of the 4.3 μm daytime earthlimb emission on the tangent altitude interval from approximately 55 to 95 km.

2.3.3 General Discussion of the Comparison of the Data and the Predictions

Here we note that although the data vary by more than 2 orders of magnitude on the range 40 to 140 km tangent altitude, our predictions are never significantly more than a factor of 2 in disagreement, and for the most part agree better than that with the data. There are several cases in the overall comparison of the predictions and data for the four scans where disagreement is more obviously marked, and we will discuss these cases here in general, and then in subsequent discussion in more detail.

First we note relatively large disagreement between prediction and data in the high altitude end of scans 10 and 11. Inspection of the predictions for all four scans and of the data for the presumably better behaved scans (9 and 12) would argue that the discrepancy can be attributed to noise, or perhaps an effect of the variation of the DC level, and therefore, should be discounted.

Secondly, we note a sharp disagreement between prediction and data at lower tangent altitudes beginning at 54 km and becoming very noticeable at 40 km in all cases. We are reasonably sure that this results from a breakdown in our assumption of non-overlapping lines in the calculation of earthlimb radiance for tangent altitudes less than ~ 55 km. We discuss this point, and a method to remedy the situation in detail in section 2.3.7 below.

Third, there appears to be a general tendency for over prediction of varying significance on the entire tangent altitude range from 55 to 140 km for the four scans. This apparent discrepancy is not particularly serious (typically much less than a factor 2) and here we briefly consider several alternative possibilities to improve on this situation; (a) the generally mild overprediction on the approximate range ~ 80 to 140 km would be reduced if we would use the Hays and Olivero (1970) CO_2 mixing ratio model, which breaks away from and becomes less than the constant altitude value of 3.2×10^{-4} at 80 km, rather than at 100 km, which is the model we have employed for generating our predictions on Figs. 2-11 through 2-14; (b) next, there is a possibility that the solar flux is less than the value that we used in the calculation, i.e., there may be solar absorption lines coincident with the CO_2 atmospheric absorption lines near $4.3 \mu\text{m}$; we have considered this possibility to the extent that we have looked at papers such as that of Mount and Linsky (1975) which indicate that it is very doubtful that there is enough CO_2 in the solar atmosphere to cause the required absorption in the lines of the fluorescent and weak bands that dominate the $4.3 \mu\text{m}$ earthlimb from ~ 50 up to ~ 105 km, and have concluded that this explanation is very unlikely; (c) next, we have also considered the possibility that the entire scan pattern of the SPIRE experiment was rotated further away from the sun than was determined by AFGL personnel on the basis of star sensor and other data. Here we consider item (c) in summary.

We discuss the issue of possible azimuthal misregistration in detail in section 2.3.8 below. Attitude sensor systems on the SPIRE did experience some problems. Vertical positioning was solved to better than 5 km accuracy on all the scans by the utilization of prominent and well known features in spectral

earthlimb emission. The comparison between data and predictions on Figs. 2-11 through 2-14 indicates generally that vertical registration of the SPIRE data was indeed better than 5 km in accuracy. The general overprediction seen in Figs. 2-11 through 2-14 suggests the average in whatever vertical misregistration that there may have been should shift the data upwards relative to the predictions.

The problem is somewhat more difficult for the azimuthal case. We looked into this possibility in some detail, and report on it in section 2.3.8 below. Here we summarize that our study was not absolutely conclusive but seemed to indicate that a major error in azimuthal registration of the SPIRE scan pattern is not likely. Again, the overprediction noted in Figs. 2-11 through 2-14 suggests that if there is any average misregistration in the SPIRE azimuth, it should be away from the sun to reduce the predictions relative to the data.

Finally we believe that the most likely explanation for the general overprediction might be the simple result of some inaccuracy in the radiometric calibration of the SPIRE instrument, and that the small scan to scan variations in the qualitative comparison between the data and the predictions might be the effect of some minor scan to scan misregistration in both the vertical and in the azimuthal registration of the altitude of the SPIRE.

2.3.4 Mechanisms for CO₂ 4.3 μm Fluorescence

In discussion above it has been pointed out that 4.3 μm fluorescence of sunlight is a major mechanism for the 4.3 μm earthlimb on the ~ 60 to ~ 100 km tangent altitude range. Here we discuss that mechanism in a little more detail. The James and Kumer (1973) work was limited to just the CO₂ 626 fluorescence originating from absorption of 2.7 μm sunlight. Recently Sharma and Nadile (1981) have shown that fluorescence of ~ 2.0 μm and ~ 1.6 μm sunlight is important for explaining the 2.7 μm SPIRE data. This suggested that we could improve on our previous work by quantitatively accounting for

this effect at 4.3 μm . Also it has been seen above, and it also has recently been recognized by a number of workers in the community, that contributions from minor isotopic species such as CO_2 636, 628, and 627 can be very important in the formation of CO_2 earthlimb emission.

In the work we report here we have accounted for these effects on the 4.3 μm earthlimb fluorescence. On Fig. 2-15 we show for scan 9 the contributions to 4.3 μm earthlimb fluorescence from these sources. Curve 1 on Fig. 2-15 is the contribution from fluorescence of 2.7 μm sunlight by CO_2 626, i.e., the mechanism considered previously by James and Kumer. Curves 2 through 4 illustrate the contribution of the CO_2 isotopic species 636, 628, and 627 respectively. Curves 5 and 6 show the contributions due to CO_2 fluorescence of 2.0 and 1.6 μm sunlight respectively.

It can be seen that these additional sources of CO_2 4.3 μm fluorescence can not be completely neglected. Curve 5 on Figs. 2-11 through 2-14 above is the sum of the six components shown on Fig. 2-15. Although these additional sources of fluorescence as defined in this section are not particularly important for the 4.3 μm earthlimb, the analysis by Sharma shows that they should indeed be of major significance for the sunlit 2.7 μm earthlimb.

2.3.5 Mechanisms for the Sunlit Earthlimb Emission at 4.3 μm

The mechanisms for excitation of CO_2 (Jv_3) are shown in Table 2-4. The contribution for scan 9 of each mechanism to the quantity $S(\delta N)$ (which is proportional to the excitation rate of the upper state 626 001 of the fundamental CO_2 4.3 μm band of the major isotope) is shown on Fig. 2-16. We see that absorption of sunlight (in one way or another) is the dominant mechanism all the way down to approximately 55 to ~ 65 km where the oxygen singlet D mechanism begins to become dominant. The contribution by the ^1D mechanism to the 626 001-000 band limb radiance is shown on Fig. 2-17. It is seen that evidence for any serious discrepancy between our model for

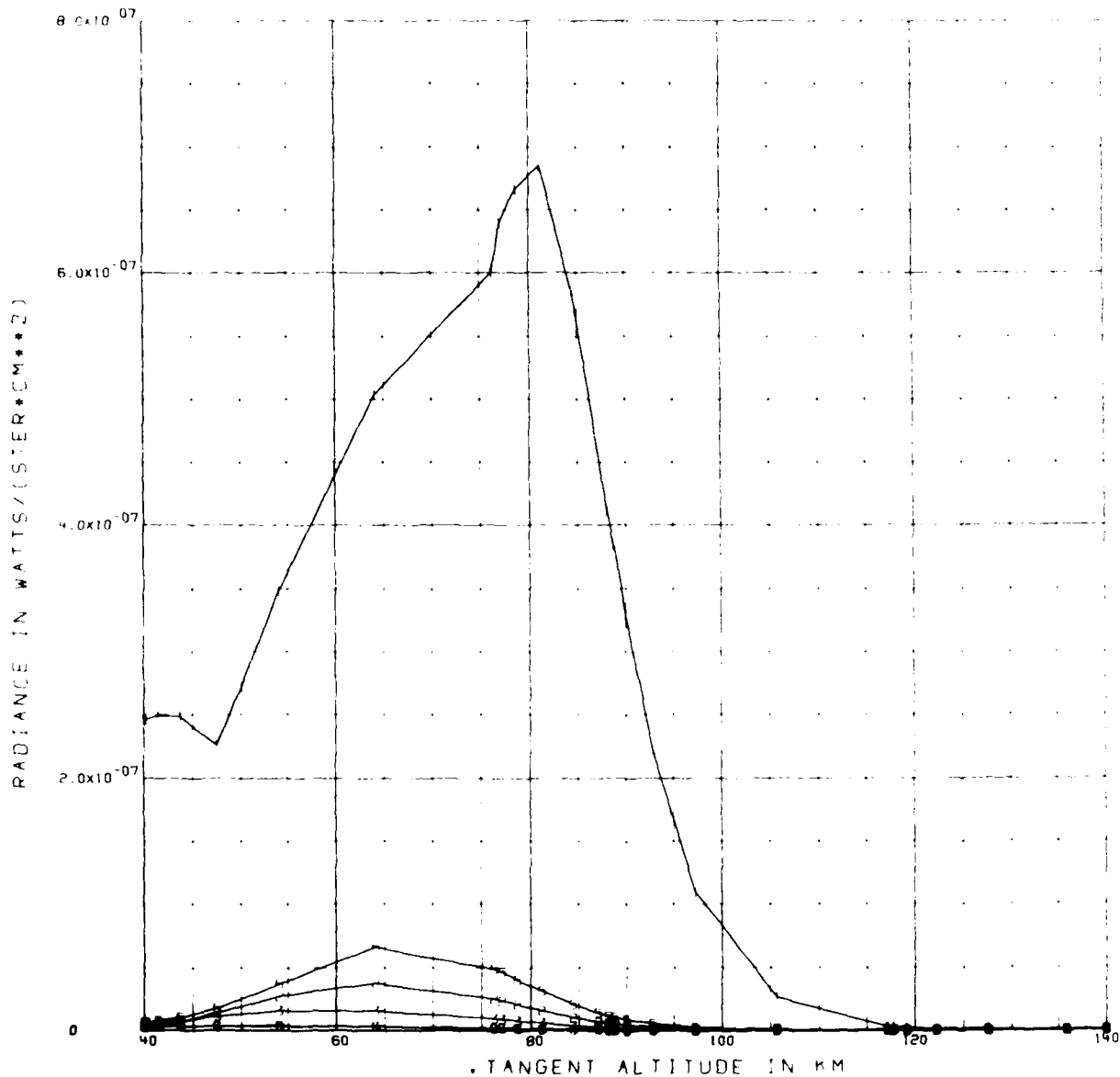


Figure 2-15 Contributions to CO₂ 4.3 μm earthlimb fluorescence. Curves 1 through 4 are due to fluorescence of 2.7 μm sunlight by the species 626, 636, 628 and 627 respectively. Curves 5 and 6 are due to fluorescence of 2.0 and 1.6 μm sunlight respectively.

CONTRIBUTION TO 001-000 EMISSION BY MECHANISM

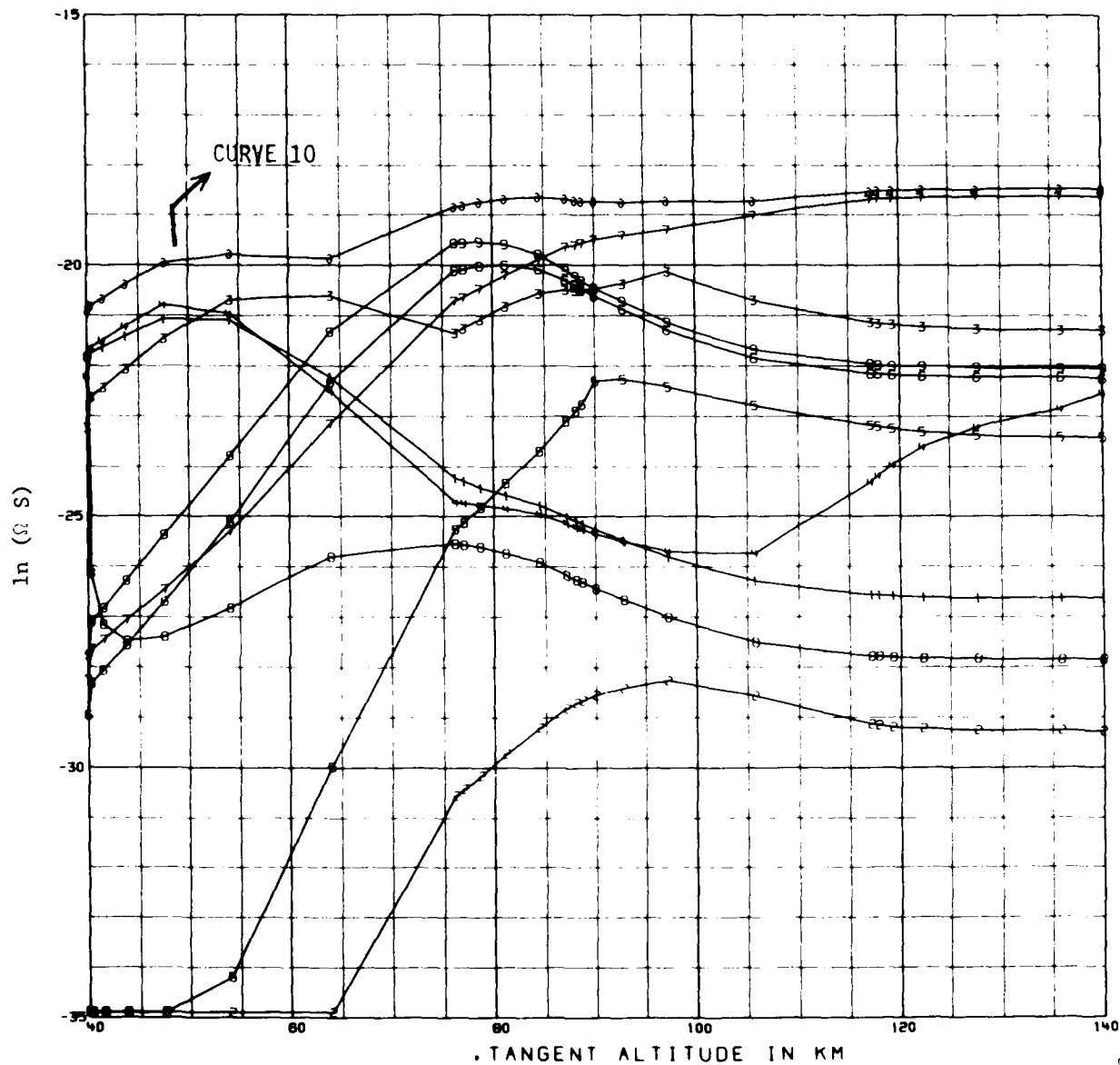


Figure 2-16 The contributions from each of the mechanisms numbered 1 through 9 on table 2-4 to the quantity, $626\ 001-000\ 4.3\mu\text{m}$ emission/ $(\sigma [\text{CO}_2])$, are plotted (curves 1 through 9 on the figure) as a function of altitude. Curve 10 is the sum of these contributions.

CONTRIBUTIONS TO 001-000 BY MECHANISMS

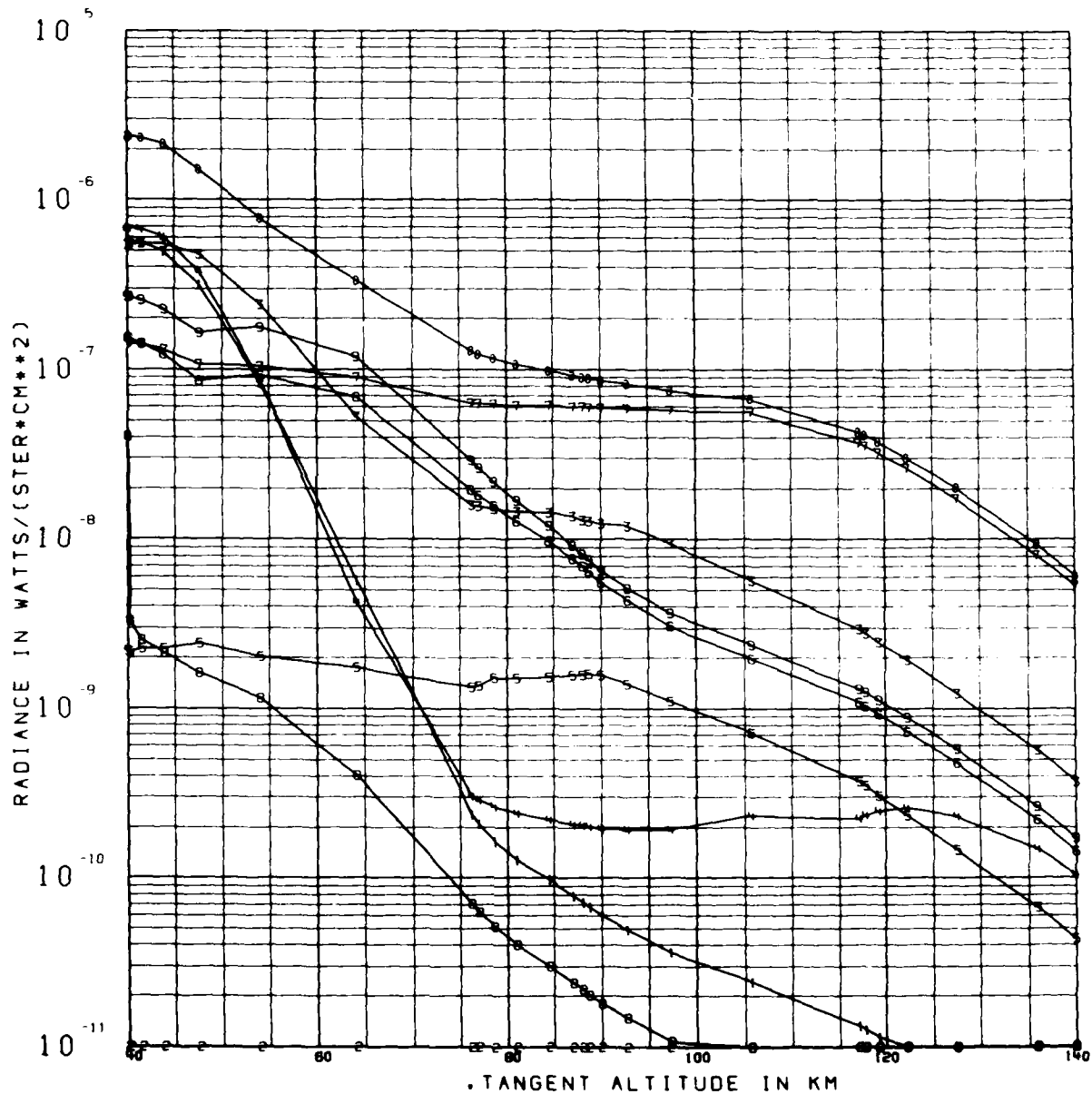


Figure 2-17 The contributions from each of the mechanisms numbered 1 through 9 on table 2-4 to the quantity, 626 001-000 $4.3\mu\text{m}$ earthlimb radiance, are plotted (curves 1 through 9 on the figure) as a function of altitude. Curve 10 is the sum of these contributions.

oxygen singlet D mechanism and what is actual reality would show up in the comparison of our predictions and the data in the range 55 to 65 km tangent altitude. Our model for this mechanism is given in our paper (Kumer, 1977a).

Considering that anything very much different from our model (in the sense that it could be considerably more than our model predicts) would show up in the low altitude data, and it does not. We believe that our model is perfectly adequate for consistent interpretation of the SPIRE data, and we see no evidence in these data for any $O(^1D)$ model that is very much different from ours. We must add that there are a number of factors to be considered when judging the applicability of any model for the $O(^1D)$ mechanism. The product of the $O(^1D)$ production rate with the efficiency for transfer of excitation of vibration to N_2 is the pertinent quantity. Production of $O(^1D)$ depends on the O_3 number density and in this case an inaccurate O_3 density (too large or too small) could be compensated for by an inaccurate choice (in the opposite direction) for the efficiency. Our bottom line here is that agreement with the data that we get with our present model argues that changes to our present model for the $O(^1D)$ mechanism are probably not warranted.

2.3.6 Vibrational Temperatures

Vibrational temperatures and atmospheric kinetic temperature for scan 9 are plotted on Fig. 2-18. Curve 1 is the atmospheric kinetic temperature. Curve 2 is the N_2 vibrational temperature. Curves J+2 designated the vibrational temperature of the $4.3 \mu m$ CO_2 band designated by J in Table 2-3. For example curve 3 is the vibrational temperature of the 626 CO_2 (001) state. Curve 8 is the vibrational temperature of the 636 CO_2 (011) state, etc. The vibrational temperatures are defined by

$$T = -1.439 v' / \ln(B) \quad (2.3)$$

where B is defined by

KIN. AND VIB. TEMPERATURES

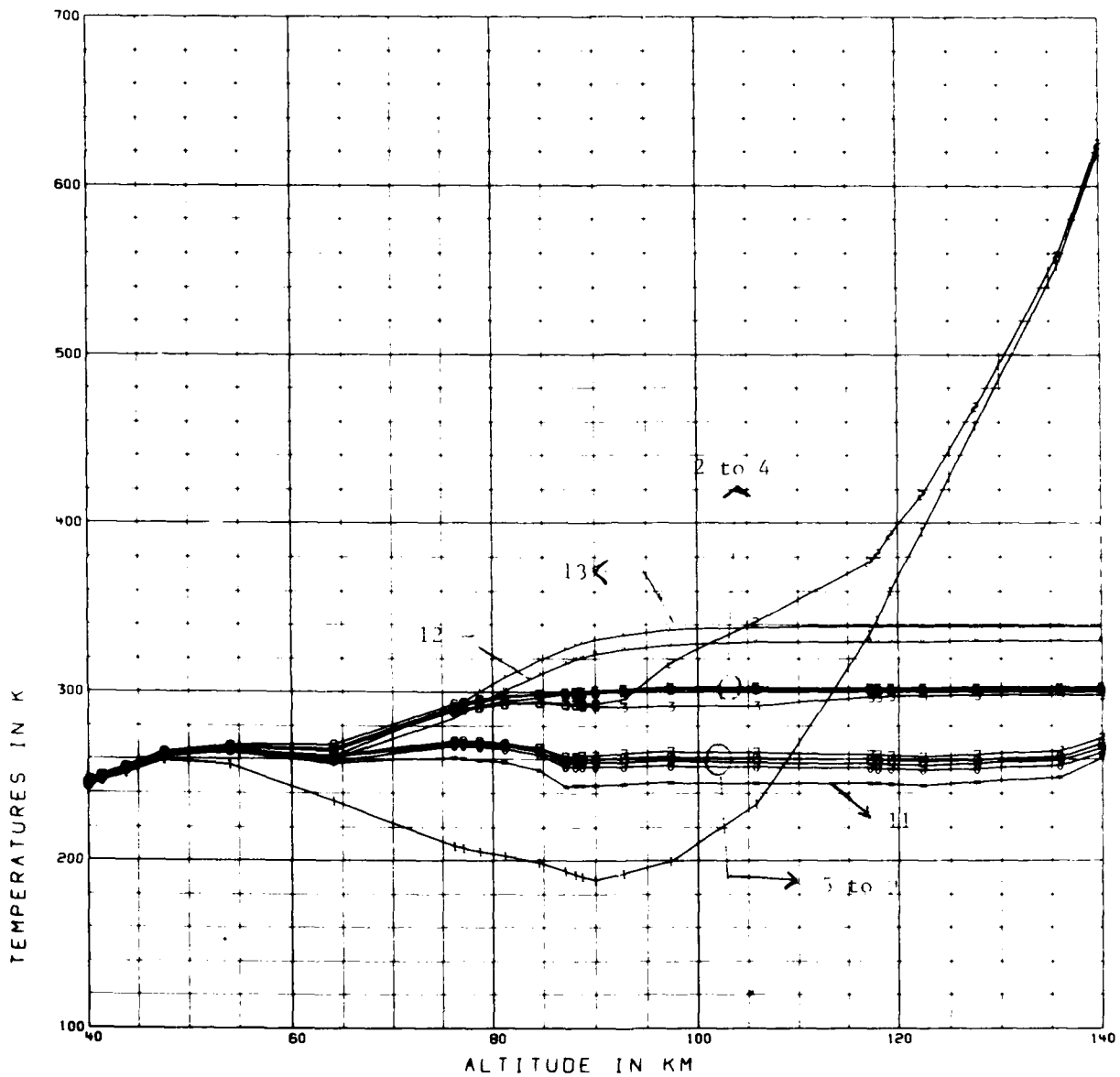


Figure 2-18 Vibrational temperatures and atmospheric kinetic temperature for scan 9 are shown plotted on the figure . The curve labelled by 1 is the atmospheric kinetic temperature. The curve labelled by 2 is the N₂ vibrational temperature. Curves labelled by J+2 designate the vibrational temperature of the 4.3 μm CO₂ band J in table 2-3 above .

$$[CO_2 (Jv_v)] = g' B [CO_2 (000)] \quad (2.4)$$

and where v' is the upper state energy in units cm^{-1} , g' is the degeneracy of the upper state. The standard that $[x]$ symbolizes the number density of the species x is utilized above. For N_2 the definition of vibrational temperature is given by Eq. (2.3) above with B given by

$$[N_2 (V = 1)] = B [N_2]$$

The vibrational temperatures listed on Fig. 2-18 were calculated by methods and techniques described in the (1977a) paper by Kumer. The radiance predictions, which agree very well with the SPIRE data (see Fig. 2-11 through 2-14 above) as is discussed above, are related to these vibrational temperature calculations in that they specify the excited state populations that are used in the calculation of the radiances. We believe this good agreement between our predictions and the data provides confirmation of our model for the daytime CO_2 atmospheric emission processes and confirmation for our predictions for daytime CO_2 and N_2 vibrational temperatures that were published in the (1977a) paper.

2.3.7 Band and Line Shape Altitude Dependence in the Limb Radiance Calculation

Referring to the discussion of radiance calculation that appears in section 2.2.3 we note that our 4.3 μm model has not been completely upgraded to include the effect of altitude dependence in the line and band shapes as has been done for the CO_2 626 010-000 band in our 15 μm model. Such an upgrade of the 4.3 μm model would involve considerable effort and was beyond the scope of the effort we report here. One of the problems with upgrading the 4.3 μm model is that so many bands are important, i.e., the fundamental band becomes relatively unimportant for altitude < 100 km for example. We did, however, find a way to approximately account for line and band shape altitude dependence in the 4.3 μm radiance calculation for all the bands by

utilizing an analytic approximation for the transmission function matrix elements that appear on Fig. 2-10. This approximation can be inferred from the work of Neuendorffer (1982) on developing an analytic expression for the absorption of a single non-overlapping line for a given mass path length of absorber gas, and a mass averaged (over the path length) value for the pressure broadening parameter and for the Doppler width of that line. The Neuendorffer approximation is an improvement over previous analytic approximations in that it is generally applicable through both the optically thick and the thin regime, and in that it may be utilized for arbitrary ratio of Lorentz to Doppler broadening. It is restricted to homogeneous paths, but can be applied to the earthlimb case by replacing the inhomogeneous earthlimb mass path with an equivalent homogeneous pseudo-mass path specified by the inhomogeneous earthlimb mass path averaged values of pressure (Lorentz) and Doppler broadening.

To verify the Neuendorffer approximation and to illustrate the expected effect on the $4.3 \mu\text{m}$ radiance calculation we show on Fig. 2-19 several calculations of the earthlimb width function for the 626 001-000 band that differ in the assumptions that are employed in the specification of band and line shape. The width function for a CO_2 band is defined on Fig. 2-9 above. The physical significance of the width function is that a good approximation to the earthlimb radiance is given by the product of the width function calculated along an earthlimb viewing line of sight for a specific tangent altitude and the emission source function value at the tangent point. The emission source function is the quantity s that is defined in section 2.2. On Fig. 2-19 curve 1 is the quantity σN for earthlimb geometry, plotted as a function of tangent altitude. In the optically thin case the width function is equal to σN independent of the band shape and of the value used for Doppler and/or Lorentz widths; this is seen to be the case for tangent altitudes ≥ 130 km for the 626 001-000 band for earthlimb viewing geometry.

The width function calculations shown on Fig. 2-19 are characterized by parameter "a," called the Lorentz parameter, that is defined as the inverse of the Doppler e-fold $1/2$ width divided by the Lorentz half width at half max.

The width function calculations presented on Fig. 2-19 differ by the value of "a" that is used for each calculation, and by the distribution of rotational levels, which determine bandshape, that is used for each calculation. Curve 2 was computed on the assumption that $a = 10^{-3}$ over the entire tangent altitude range. Curve 2 was computed by the methods we have discussed previously (Kumer and James, 1974). Curves 3, 4, and 5 were calculated by the Neuendoeffler approximation. Curve 5 was calculated for the pure Doppler case i.e., $a = 0$ over the entire altitude range; Curve 4 was calculated for the same condition as curve 2, i.e., $a = 10^{-4}$, and curve 3 was computed by utilizing a mass averaged altitude dependent value of "a" that is plotted on Fig. 2-20. For curves 2, 4, and 5 the band and Doppler line shape are set to be given by 225 deg, considered to be generally representative of mesospheric conditions. Curve 3 is the most realistic case. For curve 3 the altitude dependence of the line shape is accounted for by combining the Neuendorffer analytic approximation with mass averaging. The altitude band shape dependence due to temperature variation is also accounted for by utilizing mass averaging to assign a mean temperature to each limb viewing path (this procedure is identical with that used to assign a Doppler width to each limb viewing path).

The agreement between curves 2 and 4 provides mutual verification for our previous method and for the Neuendorffer analytic approximations. The comparisons indicate that there may not be a lot of effect on the CO_2 626 001-000 $4.3 \mu\text{m}$ radiance calculation due to altitude dependence of line and band shape above approximately 80 km. However, below 80 km it would appear that there should be a large effect due to the increasing pressure broadening with decreasing altitude. One would expect this since in first approximation the radiance is given by the product of the width function and the emission source function S . This effect is illustrated by curve 3.

A comparison of the data for scan 9 and our predictions is shown on Fig. 2-21. The predictions shown on Fig. 2-21 differ from those shown on Fig. 2-11. For predictions shown on Fig. 2-11, the altitude dependent value for "a" as shown on Fig. 2-20 was used in a Neuendorffer like calculation

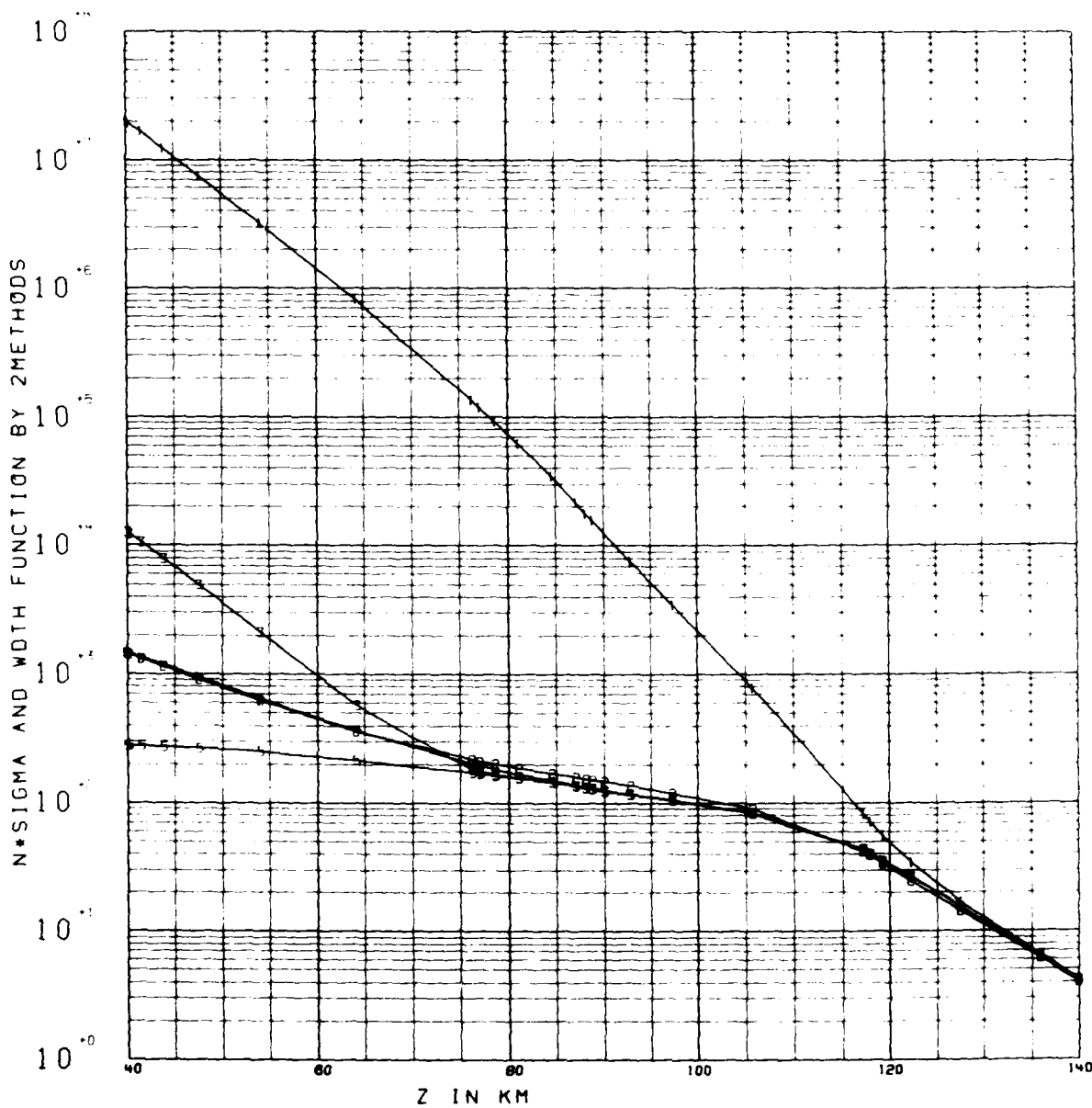


Figure 2-19 The quantity σN_L (curve 1) for earthlimb geometry and the earthlimb viewing width function $W(\sigma_N)$ that is calculated by utilizing various assumptions for the line and band shapes as discussed in the text are plotted on this figure as a function of tangent altitude. Curves 2, 4 and 5 use altitude independent line and band shapes, curve 3 uses a more realistic altitude dependent "earthlimb path mass averaged" line and band shape .

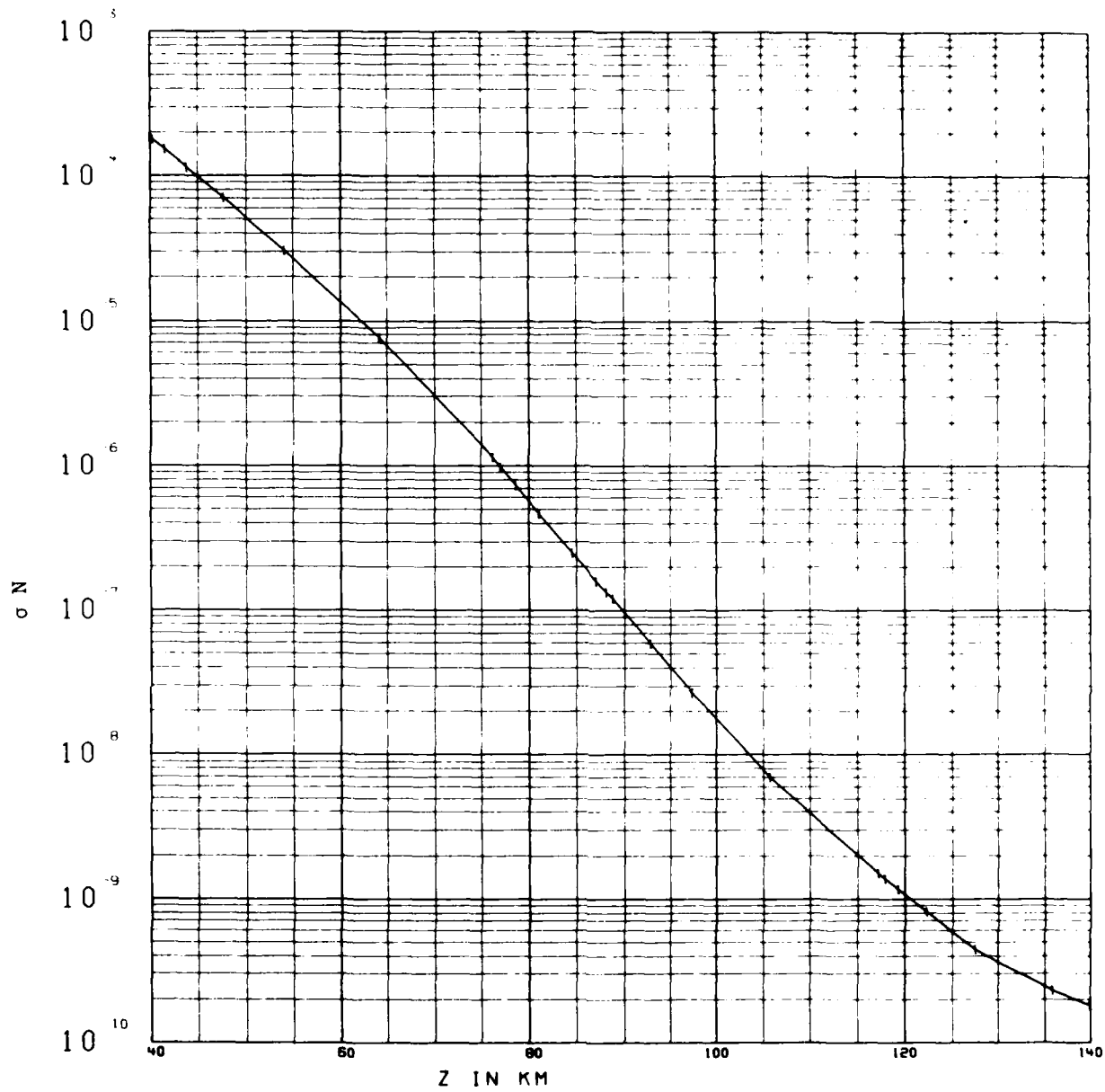


Figure 2-20 The "earthlimb path mass averaged" value for the Lorentz parameter is plotted versus tangent altitude.

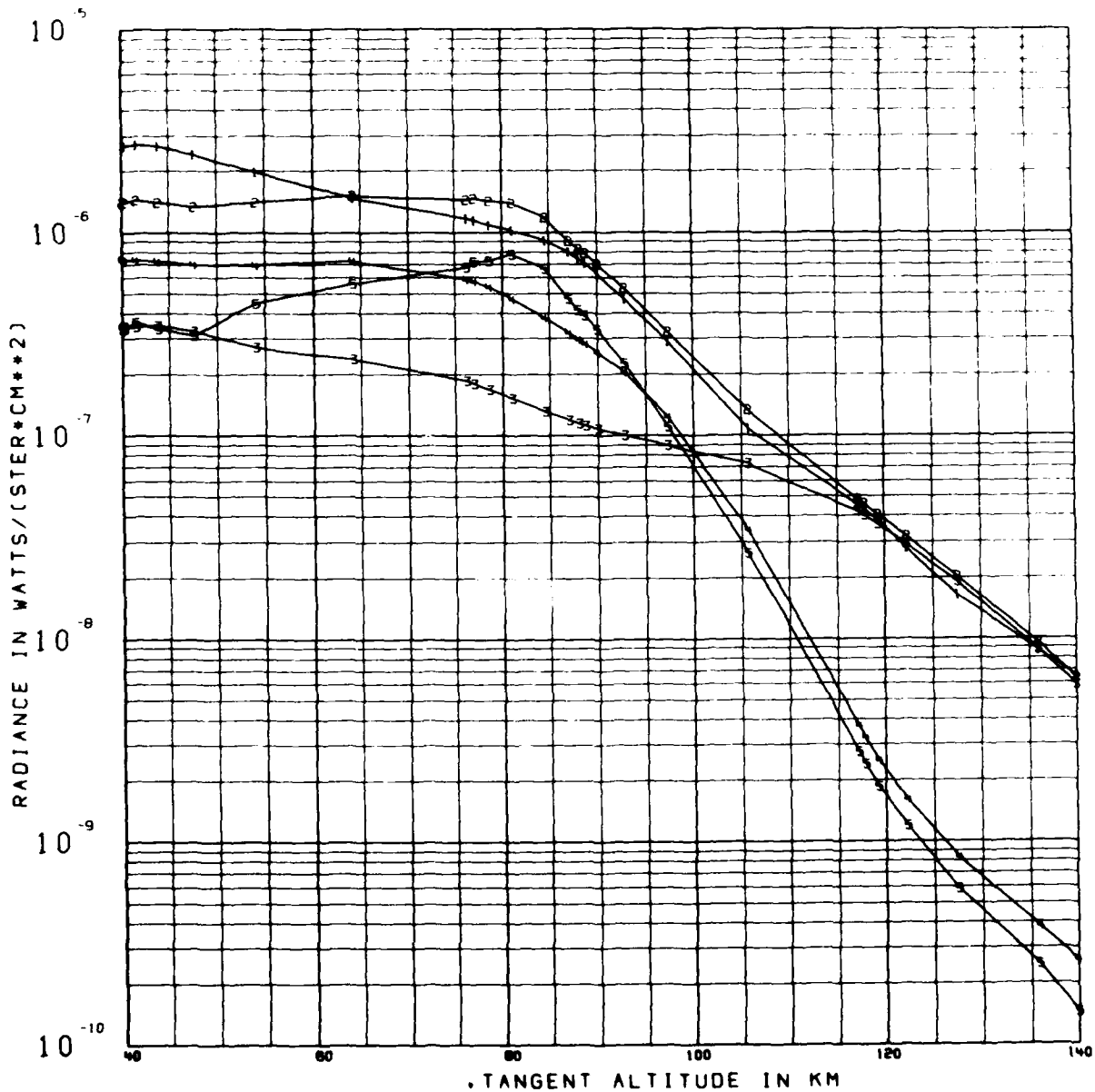


Figure 2-21 Same as Figure 2-11 except in this case the calculation utilizes the same altitude independent line and band shapes that were utilized above in the calculation of the width function curves 2 and 4 on Figure 2-20 . By contrast the the more realistic "earthlimb path mass averaged" line and band shapes were used for the calculations shown on Figure 2-11 through Figure 2-14 .

accounting for altitude dependent band and line shape variation of the transmission function matrix elements (these are defined on Fig. 2-10). This is required to achieve an "exact" limb radiance calculation as defined on Fig. 2-10. By contrast the altitude independent band shape, and line shape characterized by $a = 10^{-3}$, is used in the calculation of the transmission function matrix elements that were used to produce the predictions that are shown on Fig. 2-21.

By inspection of the comparison between data and prediction on Fig. 2-11 with that on Fig. 2-21, it is seen that better agreement can indeed be obtained between the data and the predictions, all the way down to about 53 km tangent altitude, by use of the more realistic calculation which takes into account the altitude dependence of the band and line shapes. Below 53 km the predictions on Fig. 2-11 rapidly become much greater than the data. This happens because our model utilizes the assumptions of non-overlapping lines. This is a good assumption above 53 km but at lower altitudes this assumption begins to break down. For example the square equivalent width of the strongest line of the 626 001-001 band is about 1.3 cm^{-1} for the 40 km tangent altitude limb viewing path; this is to be compared with the average line spacing of about 1.6 cm^{-1} in that band. In this case then (according to the assumption of non-overlapping lines) all of the lines of the weaker bands that are located in the same spectral region as the strong line are incorrectly making an additional contribution to the limb radiance at 40 km.

This is not the case at higher altitudes since it can be shown that the equivalent square width of the strong lines varies like $\exp(-z/h)$ where h is the atmospheric scale height (for saturated lines with strong Lorentz wings as is the case for strong lines of the 626 001-000 band near 40 km). In this case a line that is 1.3 cm^{-1} wide at 40 km slims out to about 0.13 cm^{-1} equivalent width at approximately 55 km. This is considerably less than the average line spacing in band. Considering the number and relative strength of the weaker bands that are contributing, it becomes reasonable that the non-overlapping assumption is adequate for altitudes $> 55 \text{ km}$. This is

adequate for altitudes 755 km. This is verified to be the case by the comparisons of our predictions with the data that are shown on Fig. 2-11 and Fig. 2-21.

On Fig. 2-11 the discrepancy between theory and data below approximately 55 km could be reduced by using a radiance calculation that takes line overlap into account. One way to do this might be to modify LOWTRAN so that we could supply the non-LTE CO₂ vibrational temperature for the calculation of the Planck black body radiance (which is required for calculation of the atmospheric radiance by LOWTRAN) and at the same time maintain the standard LOWTRAN procedure of utilizing the atmospheric kinetic temperature for the calculation of atmospheric transmissivity that is also required for the LOWTRAN calculation of the radiance. This is a promising approach to obtaining better agreement with the data in the 55 to 40 km region that we were not able to pursue in the scope of the current effort. We believe this would be a useful task to pursue in future efforts.

2.3.8 Possibility for Azimuthal SPIRE Scan Pattern Misregistration

In section 2.3.3 we mentioned that our predictions were generally slightly larger than the data (see Figs. 2-11 through 2-14). Here we explore the possibility that the solar elevation angles appropriate for analysis of the SPIRE data may be smaller than is currently accepted due to some inadvertent azimuthal misregistration of the SPIRE scan pattern. Since the directional data for SPIRE pointing were somewhat degraded, this possibility does have some viability as pointed out above. The SPIRE data have been well calibrated vertically by AFGL personnel by using prominent atmospheric infrared features such as the OH maximum, the HNO₃ maximum, the CO₂ 4.3 μm knee, etc. The azimuth however may not be as well calibrated, thus an azimuthal rotation of the entire SPIRE scan pattern (the pattern with currently accepted azimuth is shown in page 205 of the AFGL Technical Memo. AFGL-TM-18, Nadile, 1979) towards the night side would result in lower solar elevation angles for the sunlit scans than are currently accepted.

On the basis of the currently accepted SPIRE scan pattern azimuth Nadile and Grieder predict a solar elevation angle 7.7° for tangent point of the earth's surface for scan 11 (the closest of the sunlit scans to the dark region). However when we plot the window region $3.9\text{--}4.1\ \mu\text{m}$ data versus tangent altitude down to negative tangent altitudes (i.e., for looking at the hard earth) it appears (see Fig. 2-22) that scan 11 much more closely resembles the dark data than the sunlit data. This might suggest that the solar elevation at ground level for scan 11 is less than the nominal 7.70° .

This same behavior is not conclusively mirrored in other window spectral regions of the SPIRE data however. For example, AFGL personnel find that in the $2.2\ \mu\text{m}$ window region, the radiance in the earth viewing dark scans that is below NESR; is heavily saturated for the sunlit scans 9, 10, and 12, but fairly mildly saturated for scan 11. Since scans 9, 10, and 12 are heavily saturated, it is difficult to tell whether these represent full sun and scan 11 a terminator case (essentially zero solar elevation angle) or not.

Similarly, AFGL personnel have looked at the SPIRE data in the $3.65\ \mu\text{m}$ region, here scan 11 is an order of magnitude brighter than for the dark scans. It is not clear that the $3.65\ \mu\text{m}$ data represent reflection of $3.65\ \mu\text{m}$ sunlight from the earth or solar pumped non-LTE emissions of CH_4 and O_3 at altitude, (i.e., the effective earth shadow height could be several km high) so again it is difficult to use these data to draw hard conclusions on what the solar elevation angle might be for scan 11.

Our predictions for the $4.3\ \mu\text{m}$ earthlimb radiance for solar elevation angles calculated on the assumption that the SPIRE scan pattern was in fact rotated $14\ \text{deg}$ further away from the sun (i.e., in the counter clockwise direction as viewed in the perspective of the figure on page 205 of the Memo AFGL-TM-18 that was cited above) than is currently believed to be the case are shown compared against the data for scans 9 through 12 on Fig. 2-23 through 2-26. It can be seen that the predictions that are based on the rotated case (i.e., those shown on Figs. 2-23 through 2-26) do indeed match with the data slightly

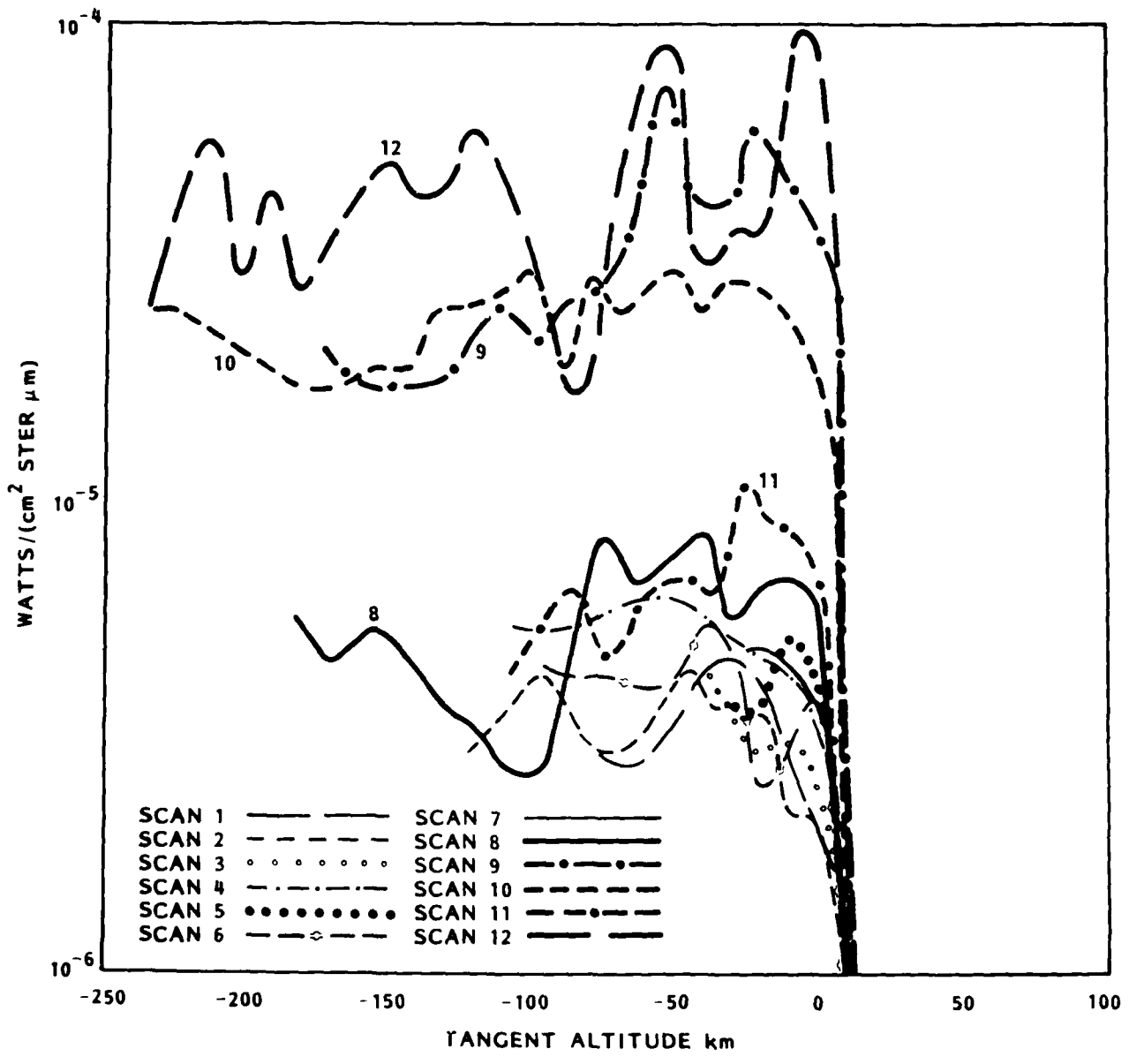


Figure 2-22 SPIRE spectral earthlimb radiance data in the 3.9 to 4.1 μm window region are plotted versus tangent altitude h on this figure. Note that scan 11 data for hard earth viewing (ie. for $h < 0$) more closely resemble data obtained in the night time scans 1 through 8 than data obtained on the obviously sunlit scans 9, 10 and 12.

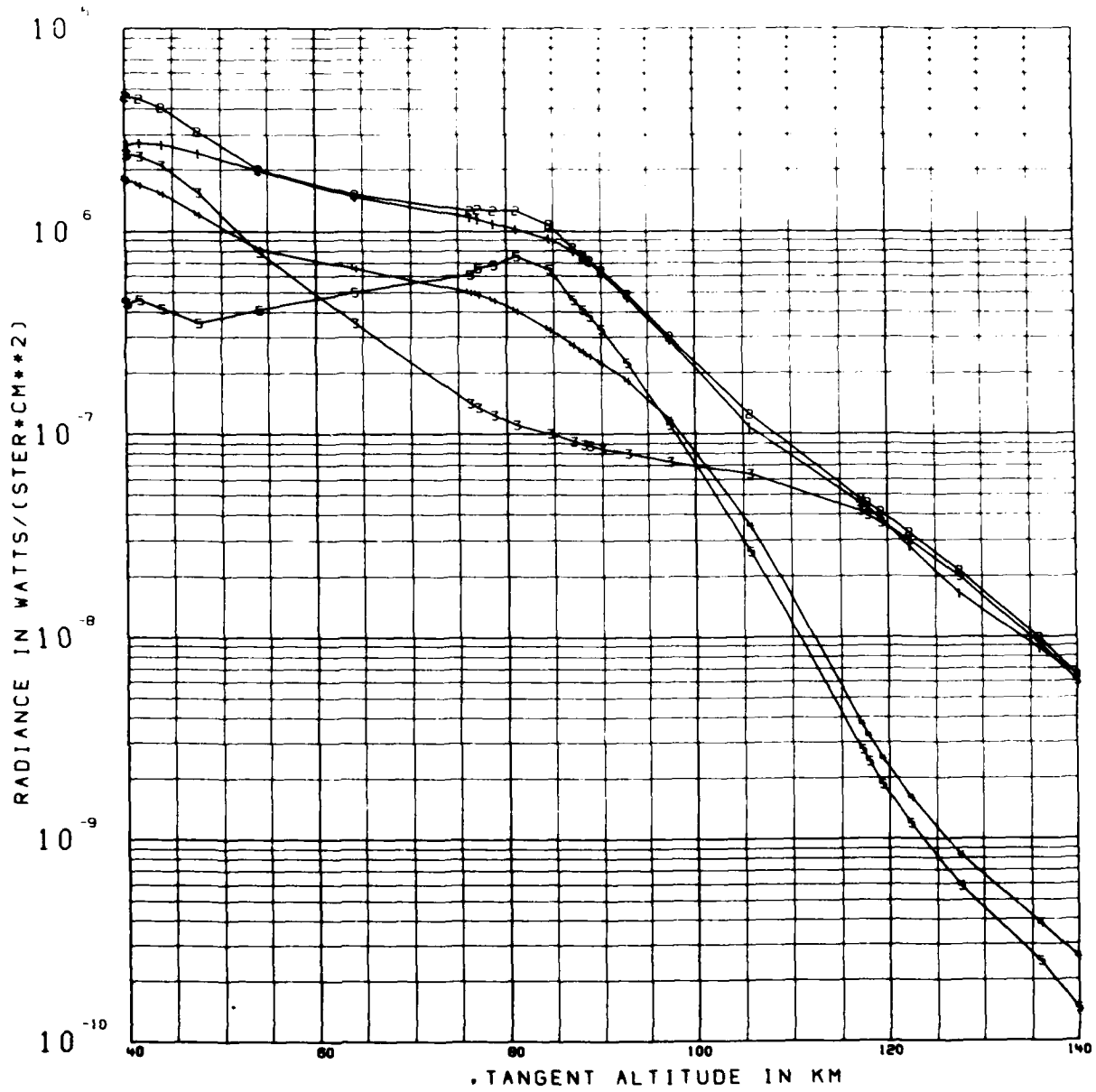


Figure 2-23 Same as Figure 2-11 except that the solar elevation angles utilized for the calculation are reduced by the assumption that the SPIRE scan pattern has been rotated 14 degrees further away from the sun than is currently accepted.

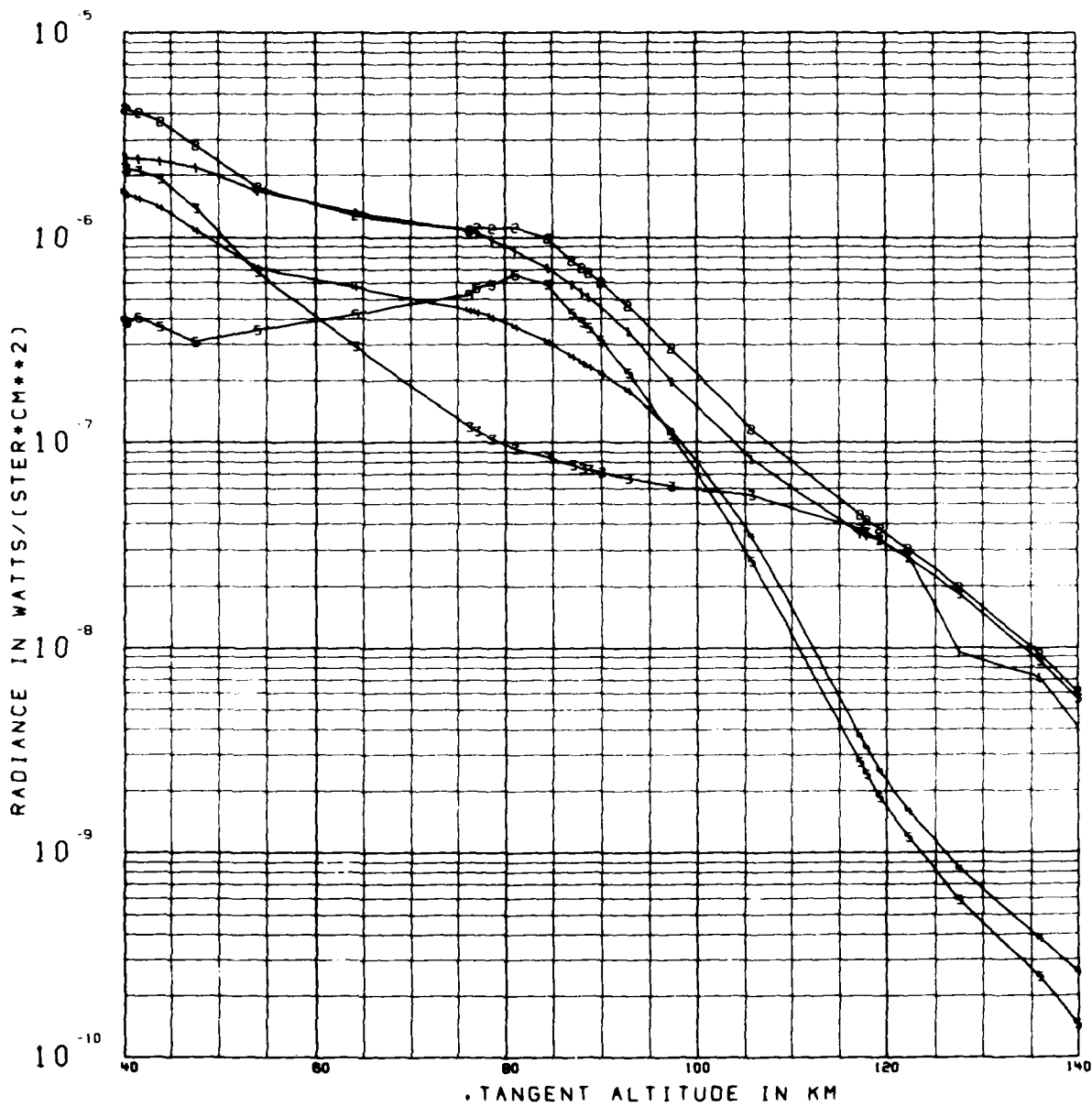


Figure 2-24 Same as Figure 2-12 except that the solar elevation angles utilized for the calculation are reduced by the assumption that the SPIRE scan pattern has been rotated 14 degrees further away from the sun than is currently accepted.

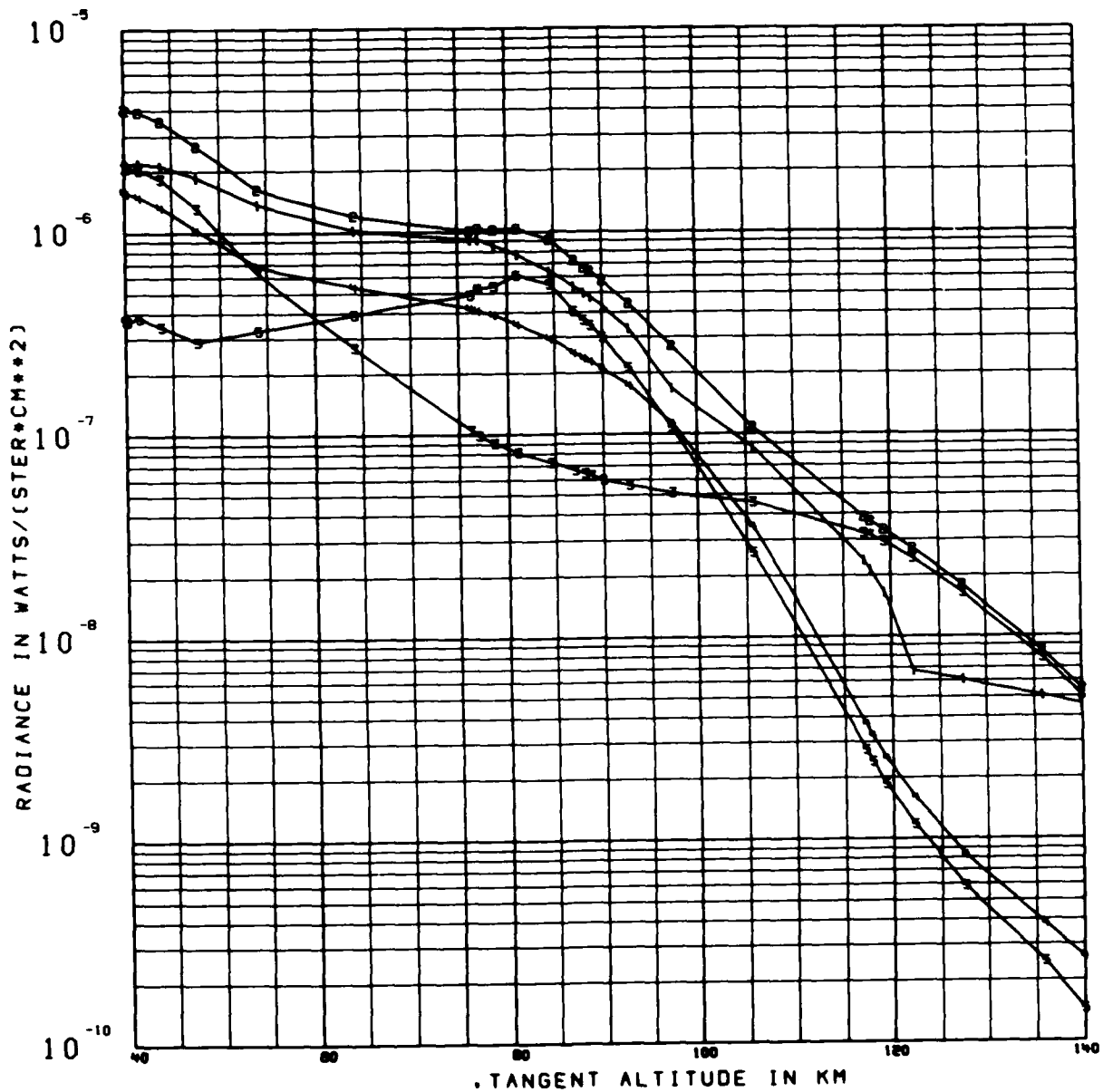


Figure 2-25 Same as Figure 2-13 except that the solar elevation angles utilized for the calculation are reduced by the assumption that the SPIRE scan pattern has been rotated 14 degrees further away from the sun than is currently accepted.

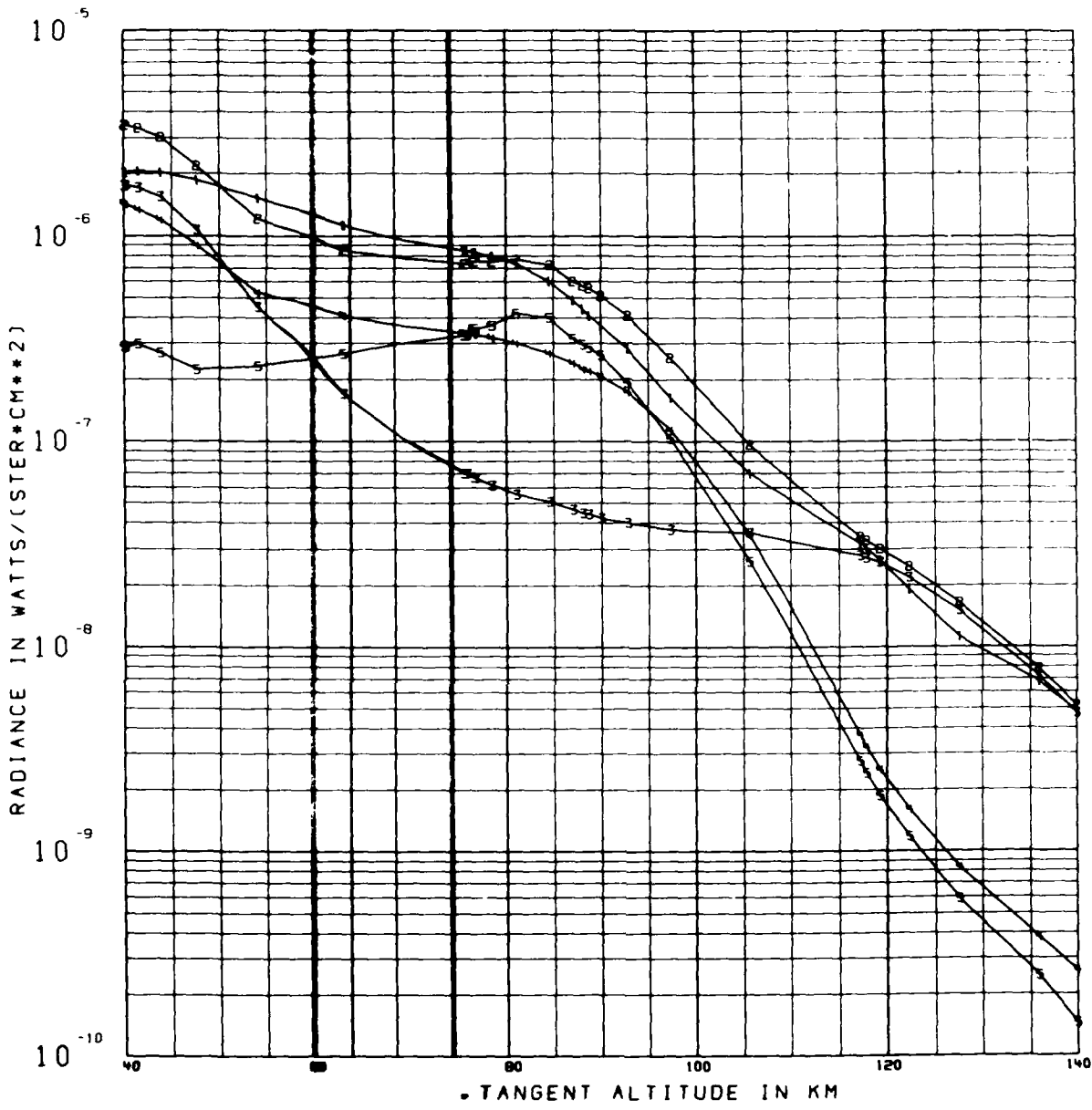


Figure 2-26 Same as Figure 2-14 except that the solar elevation angles utilized for the calculation are reduced by the assumption that the SPIRE scan pattern has been rotated 14 degrees further away from the sun than is currently accepted.

better than do the predictions generated on the basis of no rotation from the accepted scan azimuth (shown in Figs. 2-11 through 2-14 above).

Considering both the "nadir 4.0 μm window" data and the high altitude daytime 4.3 μm data, we do seem to have reason to suggest that there may be some residual uncertainty in the registration of the azimuth of the SPIRE scan patterns. We are reluctant to push this suggestion very hard though, since in neither case is the argument conclusive as much as it is suggestive. That is, in either case alternate possibilities that might explain the evidence that we have construed in these cases to suggest azimuthal misregistration can be invoked. For example, in section 2.3.3 we cite several mechanisms alternate to azimuthal misregistration which could contribute to the overprediction that is generally evident in Figs. 2-11 through 2-14. The latter predictions are based on the currently accepted azimuthal registration. Similarly, we have discussed in this section some of the effects that render the "nadir 4.0 μm window" data more suggestive than conclusive, that there could be some misregistration in the SPIRE scan pattern azimuth.

2.4 ANALYSIS OF THE NIGHT TIME SPIRE 4.3 μm DATA

2.4.1 Introduction

In this section we discuss a brief correlative analysis of the 2.7 and 4.3 μm data obtained in the eight night time SPIRE data scans and a more detailed quantitative analysis of a representative sample of the night time SPIRE 4.3 μm data, namely quantitative analysis of the night time scans 2 and 8. The scope of our effort limited us to quantitative analysis of just a portion of the data. Scans 8 and 2 are the extreme "south" and "north" scans respectively, thus we thought these scans might provide extremes of night time variability. Scan 1 was slightly further "north" than scan 2 but we did not choose to analyze this scan in detail since it was not complete, i.e., it did not extend up to high enough altitude. The data were processed as described in section 2.3.1 in an attempt to extract effects such as drift of the DC level in the data.

The comparison of our predictions for the night time 4.3 μm earthlimb against the data for scans 2 and 8 generally supports the position in our paper (Kumer et al., 1978) that night time CO_2 4.3 μm emission in the altitude region $> \sim 75$ km is dominated by collisional transfer of vibrational excitation from $\text{OH}(v > 0)$ to N_2 , followed by subsequent transfer to CO_2 and multiple scattering in the 4.3 μm bands. The correlative study of all eight scans did not conclusively support or refute this position.

We also find that additional mechanisms are required to achieve a better fit to the data. The requirement for these additional mechanisms becomes particularly noticeable above approximately 90 to 95 km. We looked quantitatively into the possibility of two mechanisms to explain the additional high altitude excitation, (1) the direct excitation by sunlight, and (2) an excitation related to the recombination of oxygen, i.e., a Chapman-like mechanism. Neither of these can account for the extra excitation mechanism that is required at high altitude. The major problem with the Chapman mechanism is that it requires an efficiency for producing N_2 vibrational excitation from the energy released by the exothermic reaction $\text{O} + \text{O} + \text{M} \rightarrow \text{O}_2 + \text{M}$ that is nearly 200 percent. We discuss results obtained and requirements on this Chapman-like mechanism for the extra source of CO_2 (v_3) excitation above 90 to ~ 95 km in detail in section 2.4.2.

We must caution that these findings should be considered as preliminary since we did not have the resources in the scope of the effort that we are reporting to produce a scientifically complete investigation. To do this would require us to quantitatively analyze all eight data scans that were obtained in night time conditions. Since the two mechanisms cited above could not explain the extra excitation above 90 to 95 km, it is required that we should consider a number of additional mechanisms. Some candidate mechanisms that need to be considered, but were not in the scope of the effort we are reporting on, would include precipitation, transport of CO_2 (v_3) by multiple scattering of sunlight from the adjacent sunlit region of the atmosphere, or a broader source of $\text{OH}(v)$ than we actually used, one that extends to higher altitudes than currently envisaged for production of $\text{OH}(v)$.

2.4.2 Comparison of Predictions and Data for Scans 2 and 8

On Figs. 2-27 through 2-29 we compare the data for scan 2 with our predictions. As above, the data are represented by curve 1, the predictions are curve 2, the 626 CO_2 001-000 band contribution to the predictions is curve 3, and the contribution of the weak bands is curve 4. We progressively add in mechanisms to achieve a better fit in going from Figs. 2-27 to 2-29. The mechanisms we consider for the night time case are given in Table 2-5. Note that absorption of sunlight is not included in Table 2-5. Since the hard earth shadow heights were less than 140 km for many of the "dark" scans we specifically investigated the possibility that absorption of sunlight could play a role in producing the extra source of excitation of CO_2 (ν_3) that is required at high altitude. We found that this was not an important factor since the large absorption along the long slant paths through the atmosphere renders the effective shadow height for absorption of sunlight by CO_2 to be approximately 80 to 110 km higher than the hard earth shadow height.

The non-airglow associated mechanisms, thermal collisions and absorption of 4.3 μm earthshine, are utilized to attempt to model the data on Fig. 2-27. These are mechanisms 1, 4, and 5 listed in Table 2-5. It can be seen that these mechanisms do not produce sufficient excitation to adequately model the data.

On Fig. 2-28 we add in the OH airglow related mechanism 2 in Table 2-5. This mechanism has been discussed by Kumer et al (1978) where it was shown that excitation transfer via mechanism 2 in Table 2-5 of about $0.12 \text{ ergs}/(\text{S-cm}^2)$ was required to achieve agreement with a set of quiet night time 4.3 μm zenith radiance data obtained 4-11-74 by AFGL and Utah State University personnel. To achieve the modeling agreement shown by Fig. 2-28 required transfer from $\text{OH}(V > 0)$ via mechanism 2 in Table 2-5 of $0.19 \text{ ergs}/(\text{S-cm}^2)$ in the half width altitude range 83 to 89 km. It can be seen that an additional source of excitation above 90 km is required to achieve a better fit to the data.

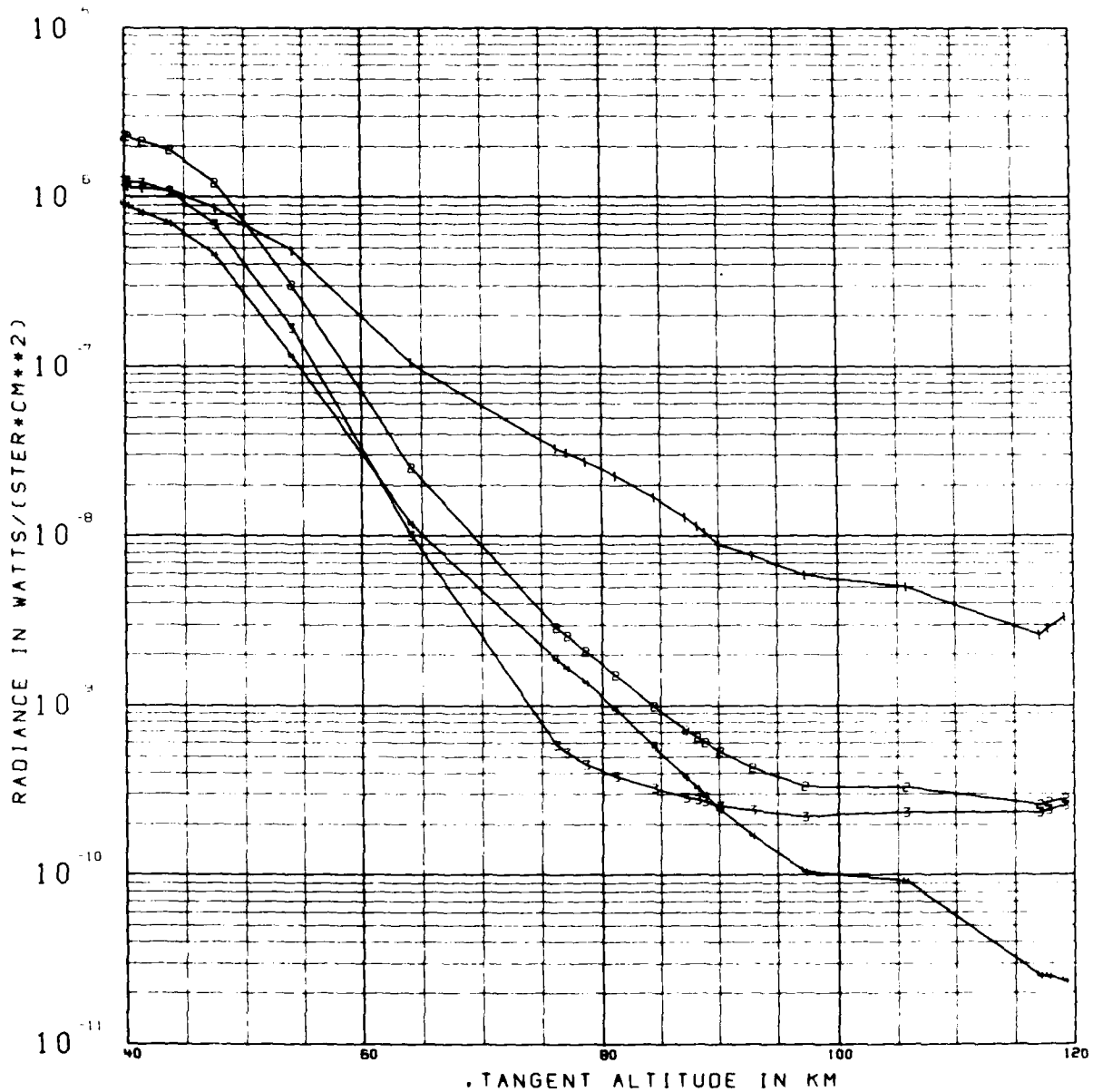


Figure 2-27 The $4.3\mu\text{m}$ data for dark scan 2 are given by curve 1. The predictions are labelled by curve 2, components due to the CO_2 626 001-000 band by curve 3 and due to the "weak" bands by curve 4. The non-airglow associated mechanisms 1, 4 and 5 in Table Figure 2-5 are used to calculate the predictions.

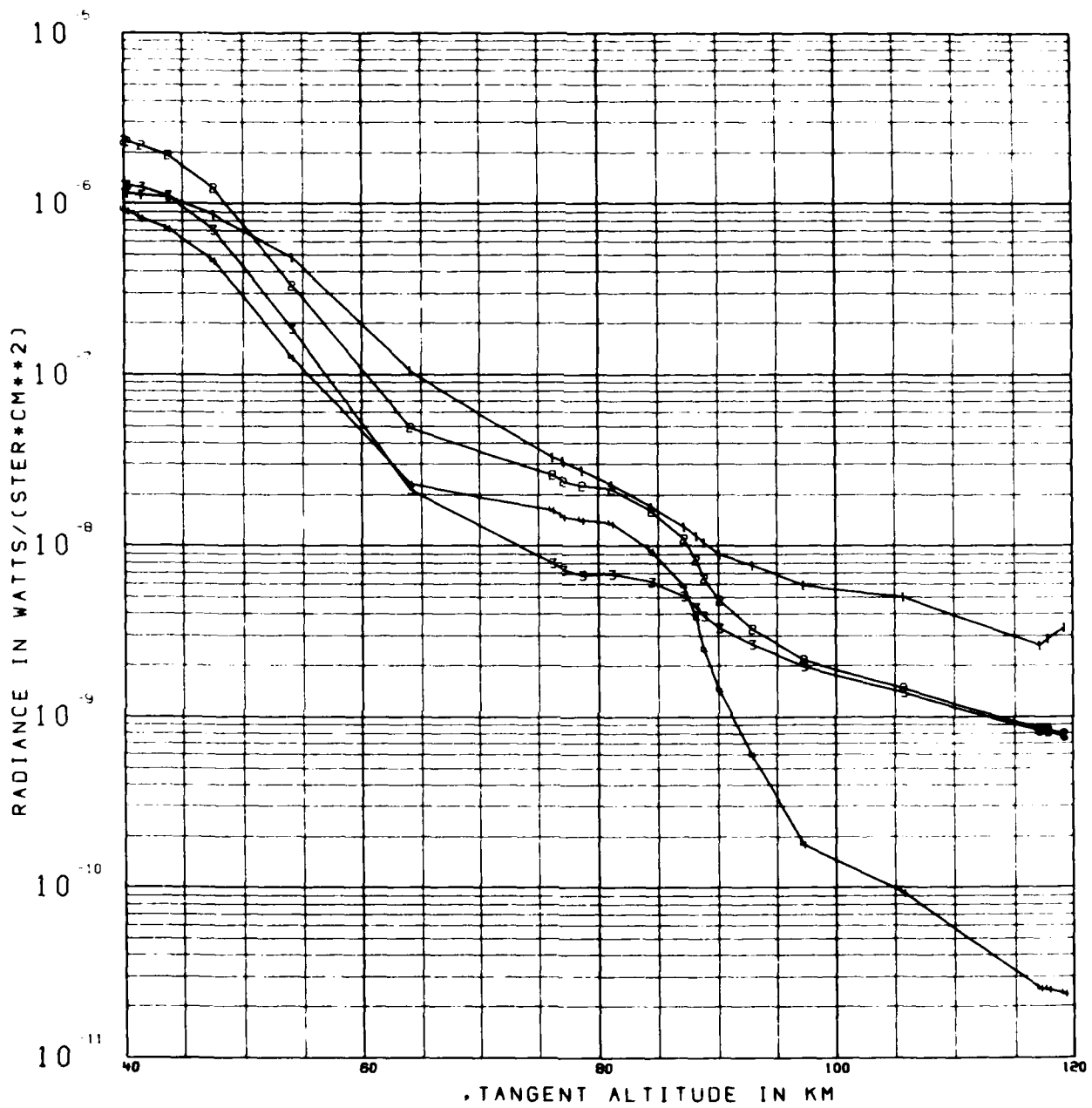


Figure 2-28 Same as Figure 2-27 except the OH airglow related mechanism 2 in Table Figure 2-5 is also included in generating the predictions.

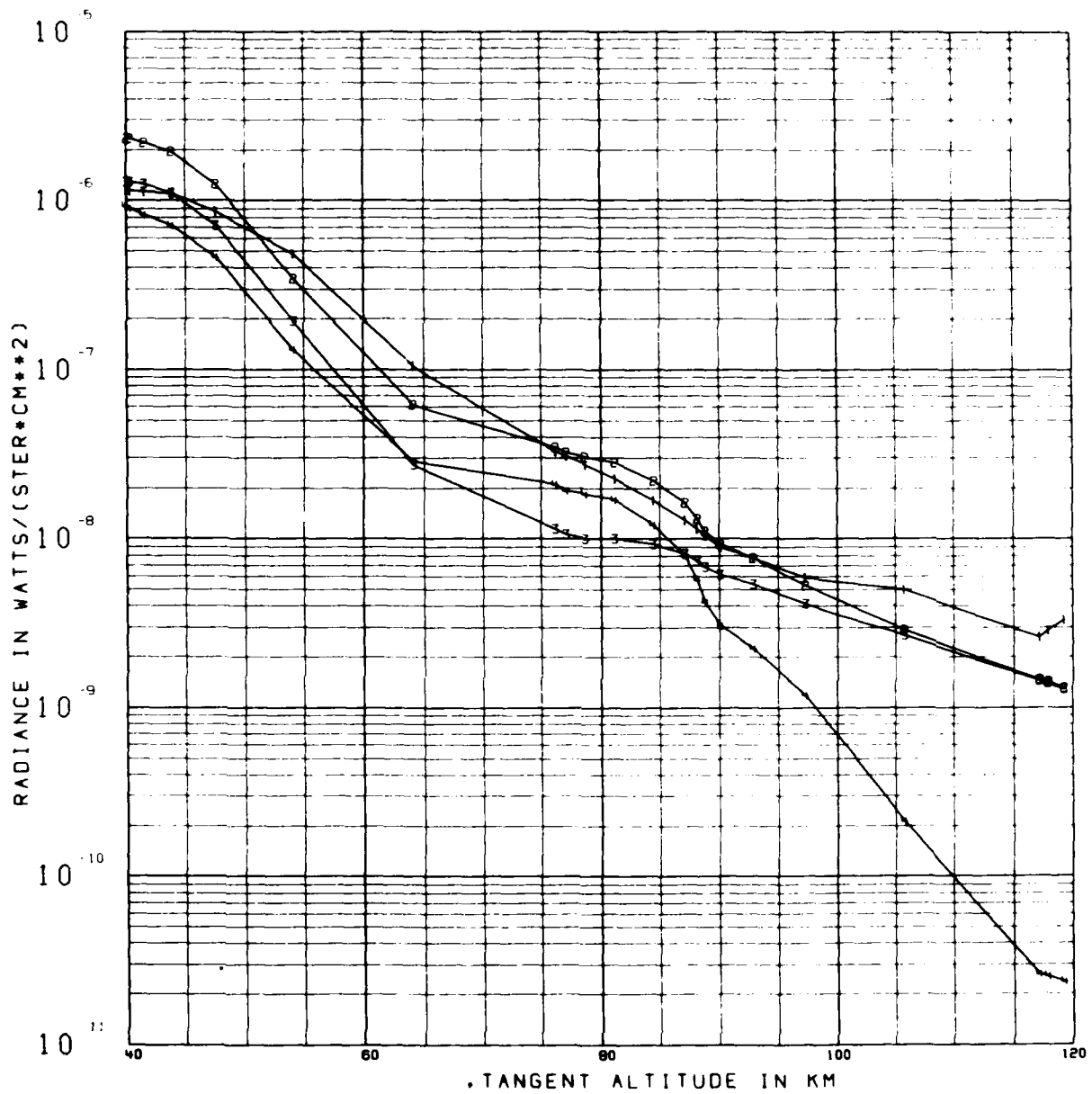


Figure 2-29 Same as Figure 2-28 except the "Chapman-like" airglow related mechanism 3 in Table Figure 2-5 is also included in generating the predictions.

The predictions we show on Fig. 2-29 include a second postulated airglow related mechanism. The "Chapman-like" mechanism is shown by item 3 in Table 2-5. The excitation E_x in units (vibrational quanta)/(S - cm³) due to this postulated mechanism is given as a function of altitude by

$$E_x = E_f [M] [O]^2$$

and the value $E_f = 1.1 \times 10^{-31} \text{ cm}^6/\text{S}$ is required to achieve the quality of fit shown on Fig. 2-29. Since the rate constant $k = 3 \times 10^{-33} \text{ cm}^6/\text{S}$ for the reaction



and since there are 5ev released by reaction (2.5), we are requiring that about 200 percent of the available energy finds its way into vibrational excitation of N₂. This appears to exceed the realm of credibility.

Table 2-5 MECHANISMS FOR NIGHT TIME EXCITATION OF CO₂ v₃ IN THE UPPER ATMOSPHERE

Item	Mechanism
1	Thermal collisions with atmosphere species other than N ₂ *
2	O ₃ +H→OH (V>0) +O ₂ OH (V>0) +N ₂ →OH (V-1) + N ₂ (V=1) N ₂ (V=1) +CO ₂ <=> N ₂ + CO ₂ (v ₃) CO ₂ (v ₃) <=> CO ₂ + hν (4.3μm)
3	O+O+M→O ₂ +M +energy
4	Thermal collisions with N ₂
5	Absorption of 4.3 μm earthshine by atmospheric CO ₂

* The mechanisms 1, 4 and 5 above have been discussed in detail by Kumer and James (1974), the mechanism 2 has been discussed in detail in the paper by Kumer et al. (1978), and the mechanism 3 is discussed in detail in the present report.

On Fig. 2-30 we show the comparison of our predictions with scan 8 data. Both the OH and the Chapman-like mechanism were utilized to provide the fit as shown. Again the transfer of $0.19 \text{ ergs}/(\text{S-cm}^2)$ from OH ($V > 0$) was used to achieve the fit to the scan 8 data that is shown in Fig. 2-30. In order to invoke the Chapman-like mechanism to achieve the quality of fit as shown required $E_f = \sim 3.4\text{E-}31 \text{ cm}^6/\text{S}$. This differs from the value required to fit the scan 2 data by a factor ~ 3 . This provides further evidence that the Chapman-like mechanism is not a good candidate for explaining the extra energy source for two reasons; (1) the requirement on E_f is inconsistent from scan 2 to scan 8, and (2) the value required for E_f for scan 8 is so large that it becomes inconceivable that the Chapman-like mechanism can supply the required energy.

2.4.3 Night Time Vibrational Temperatures

The atmospheric kinetic temperature and the vibrational temperatures of N_2 ($V = 1$) and CO_2 (001) which are calculated for scan 2 on the basis of the non-airglow associated mechanisms 1, 4, and 5 in Table 2-5 are shown plotted as a function of altitude on Fig. 2-31. Changes to the vibrational temperatures obtained by progressively adding in the mechanisms 2 and 3 in Table 2-5 are illustrated by Fig. 2-32 and 2-33.

2.4.4 Comparison of the SPIRE 2.7 and 4.3 μm Night Time Earthlimb Data

In order to determine if we could establish a correlation between the 2.7 and 4.3- μm night time earthlimb on a scan by scan basis, to support the hypothesis that the OH airglow mechanism is the dominant excitation mechanism for both these spectral regions in the night time earthlimb, we performed a brief examination of the 2.7 and 4.3 μm earthlimb in the altitude region of the OH airglow emission layer in the 2.5 to 3.1 μm and in the 4.1 to 4.5 μm bands for all eight "dark" scans. The spectral radiances in the 2.7 μm region varied between 1.3 and $2.3 \times 10^{-7} \text{ watts}/(\text{sq. cm-sr-um})$ and the spectral radiances in the 4.3 μm region varied from 6 to $10 \times 10^{-7} \text{ watts}/(\text{sq. cm-sr-um})$.

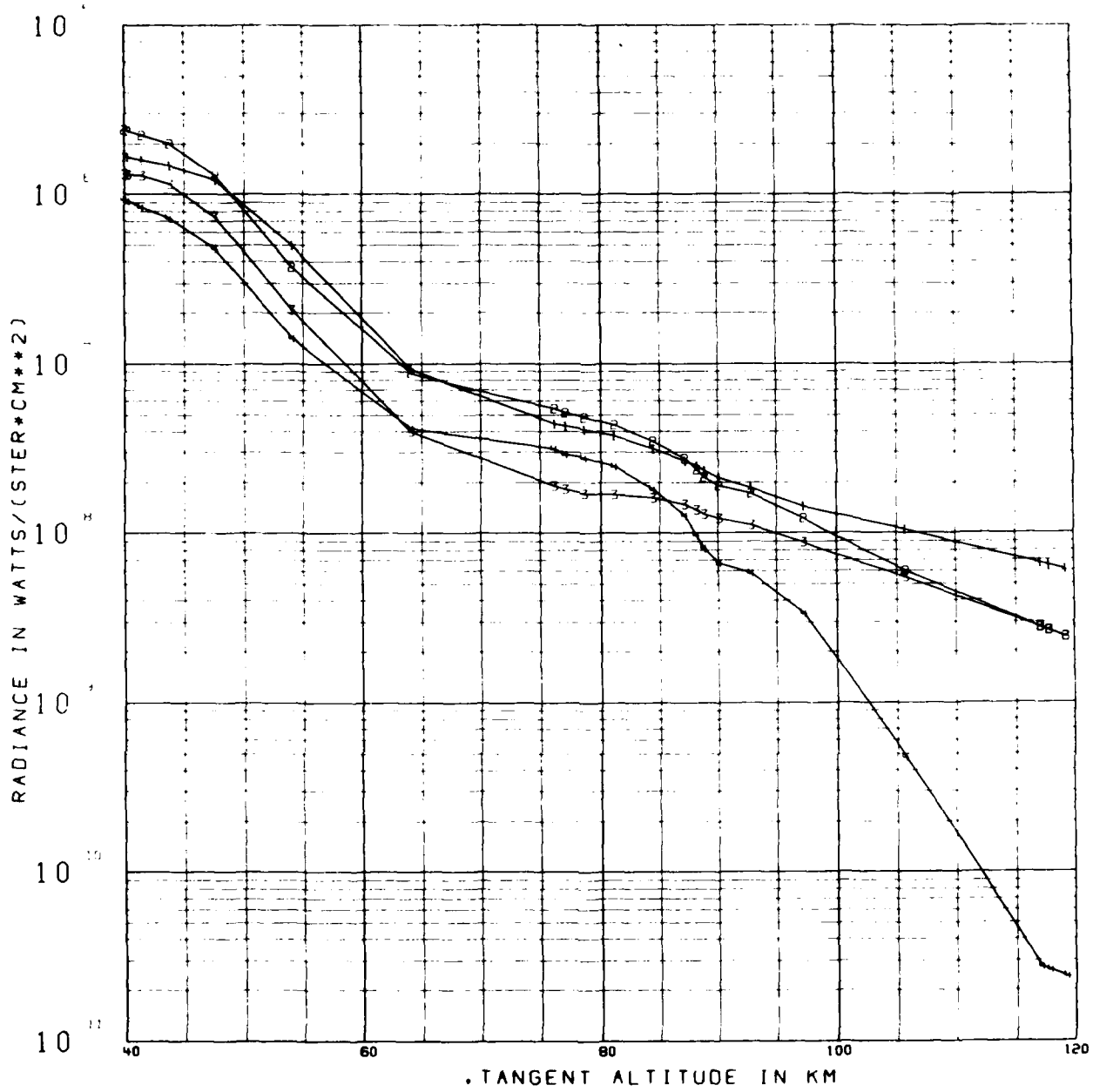


Figure 2-30 Same as Figure 2-29 except the data are from scan 9.

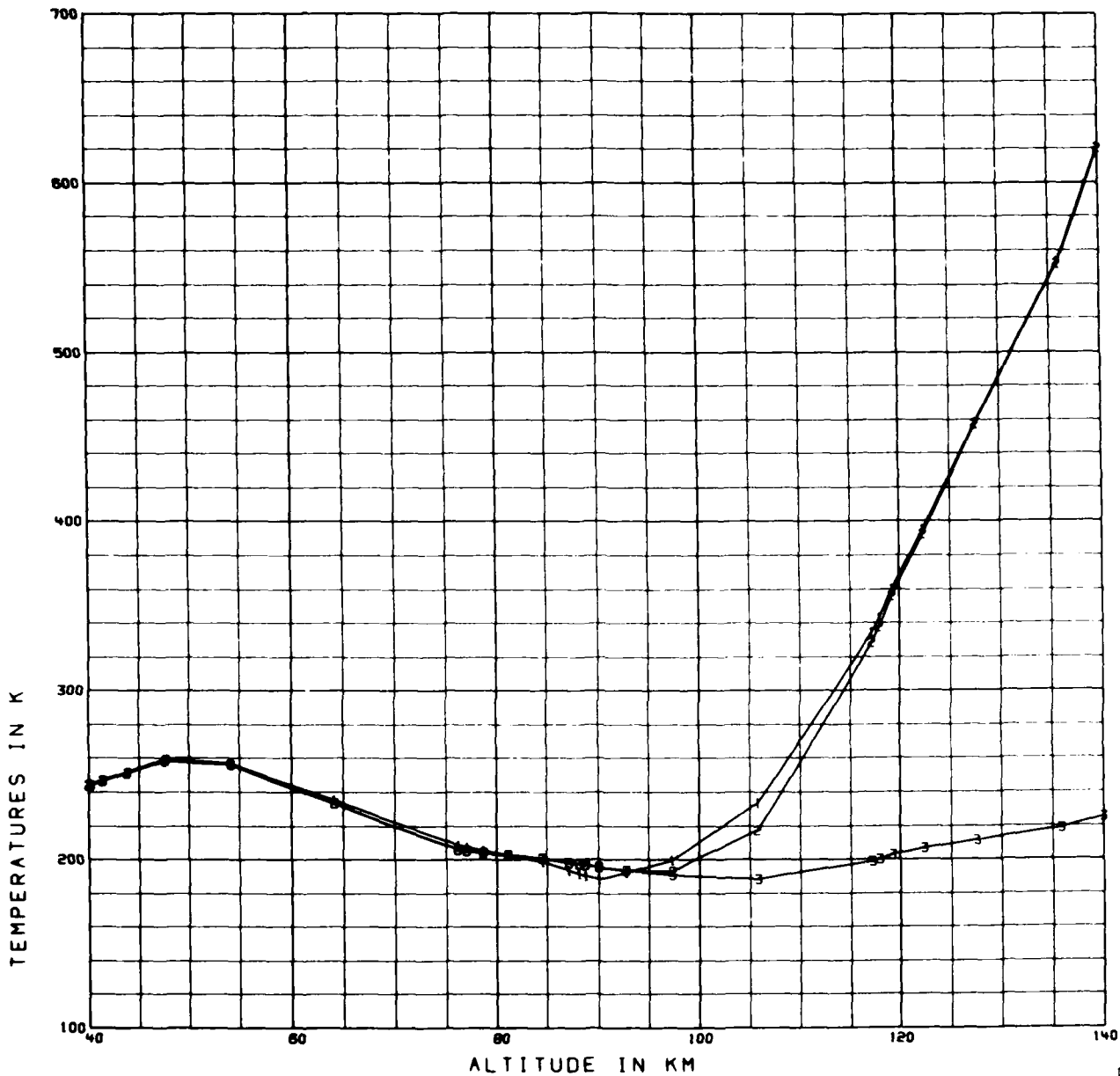


Figure 2-31 Atmospheric kinetic temperature (curve 1), N_2 and $CO_2(001)$ vibrational temperatures (curves 2 and 3 respectively) are shown here. Mechanisms are those utilized to generate the predictions for scan 2 that are shown on Figure 2-27.

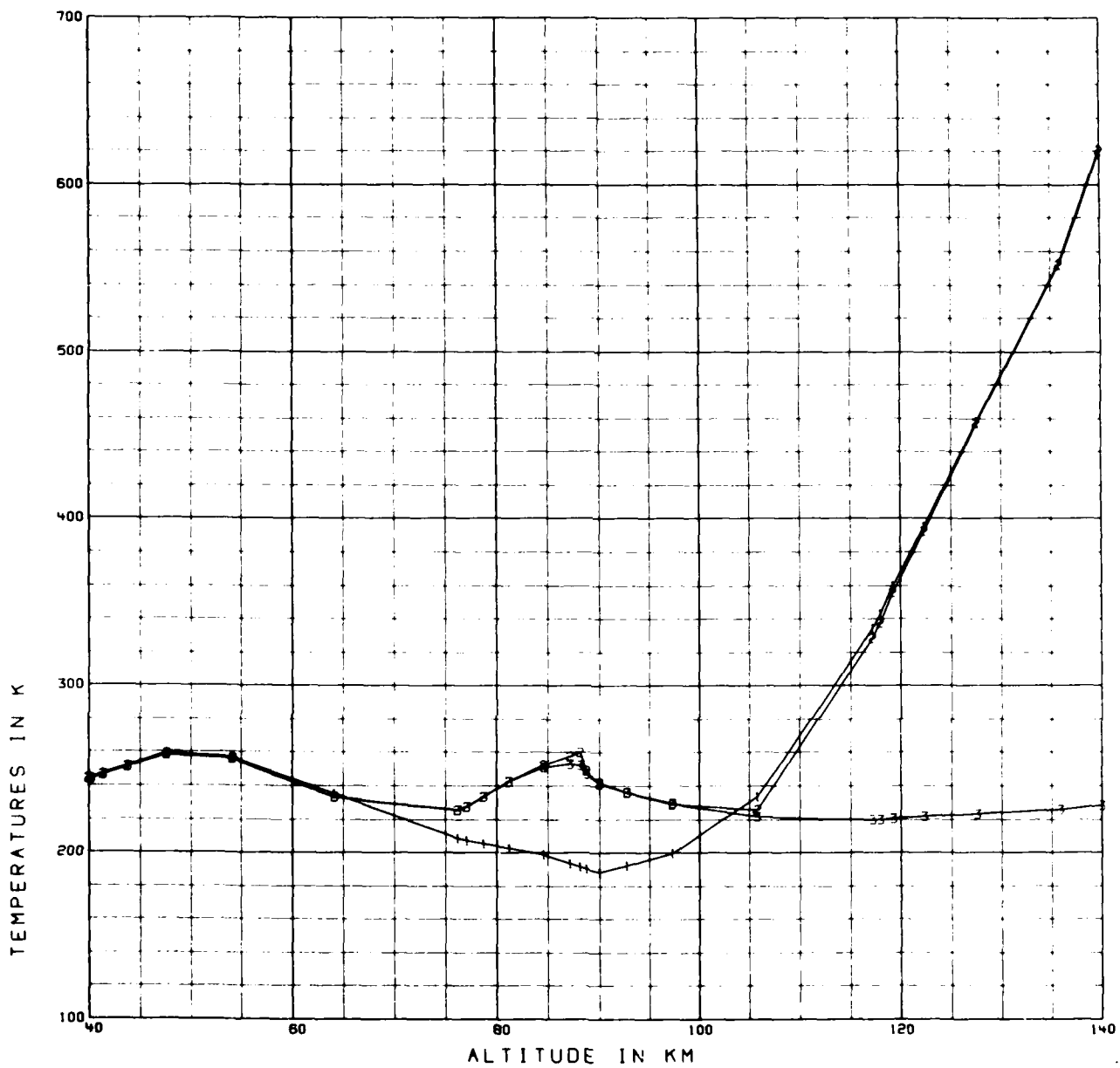


Figure 2-32 Atmospheric kinetic temperature (curve 1), N_2 and $CO_2(001)$ vibrational temperatures (curves 2 and 3 respectively) are shown here. Mechanisms are those utilized to generate the predictions for scan 2 that are shown on Figure 2-28.

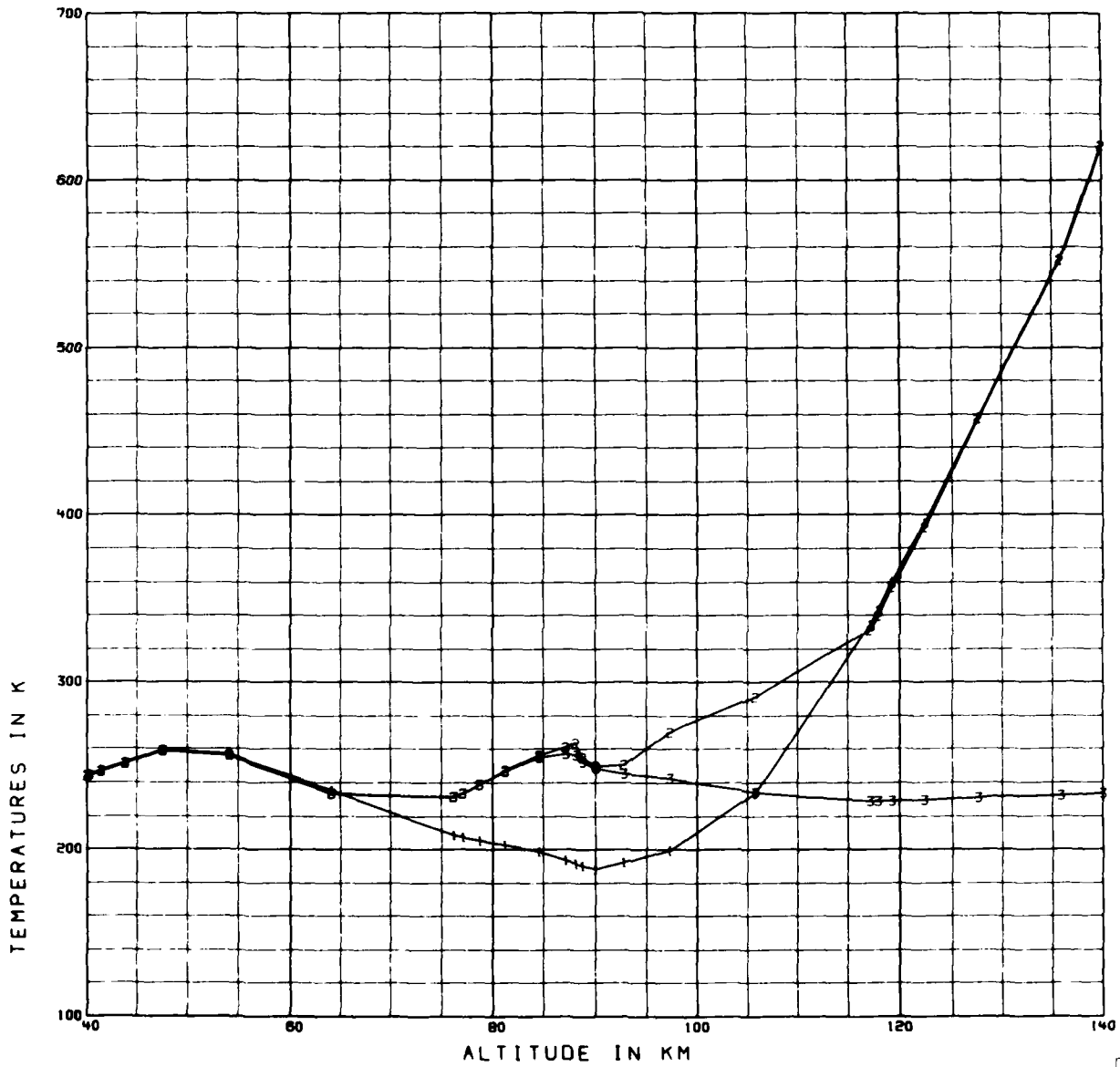


Figure 2-33 Atmospheric kinetic temperature (curve 1), N₂ and CO₂(001) vibrational temperatures (curves 2 and 3 respectively) are shown here. Mechanisms are those utilized to generate the predictions for scan 2 that are shown on Figure 2-29.

First, there appeared to be only a small correlation, if any at all, on going from one scan to the next in either of the wavelength regions. The noise and the DC drift in the baseline of the spectral data could have contributed to difficulty in establishing any readily apparent "one scan to the next correlation" in a given band. Also the altitude resolution is approximately equal to the half width of the OH emission layer and this could also have introduced some problems in trying to identify any apparent trend in the data on going from "one scan to the next".

Secondly, we did not find any readily identifiable correlation between the 2.7 and 4.3 μm data on a scan by scan comparison basis. However, correlation on a scan by scan basis in the 2.7 and 4.3 μm data is difficult to identify for the same reasons given above for the difficulties faced in identifying any correlation or trend within a given band on going from one scan to the next. Also, the multiple scattering of photons by CO_2 would tend to smooth spatial structure that may be present in the OH airglow source. Since the relaxation time constant for CO_2 emission is 6 to 8 minutes in this altitude region, this too would tend to smooth temporal structure in the OH airglow source.

We conclude that the comparison study between the 2.7 and the 4.3 μm night time earthlimb did not show any readily apparent correlation on a scan by scan basis, but for reasons given above this should not be taken to mean that the OH mechanism is not the dominant mechanism for producing CO_2 (ν_3) in the altitude region 80 to 90 km.

2.5 ANALYSIS OF DAYTIME CO_2 CONTRIBUTION TO THE 2.7 μm EARTHLIMB

2.5.1 Estimated CO_2 Contribution to the Sunlit 2.7 μm Earthlimb

In our January 1981 presentation at the AIAA meeting held in St. Louis (Kumer, 1981) we showed that absorption of sunlight at 2.7 μm by the 626 CO_2 species followed by reemission at 2.7 μm could not produce sufficient radiance to explain the 2.7 μm daytime SPIRE data. This stimulated work by Sharma to investigate the possibility that absorption of sunlight by CO_2 at ~ 2.0 and

1.6 μm followed by fluorescence at 2.7 μm could be an important contributor to the SPIRE sunlight 2.7 μm earthlimb. Likewise Degges investigated the prospect that resonance scattering of sunlight at 2.7 μm by H_2O might also be an important contributor.

In the event Sharma and Degges showed that both of these mechanisms were indeed very important in the formation of the 2.7 μm earthlimb. Additionally we looked into the prospect that absorption and reemission of 2.7 μm sunlight by the minor isotopic CO_2 species 636, 628, and 627 could also play a significant role in the formation of the 2.7 μm sunlit earthlimb, and found indeed that it did. By considering the contributions of all these mechanisms Sharma and Nadile (1981) showed that the 2.7 μm sunlit SPIRE data could be reasonably well understood.

On Fig. 2-34 we show our estimated prediction for the contribution to the 2.7 μm earthlimb that is due to absorption and reemission of 2.7 μm sunlight by CO_2 . Curve 2 is the component that is due to absorption and reemission of 2.7 μm sunlight by the major isotopic species 626 CO_2 . The sum of all these components is curve 1 on Fig. 2-34. The contribution from absorption and subsequent reemission of 2.7 μm sunlight by the 636, 628 and 627 isotopic species of CO_2 is given by curve 3.

The predictions that we show for curves 2 and 3 are a factor 2 smaller than we had reported previously in our March through April 1981 progress report. Since the time of that work we have found and corrected a very troublesome bug in our program that had introduced an overprediction by a factor of 2 in our curves 2 and 3 on Fig. 2-34. We found and corrected this error just recently in the process of analyzing the daytime 4.3 μm earthlimb data as is described above in section 2.3. Our program had originally been functioning accurately but we introduced the bug when we made an attempt to deal with the effect of the reaction

$$\begin{Bmatrix} 10^{\circ}1 \\ 02^{\circ}1 \end{Bmatrix} + M \begin{matrix} \rightarrow \\ \leftarrow \end{matrix} O_2^2 1 + M. \quad (2.6)$$

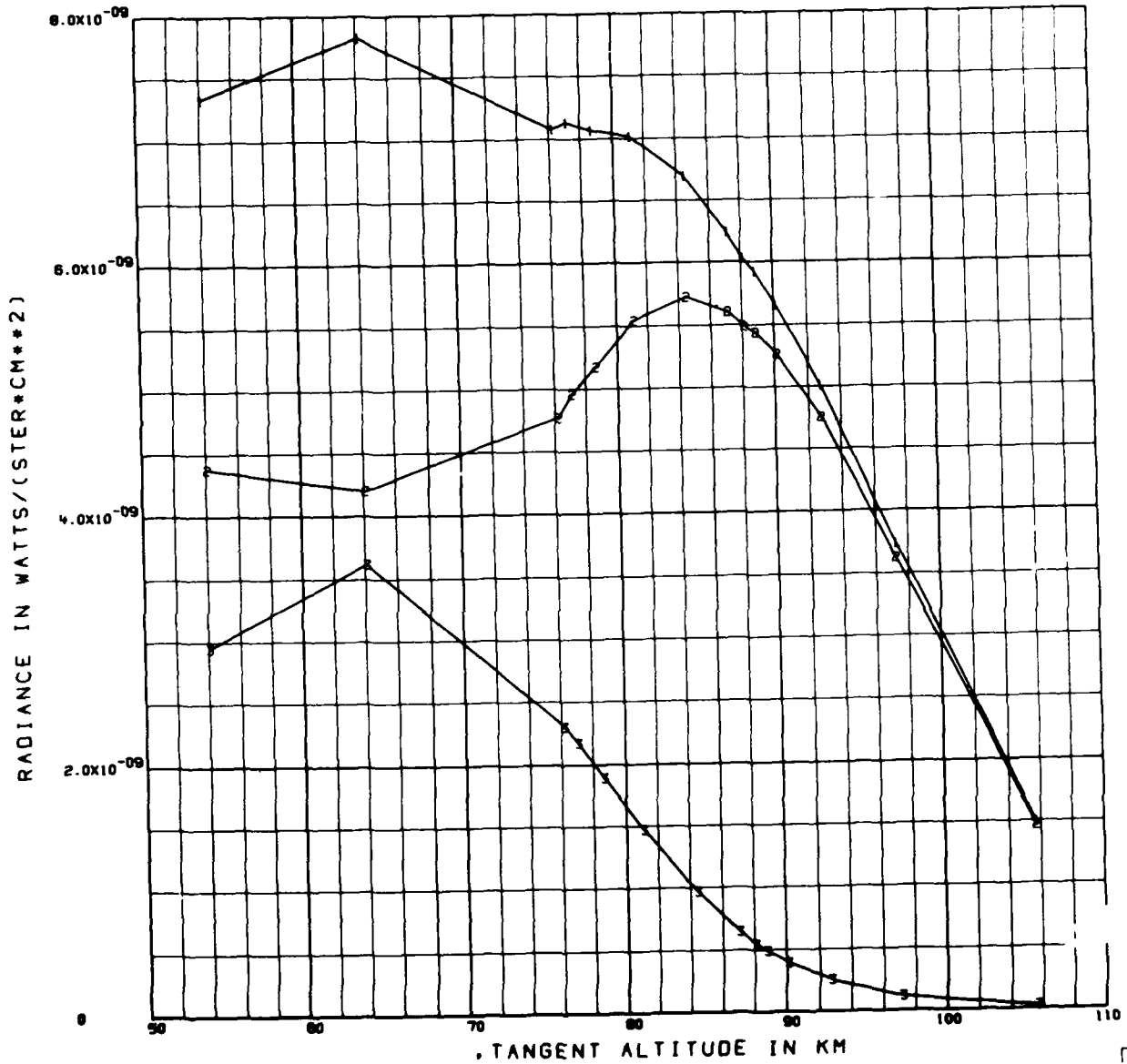
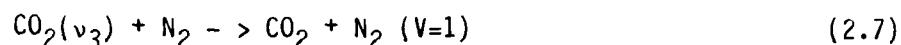


Figure 2-34 Predictions for the CO₂ contribution (curve 1) to the sunlit 2.7 μm earthlimb that results from the absorption of 2.7 μm sunlight by CO₂, followed by subsequent re-emission, are shown here. Curve 2 is the component due to the 626 CO₂ species and curve 3 is the component due to the minor isotopic species of CO₂.

We were concerned with this reaction because the states with $v = 2$ are forbidden to radiate in the 2.7 μm band, thus the effect of this reaction would be to reduce the predictions in Fig. 2-34 by another factor 2 if the rate constant for reaction 2.6 is as large as, or comparable to, the rate constant for the reaction



Since our calculations on Fig. 2-34 represent an underprediction, one might infer that the rate constant for the reaction 2.6 is not as large as that for the reaction 2.7. We had hoped to measure the rate constant for reaction 2.6 in our complimentary laboratory experiment but circumstances prevented this. Details are provided in section 3.0 below which deals with our complimentary laboratory effort. Future effort should be directed at development of an accurate method to account for reaction 2.6 quantitatively in the calculation of its effects on the 2.7 μm earthlimb, and to establish realistic estimates of the magnitude of the rate constant, i.e., it is not of much interest unless it is comparable to or larger than for reaction 2.7.

2.5.2 Preliminary Efforts to Spectrally Model the 2.7 μm Earthlimb

The 2.7 μm sunlit SPIRE data lend themselves to spectral analysis which may possibly yield fairly precisely the contribution from each of the candidate sources. To this end we began a preliminary effort to adapt a very general and comprehensive software package that has been developed partially under the Lockheed Independent Research Program and partially under the ongoing contract NAS5-26173 for the purpose of calculation of spectral limb radiance and for the decomposition of spectral earthlimb data into the components that result from various species and/or mechanisms. The package includes capability for relatively rapid calculation at spectral resolution $\Delta\nu \lesssim \nu_D$ where ν_D is the Doppler width of the radiating molecular species. Arbitrary slit functions may be utilized. The calculations may be performed for any of 20 molecular species compiled on the latest version of the AFGL McClatchey/Rothman tape. On Fig. 2-35 we show a sample calculation of

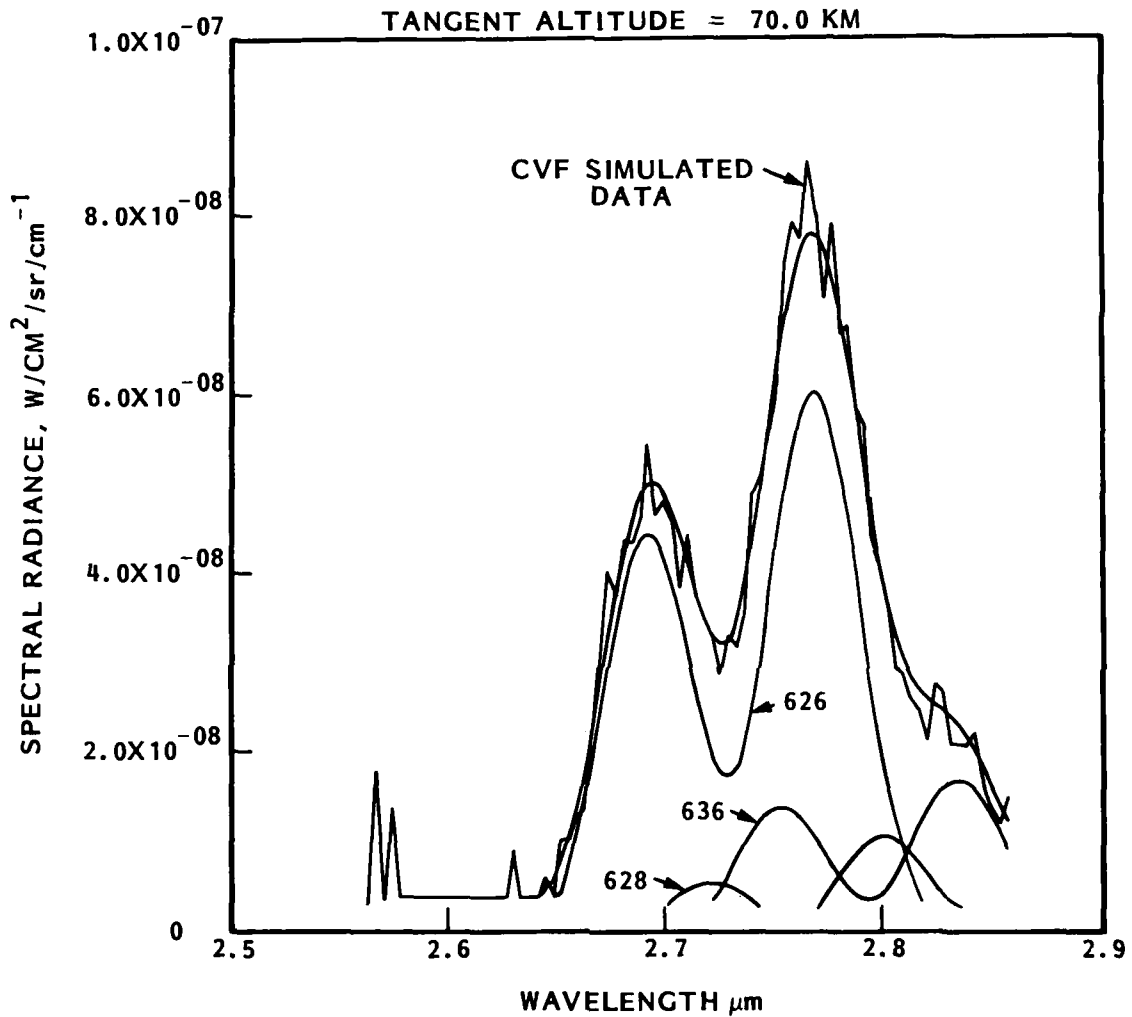


Figure 2-35 The contribution to the sunlit $2.7\mu\text{m}$ spectral earthlimb that is due to absorption and re-emission of sunlight by CO_2 is shown here. The simulated data are calculated for resolution and sensitivity that approximates SPIRE performance.

earthlimb spectral radiance at 70 km tangent altitude due to absorption of sunlight at 2.7 μm by CO_2 followed by reemission at 2.7 μm . The calculation was performed for conditions of solar illumination approximately applicable to sunlit scan 9 of the SPIRE experiment.

A facility of this software is that the contribution to spectral radiance due to any bands of interest to the programmer may be calculated and displayed independently. The software also has facility to use these components as base functions to be fit to actual data, thereby providing the quantitative means to decompose the SPIRE data into the components that result from various species and/or mechanisms. The software may also be employed in an inversion mode to determine either the number density of the emitting species, or, in some cases, to determine the vibrational temperature of the upper levels of the transition. The projected capability of this improved software package which is being developed under the programs cited above differs from our previous capability in that (1) spectral earthlimb radiance is calculated, rather than molecular band integrated earthlimb radiance, (2) the capability may be applied to all 20 species on the latest Rothman update of the McClatchey tape, (3) the new capability does not utilize physical models to calculate vibrational temperature; instead, the vibrational temperatures must be (a) input from an independent calculation such as can be provided in certain cases by our previous software capability, or (b) derived by an inversion process directly from earthlimb data such as the SPIRE data, or data that are to be obtained in the ELIAS, CIRRIIS, and SPIRIT experiments.

A logical development for the improved software package would be the detailed adaptation to the analysis of DNA/AFGL earthlimb problems that require this type of detailed spectral earthlimb modeling capability. This would include further detailed application against the SPIRE data, to glean the added information that is contained in the spectral signature of the SPIRE data. Such an effort need not be limited to the 2.7 μm region but in fact would be useful throughout the 1.4 to 16.5 μm spectral region. The improved software may also be used for analysis of data to be obtained in upcoming earthlimb

experiments such as SPIRIT and CIRRIS that are to employ very high spectral resolution.

2.6 HORIZONTAL STRUCTURE CONSIDERATIONS

To this point the discussion in section 2 has been concentrated on the analysis of the SPIRE data. In this section we digress from this theme, to utilize the SPIRE data at 15 μm to assist in constructing a reasonably realistic scenario for the occurrence of horizontal structure in earthlimb radiance for "long period" gravity waves (approximately 30 min or more).

There are cases in the literature (Noxon, 1978; or Faire and Murphy, 1972 are a small cross section of these) which suggest that gravity waves with atmospheric temperature perturbations of the order 40°K are not uncommon in the mesopause region. Also, there is evidence that suggests that horizontal wavelengths may be comparable with length scales of interest to the community. For example, Peterson (1979) discusses a bright structured visual OH airglow event suggestive of gravity waves with 16 km horizontal wavelengths which occurred on 4 and 5 April 1978. On the other hand, gravity waves ducted through the mesopause region may have horizontal wavelengths of hundreds of km.

A plausible approximation for a gravity wave perturbation to the model atmosphere (shown on Fig. 2-2 and 2-3 above) that we used for modeling the SPIRE data, as is discussed in section 2.2, is given by equations (2.8) and (2.9) below.

$$T = T_0(z) \left\{ 1 + A(z) \sin [k_z(z - 80 \text{ km}) + k_x X_0 + \psi] \right\} \quad (2.8)$$

$$n_i = n_{0i}(z) \left\{ 1 - A(z) \sin [k_z(z - 80 \text{ km}) + k_x X_0 + \psi] \right\} \quad (2.9)$$

Here T_0 and n_{0i} are the temperature and number densities of the unperturbed atmosphere.

For this sample case we use $k_x = 2\pi/140$ km, $k_z = 2\pi/20$ km, $\omega = 3.06 \times 10^{-3} \text{ s}^{-1}$, $c^2 = 0.08 \text{ (km/sec)}^2$, $g = 0.0095 \text{ km/s}^2$, $H = 6$ km and $\gamma = 7/5$ and $\omega_g^2 = (\gamma - 1)g^2/c^2 = 4.5 \times 10^{-4} \text{ s}^{-2}$ so that (from Hines Equations (33) through (36)) we get

$$\omega = \omega_g(k_x/k_z) = (2.12 \times 10^{-2}) (20/140) = 3.03 \times 10^{-3} \text{ s}^{-1}$$

Thus the period is 35 min, considerably slower than the Brunt frequency. For this case it can be shown that the approximate formulation of Hines (1960) can be used to show that the relative phase and amplitudes of the fractional perturbations in temperature and number density are as shown in Eqs. 2.8 and 2.9 above.

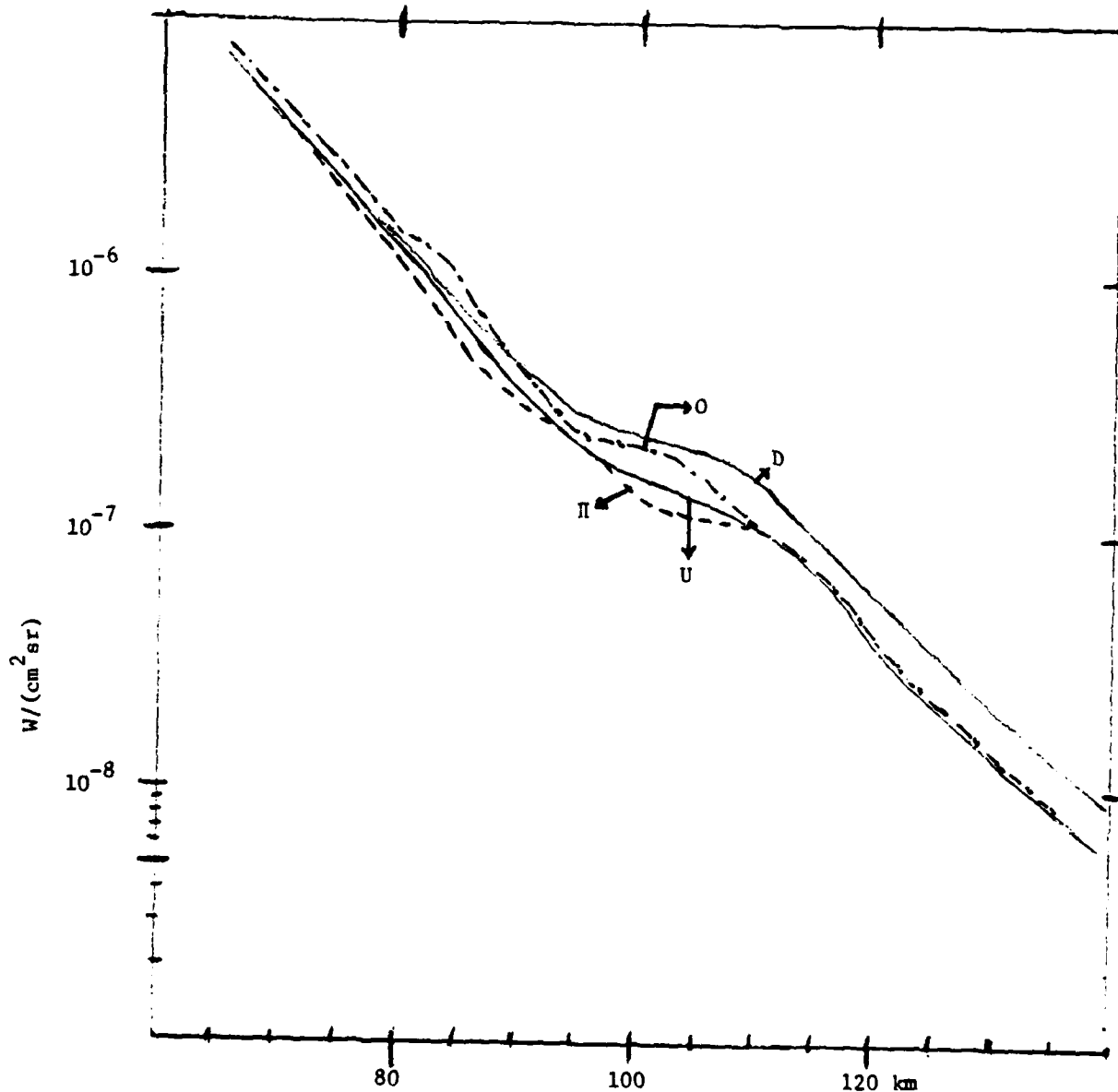
The fractional amplitude $A(z)$ of the perturbation is selected so that the temperature perturbation is ~ 40 deg at ~ 95 km. The specific altitude dependence of the fractional perturbation is given by:

$$A = 0.056 \exp [(z - 80)/2H]$$

for $z \leq 100$ km where z is altitude in km and $H = 6$ km. But for $z > 100$ km we introduce an empirical damping factor, so in this case

$$A = 0.056 \exp [(z - 80)/2H] \exp [(100 - z)/H].$$

To illustrate the possible infrared horizontal structure effect of a plausible approximation for a gravity wave perturbation to the model atmosphere (shown on Fig. 2-2 and 2-3) that we used for modeling the SPIRE data as is discussed in section 2.2, we show earthlimb radiance profiles due to CO_2 010 \rightarrow 000 emission in the 14 to 16 μm band on Fig. 2-36. Curve D is representative of the SPIRE data as shown on Fig. 2-1. Curve U is calculated via our most recent techniques as described above in section 2.2. Curve U is identical therefore to our predictions for the 15 μm earthlimb that are compared with the SPIRE 15 μm data on Fig. 2-6. It is calculated for the case of the unperturbed model atmosphere we have used for analysis of the SPIRE data that



2-36 Earth limb radiance in the 14 to 16 μm region for various cases as explained in the text are shown here. Curve D is representative of the SPIRE data. Curve U is a calculation based on the unperturbed atmospheric model (figures 2-2 and 2-3 above) that we have utilized in our SPIRE data analysis effort. Curves O and II are calculations based on gravity wave perturbations of the SPIRE data analysis model atmosphere that differ by Π in phase.

is illustrated by Fig. 2-2 and 2-3. Curves 0 and π apply for calculations that are performed with the atmosphere perturbed by a gravity wave as given by Eqs. (2.8) and (2.9) above for the phase angle $\psi = 0$ and π respectively.

Note that this example assumes plane gravity waves that are propagating in a direction that is perpendicular to an earth limb sensor line of sight (LOS), hence there is no gravity wave induced horizontal variation along the line of sight for this example. The gravity wave model that we have utilized is a simple variation of the isothermal Hines (1960) model and is useful for this illustration. However, more realistic calculations of the gravity wave perturbation of temperature and density in a real atmosphere are necessary to assess the effect of gravity waves more reliably than we have done here. This would require utilization of the latest results of Tuan and coworkers (Private Communication, Tuan, 1982).

2.7 IMPROVEMENTS SUGGESTED IN THE CURRENT HIGH ALTITUDE INFRARED RADIANCE MODEL

The SPIRE experiment and subsequent analysis provides a vehicle to verify and upgrade the AFGL High Altitude Radiance Model. This is an extremely useful thing to do since experience has shown that derivatives of the High Altitude Radiance Model, such as the OSC Code earthlimb model, are widely utilized in industry for evaluating sensor performance in sensor simulation studies. Too frequently the codes are applied by personnel with little knowledge of the applicability of the code to their particular problem, and not much of an idea as to when the code may not be applicable to their particular problem. Since this kind of utilization is sometimes practiced (certainly not the recommended practice by any means) it is necessary that the possible shortcomings of the model be explicitly spelled out so that misuse of the model is minimized, and that the model be kept up to date to the extent that the availability of data, such as the SPIRE data, and the analysis thereof permits.

In this discussion we address our remarks to the version of the Current High Altitude Radiance Model (CHARM) that is described by T.C. Degges in the report of Humphrey et al. (1981). Major ingredients of the CHARM include the (1) physical radiative transfer model, (2) non-LTE emission mechanisms, (3) the identification of the spectral bands of a given radiating specie that must be included in CHARM in order to perform adequate calculations, and (4) the temperature and composition of the input model atmosphere. Our discussion will address items (1) through (3).

Assumptions that go into the physical radiative transfer model that are used in CHARM are listed on page 12 of the report by Humphrey et al. (1981). The analysis of the 14 to 16- μm radiance that we report in section 2.2 above indicates that utilization of the assumption (6) "temperature variations at different altitudes do not affect the radiative transfer" in the CHARM does indeed introduce serious error in the altitude region above 95 km. In section 2.2 we have shown that the inclusion of band and line shape variation versus altitude, which results directly from "temperature variations at different altitudes," is one of the major effects which must be accounted for to improve on pre-SPIRE modeling of the 15- μm SPIRE data is achieved.

We also believe that the CHARM could be improved by utilizing line strengths that are properly weighted across the band as we described above in section 2.2, rather than by use of the current CHARM assumption (4) "line strengths are used as if each line were at the band center, neglecting wavelength variation across the band." The method we use to account for variation of line strength across the band has been discussed by Kumer and James (1974) and is also discussed in section 2.2 above. We believe this method could be included into CHARM and would result in an improved version of CHARM that would suffer little or no increased complexity and run time.

The analysis of SPIRE data we report here has also given some insight as to additional non-LTE mechanisms that are required to improve the CHARM. Inclusion of the faster vtr rate constant for quenching of CO_2 (010) by atomic oxygen at mesospheric temperatures is required to better model the

15- μm earthlimb. This was the second effect that we found in section 2.2 above to be very important to achieve an adequate model of the 15- μm SPIRE data. The inclusion of the $\text{O}(^1\text{D})$ mechanism is required to achieve a better model for the daytime 4.3- μm earthlimb. For the nighttime 4.3- μm earthlimb our analysis of the SPIRE data in section 2.4 above has shown that the transfer of energy from $\text{OH}(V > 0)$ is required to be included into CHARM in order to adequately model the data in the approximate altitude range 75 to 90 km. The analysis also indicates that another, as yet unidentified mechanism needs to be specified in order to account for the underprediction of SPIRE nighttime 4.3- μm data above approximately 90 km that we discussed in section 2.4 above.

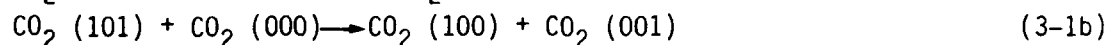
The version of CHARM that is described in the report by Humphrey et al. (1981) does not include the "weak" bands 2 through 8 that we have presented in Table 2-3 above. However, we have shown in section 2.3 above that these bands are major contributors to both the day and nighttime 4.3- μm earthlimb in the altitude region from approximately 60 to 105 km and are required to achieve an accurate model of the 4.3- μm SPIRE data. Hence an improved and realistic version of the CHARM should include these bands. The analysis also shows that a larger number of bands than presently included in CHARM should in fact be included in order to adequately model the 15- μm earthlimb. Likewise Sharma has shown by analysis of the SPIRE 2.7- μm data that the bands which account for the fluorescence of sunlight at 2.0 and 1.6 μm should be included in the CHARM in order to adequately model the day time 2.7- μm SPIRE data. Finally, bands of the minor isotopic species of CO_2 have been shown to be required in all three regions of the SPIRE data that we have subjected to detailed analysis, namely 15, 4.3, and 2.7 μm .

In this section we have summarized a number of aspects of the CHARM that the SPIRE data, and the analysis thereof, show require improvement. By the time our report is published we would expect that some of these deficiencies would have been corrected in the CHARM.

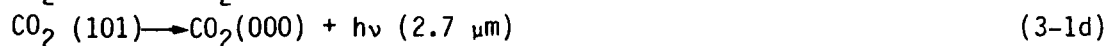
Section 3
LABORATORY STUDY OF CO₂ FLUORESCENCE

3.1 EXPERIMENTAL OBJECTIVES AND APPROACH

During the time period covered in this report we undertook a number of experiments aimed at studying the processes:



and



The primary goal of these experiments was to obtain experimental values for the branching ratio which described what fraction of CO₂ in the 101 level decayed via process (3-1e) (emission at 4.3 μm) as compared with process (3-1d) (emission at 2.7 μm).

The approach was to produce molecules in the 101 level via process (3-1a) by using a tunable 2.7 μm laser to excite the CO₂. By comparison of the relative intensity of emission at 4.3 μm and 2.7 μm the branching ratio can be determined.

There are a number of factors which complicate these measurements and which make the use of a pulsed laser a desirable technique for obtaining the desired results.

In the absence of any emission measurements it would be expected that the branching ratio could be calculated from known values of the absorption band strengths for the 4.3 μm band and the 2.7 μm band. While this is true, there are a number of reasons for testing an emission measurement aside from the value

of having a direct confirmation of the branching ratio to compare with the calculated ratio. The branching ratio is affected by many collisional processes which result in a transfer of the initial vibrational excitation to other molecules or else cause a redistribution of that energy among various vibrational modes.

Depending on the number of densities of the colliding partners, many of these processes occur on time scales smaller than the radiative lifetime. As a result, the actual branching ratios obtained under a given set of conditions may differ considerably from the values expected for the isolated molecules in a hypothetical collision free environment.

The single most important process which affects the laboratory measurements and leads to considerable difficulty in the measurement is process (3-1b) (the sharing of the excitation between two molecules as a result of collision of excited CO_2 with CO_2 in the ground state). While for the isolated molecules the lifetime for radiating at $2.7 \mu\text{m}$ is longer than that corresponding to $4.3 \mu\text{m}$, it turns out that the exchange shown in (3-1b) occurs with such a high efficiency that any $2.7 \mu\text{m}$ radiation is quenched at a rate fast compared to emission at $4.3 \mu\text{m}$. This requires that the $2.7 \mu\text{m}$ measurement be made on a time scale which is much smaller than that required at $4.3 \mu\text{m}$. The emission at $4.3 \mu\text{m}$ is not affected by this because emission at $4.3 \mu\text{m}$ from the states (101) and (001) presumably takes place at the same rate and therefore process (3-1b) which redistributes the V_3 excitational energy should not affect the overall rate of emission at $4.3 \mu\text{m}$.

The rate constant for reaction (3-1b) is $1.3 \times 10^{-10} \text{ cm}^3 \text{ s}^{-1}$. (Finzi and Moore, 1975). Therefore at a pressure of the order of 10^{-2} torr, for example, the lifetime of the 101 level is of the order of $21 \mu\text{s}$, which is more than two orders of magnitude smaller than the $4.3 \mu\text{m}$ band radiative lifetime. This clearly points to the need to be able to measure the relative emission on a time scale much faster than required for pure radiative decay.

In actual measurements, a pressure of 10^{-2} torr would be unsuitable because under the conditions of our experiment which utilized a small fluorescence cell, the results would be effected by deactivation as a result of wall collisions. In our experiments we utilized CO_2 in the presence of 50 torr of Argon. Under these conditions the V_3 vibration responsible for 4.3 emission, is quenched with a lifetime of approximately 400 μs . Still, the 2.7 μm radiation is quenched by reaction 3-16 at a much more rapid rate even at CO_2 pressures as low as 10^{-2} torr.

The need for using a laser in order to study the branching ratio becomes apparent from the above considerations of the energy transfer process (3-1b). In order to have a reasonable rate for the transfer reaction, small number densities are required. At the small number densities, the use of a continuous source would not provide enough energy for easy measurement of the resultant signal. Thus a laser source which can provide large initial excitation of the (101) level is required. Furthermore, a pulsed laser is ideal because of the rapid decay of the (101) level following initial excitation.

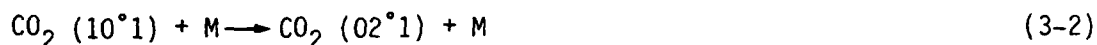
Previous preliminary experiments which are described in the final report "Fluorescence Experiment and Auroral Data Evaluation to Improve Prediction of Nuclear Atmosphere Infrared Background" DNA 4906F by Kumer and James had indicated that our chromatix laser which was tunable at 2.7 μm would be adequate for this purpose.

In the following section we describe our experimental effort and some of the modifications to our original experiments which were made in an attempt to overcome certain experimental difficulties. Prior to this discussion, however, we first give a brief summary of the types of measurements which we expect to be able to measure with a sufficiently stable pulsed laser source.

Equations (3-1a) through (3-1e) represent only a portion of the processes which are of importance in atmospheric applications. In addition to the band (101), there is another band which is excited by radiation near 2.7 μm . That

is the (02°1) band at 2.7 μm. Therefore all of the reactions shown in equations (3-1) will also occur with the (101) level replaced by the (02°1) band.

The levels (02°1) and (101) of CO₂ are quite closely spaced (about 100 cm⁻¹) and as a result can become equilibrated via collisions of the type:



Therefore any initial excitation of the 101 level should also result in the (02°1) level becoming populated. The rate constant for this reaction can be estimated as about $3 \times 10^{-11} \text{ cm}^3 \text{ s}^{-1}$ (Sharma, 1968) which is the value obtained for the corresponding reaction with $\nu_3 = 0$.

In our laboratory measurements with 50 torr of Argon present in the cell, this equilibration should occur on a time scale much faster than reaction (3-1b) so that regardless of whether the (10°1) band or the (02°1) band is excited, the emission observed near 2.7 μm will include the contributions of both bands:

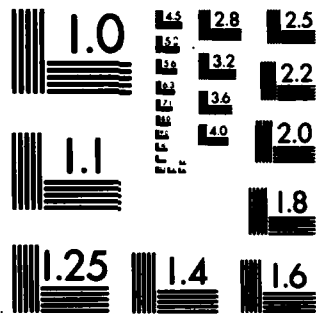


Also fluorescence near 4.3 μm will include bands

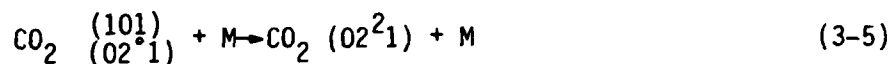


The reactions (3.2) would affect the branching ratio measurements in that the value obtained would represent an average value for the 2.7 μm and 2.77 μm bands.

In addition to the states (10°1) and (02°1) which are split by Fermi Resonance, there is another nearby state (02²1) which differs from (02°1) in having vibrational angular momentum. This Δ state with $\ell = 2$ would also be expected to be formed in collisions of the type.



MICROCOPY RESOLUTION TEST CHART
NATIONAL BUREAU OF STANDARDS-1963-A

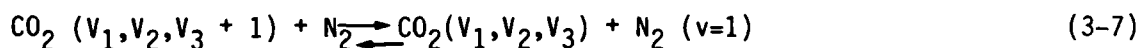


The state $(02^2 1)$ can still radiate at $4.3 \mu\text{m}$ to produce $(02^2 0)$; however, the transition



is forbidden with the result that process (3-5) would tend to reduce the intensity in the $2.7 \mu\text{m}$ region and also increase the apparent lifetime. This process would therefore affect the measured value of the branching ratio. The exact amount by which the branching ratio would be affected would depend on whether or not process (3-5), which involves a change $\Delta l = 2$, has the same rate constant as process (3-2). Later in this report we suggest ways in which this might be determined.

A major process affecting excited CO_2 in the atmosphere and one which can easily be studied in the laboratory is the transfer of excitation between CO_2 and N_2 according to:



This process of rapid sharing of vibrational excitation between CO_2 and N_2 affects the time dependence of the CO_2 emission in the atmosphere. In the laboratory, information concerning this ratio can be obtained from the study of the time dependence of the CO_2 emission as different amounts of N_2 are mixed with the CO_2 in the sample cell. Preliminary measurements involving this process are discussed later in this report.

3.2 SUMMARY OF EXPERIMENTAL MEASUREMENTS

In our report (DNA 4906F) we described preliminary measurements of the $4.3/2.7$ branching ratio in which a boxcar integrator was used to measure the $2.7 \mu\text{m}$ signal. One of the major difficulties encountered in these earlier measurements was the fact that there was a large scattered pulse from the $2.7 \mu\text{m}$ laser light used to excite CO_2 . In those earlier experiments the

preamplifier used to measure the scattered 2.7 μm light had a response time of the order of 10 microseconds. This resulted in a large wide ($>10\mu\text{s}$) pulse from the exciting laser light pulse which overlapped and masked the 2.7 μm reemission from CO_2 . When this signal was amplified it saturated the amplifier. To avoid this problem we worked at low CO_2 pressures (5×10^{-3} torr) to increase the lifetime of the 101 level and placed the boxcar window a long way away (70 μs) from the exciting pulse in order to eliminate the interference between this exciting line and the resonance fluorescence at 2.7 μm . The low pressures and the fact that we were many half-lives away from the peak of the fluorescence required sacrificing signal intensity.

In an attempt to remedy this situation we built an amplifier with a response of 1.5 μs , expecting that we could work at higher pressures with a corresponding increase in signal, and also separate the scattered pulse from the fluorescent pulse.

As it turned out, we continued to have problems with measuring the signal at 2.7 μm .

Our earlier experiments utilized a cylindrical fluorescence cell in which the two detectors (one for 4.3 μm and one for 2.7 μm fluorescence) viewed along the axis of the cylinder through two CaF_2 windows. A 2.7 μm filter was placed in front of one detector and a 4.3 μm filter was placed in front of the other. The 2.7 μm laser pulse was directed perpendicular to the axis through two windows which had been placed in holes drilled through the cylinder walls. In the earlier experiments the laser light made just one pass through the cell. The geometry of this is shown in Fig. 3-1. In order to enhance the signals we built a multiple pass cell by placing parallel mirrors inside the cell to give the geometry shown in Fig. 3-2. This cell design was chosen because it was one which would increase the number of passes without producing a significant loss in solid angle between the excitation region and the detectors. In most of our subsequent experiments the mirrors were positioned to give seven passes through the cell.

The large amplified scattered pulse originating from the exciting laser light continued to create problems with our electronics. This was due in part to saturation of electronics and equally as much due to the fact that our laser was extremely unstable. For each exciting pulse a corresponding fluorescence pulse as monitored by 4.3 μm fluorescence did not always occur. The 4.3 μm pulses which did occur were stored in a Tracor-Northern signal averager so that after a run of several minutes (with 5 laser pulses per second) the 4.3 μm signal was well defined. Since the signal at 2.7 μm always contained the effects of the tail of the 2.7 μm scattered laser exciting line plus (presumably) some occasional contribution from resonance fluorescence at 2.7 μm results obtained with the boxcar integrator were unstable.

During the course of several months we attempted a number of further modifications to our system in an attempt to overcome these difficulties. None of these were satisfactory in leading reproducible results for the ratio of signal strengths obtained in the 2.7 μm and 4.3 μm channels.

A brief summary of the types of modifications that we made is given in the following section.

Our first attempt to eliminate the problem arising from the scattering of the initial 2.7 μm laser pulse was to construct a differential amplifier and look directly at the initial exciting pulse and compare this with the 2.7 μm pulse of re-radiation scattered in the fluorescence cell. By adjusting the signal from those two sources we expected to have zero output from the differential amplifier when no fluorescence was taking place. When fluorescence did occur, we expected that the longer lived (longer than the initial excitation pulse) 2.7 μm fluorescence signal would appear at the output. Again this was not completely satisfactory because of saturation and corresponding long recovery times, also it was difficult to accurately match the signal from the two outputs of either differential amplifier.

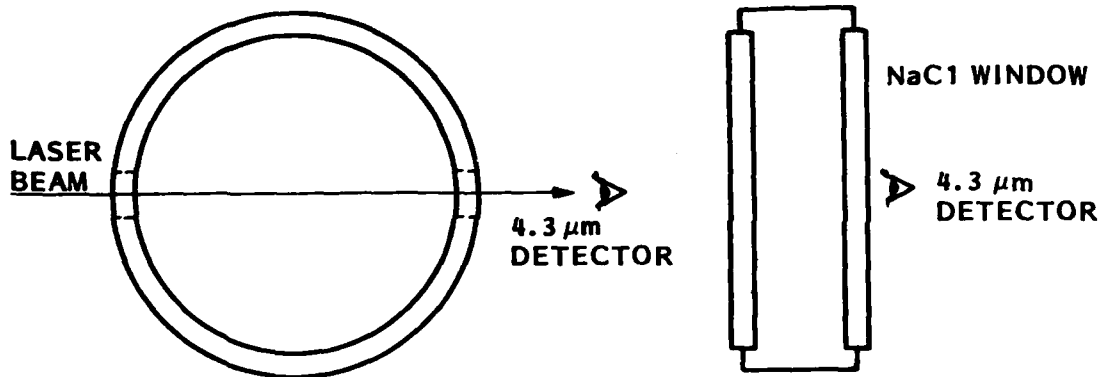


Fig. 3-1 Experimental Arrangement for Measurement of Fluorescence at 4.3 μm

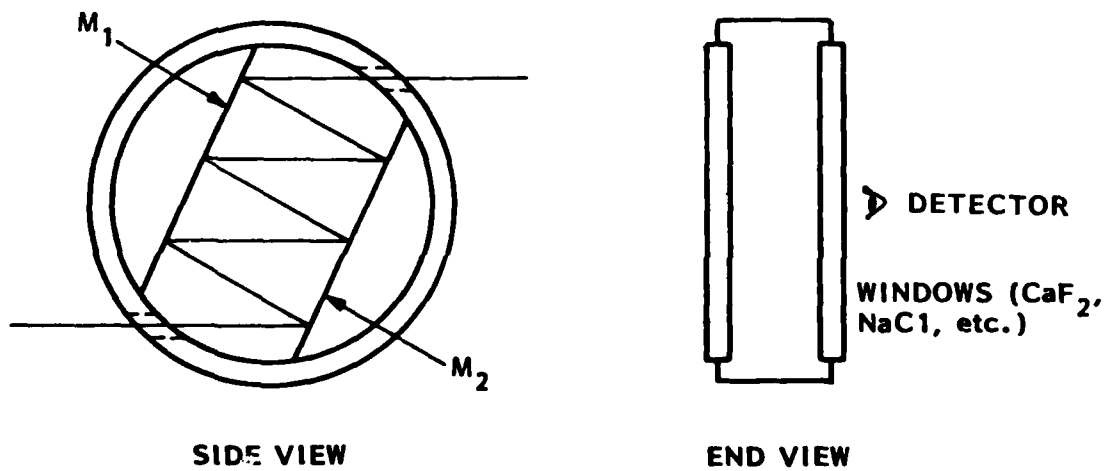


Fig. 3-2 Multiple Pass Cell

Continuing efforts involved rejecting the differential amplifier and using the actual 4.3 μm signal itself to trigger the signal averager and boxcar integrator which recorded the 4.3 μm fluorescence and 2.7 μm re-radiation. By using a voltage comparator we could trigger the signal averager and boxcar only when the fluorescence at 4.3 μm was greater than a preset value. Since we were not observing fluorescence with every pulse of the laser, this eliminated averaging scattered pulses at 2.7 μm which did not include a fluorescence component. It also served to improve signal to noise ratio in the 4.3 μm channel since pulses less than some pre-determined value were not included. Still we continued to have irreproducible results in the 2.7 μm channel.

Several further modifications included the use of fast switching whereby the signal at 2.7 μm was not admitted to the amplifying electronics until several microseconds after the initial pulse so as to eliminate saturation of electronics caused by this source. When these modifications failed to yield reproducible results we finally replaced the boxcar integrator which appeared to be unstable with an integrating circuit built specifically to cover the time intervals of interest for measuring fluorescence at 2.7 μm . A diagram of this configuration is shown in Fig. 3-3.

In spite of the numerous modifications to our system we were not able to obtain reproducible results for the branching ratio measurements. During the time period when these various modifications were being made we observed that the chromatix laser was quite erratic in its output and that this effect seemed to become worse as time went by.

In fact, we found on measuring the infrared output from the heated LiNbO_3 crystal that wavelength shifts of 100 or so wavenumbers would occur without any change in the control setting. In retrospect we realize that most of our earlier problems associated with trying to measure the 2.7 μm fluorescence were due to the fact that our laser was extremely unstable. When we realized that our laser was not putting out a constant frequency we returned the system to chromatix for repairs. As it turned out a transistor in the heater circuit

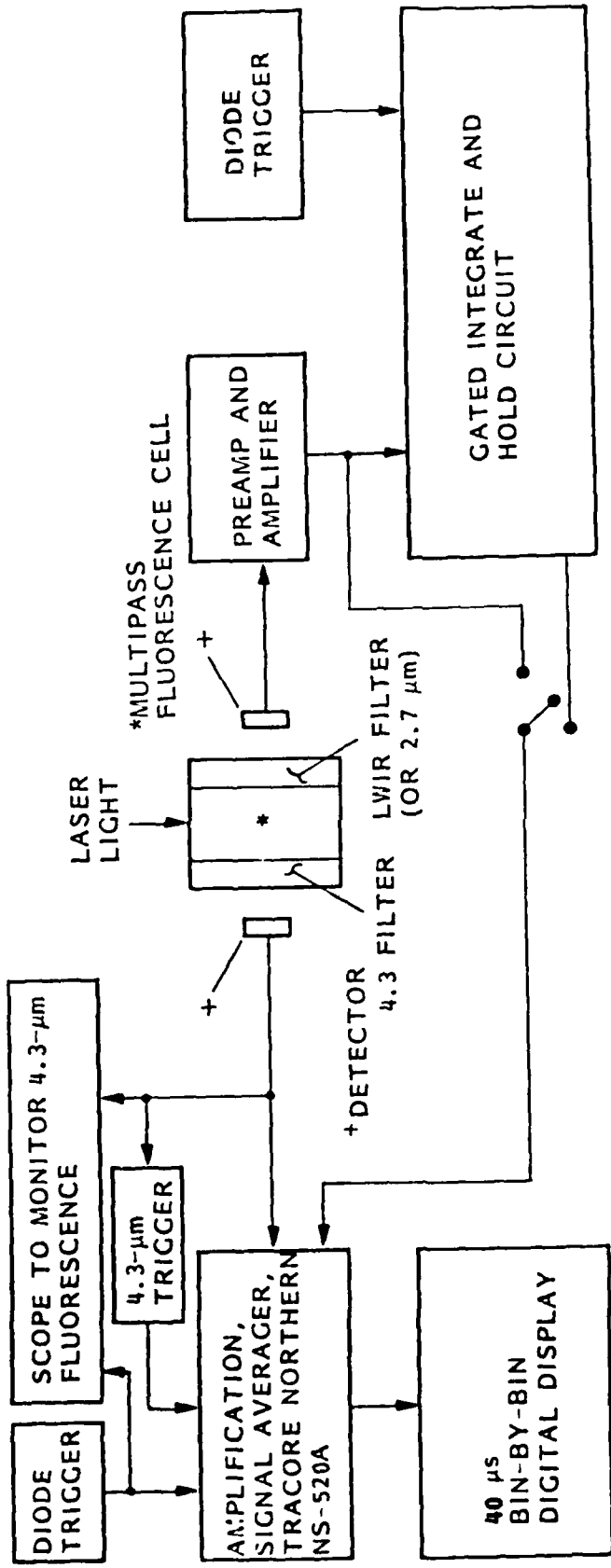


Fig. 3-3 Geometry and Electronics for Two-Channel Run

which maintained the LiNbO_3 crystal at a constant temperature had failed which ultimately resulted in fluctuations of many wavenumbers from day to day. In our earlier report, DNA 4906F, we had mentioned that the $2.7 \mu\text{m}$ filter placed in front of the detector rejected much of the exciting laser light but transmitted a significant portion of the 101 and 021 bands. Thus originally the interference of scattered laser light was not as damaging as it was in our later experiments, since in these later experiments the exciting $2.7 \mu\text{m}$ was changing in frequency from day to day by an amount sufficient to cause it to fall within the bandpass of the $2.7 \mu\text{m}$ filter at times.

The manufacturer's sales personnel had claimed that their dye laser plus associated optical parametric oscillator (heated LiNbO_3 crystal) would produce a wavelength stability of the order of 0.001 cm^{-1} over several hours. Our experience was that this was not the case based on the fact that there were pulse to pulse variations in the magnitude of the fluorescence observed at $4.3 \mu\text{m}$ and also because a considerable fraction (sometimes as much as 70 percent) of the exciting pulses did not result in any fluorescence at all.

In spite of the fact that we were unable to obtain reproducible signals at $2.7 \mu\text{m}$ we could collect many $4.3 \mu\text{m}$ fluorescent pulses and obtain a decay curve for $4.3 \mu\text{m}$ emission with good signal to noise. This was due to the fact that the $4.3 \mu\text{m}$ signal is more intense than the $2.7 \mu\text{m}$ signal and also because the $4.3 \mu\text{m}$ filter rejected scattering of the $2.7 \mu\text{m}$ exciting pulse so that there was not the problem of interference and saturation of electronics that we had experienced in the $2.7 \mu\text{m}$ channel.

3.3 RESULTS FOR VV BETWEEN $\text{N}_2(\text{V}=1)$ AND $^{13}\text{C}^{16}\text{O}_2$.

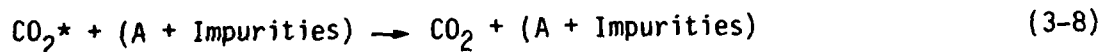
In our earlier report we examined the rate of reaction (3-7) involving the transfer of energy between CO_2 and N_2 . We obtained results which were in agreement with the literature value of $\sim 6 \times 10^{-13} \text{ cm}^3\text{sec}^{-1}$ for the rate constant. In our present set of experiments we were interested in comparing the rate of decay of $4.3 \mu\text{m}$ emission in the presence of N_2 for both

$^{12}\text{CO}_2$ and $^{13}\text{CO}_2$. K_{VV} measurement for reaction (3-7) is important for some of the minor isotopic species such as $^{13}\text{CO}_2$ for accurate predictions of the CO_2 4.3 μm relaxation time in the x-ray deposition region of the atmosphere near 80-km altitude. Kumer (1977b) has shown that the value of this relaxation time can vary between 7 and 20 minutes near 80 km depending on the values of k_{VV} for various weak isotopic CO_2 4.3 μm bands.

We made several measurements of the quenching of $^{12}\text{CO}_2$ and $^{13}\text{CO}_2$ by argon and nitrogen. The purpose of these measurements was to measure the difference in the transfer rate for the exchange of vibrational energy between CO_2 and N_2 for the different isotopic species of CO_2 . There was some problem with the experimental data in that the quenching rates appeared to be much faster than our expectations for both cases. In the case of a measurement of the quenching of CO_2 by argon with no nitrogen present, we obtained a value greater than the known rate. We obtained a lifetime for the excited CO_2 of 156 μs whereas the expected value under our experimental conditions should have been about 400 μs (Yardley and Moore 1968). This suggests that there was probably some source of contamination in the laboratory sample cell which was resulting in a faster quenching rate and a corresponding decrease in the lifetime of CO_2 .

In spite of this apparent discrepancy we have attempted to make some estimates as to the relative quenching rates of $^{12}\text{CO}_2$ and $^{13}\text{CO}_2$ by N_2 . To make this comparison we have assumed that in all of our quenching runs, which used the same amount of Argon, that the same quenching rate of 156 μs would have been obtained in the absence of N_2 . What this amounts to is the assumption that the impurities which must have been present were constant for all of the runs. Based on this assumption, we have then compared the $^{12}\text{CO}_2$ and $^{13}\text{CO}_2$ results. To make this comparison we have calculated curves of the emission rate as a function of time for various values of the N_2 transfer rate.

Given that in the presence of argon for our experimental conditions, the excited CO_2^* appears to have a lifetime of 156 μs , we have:



$$-d(\text{CO}_2^*)/dt = (\text{CO}_2^*) K \quad (3-9)$$

where

$$K = 1/\tau = 6410 \text{ s}^{-1}$$

In addition to this process, the excited CO_2^* participates in the energy exchange process:



From this process we have:

$$-d(\text{CO}_2^*)/dt = k_f(\text{CO}_2^*)(\text{N}_2) - k_r(\text{CO}_2)(\text{N}_2^*)$$

and

$$-d(\text{N}_2^*)/dt = k_r(\text{CO}_2)(\text{N}_2^*) - k_v(\text{CO}_2^*)(\text{N}_2)$$

In our experiments we had $(\text{CO}_2) = (\text{N}_2)$. If we make a simplifying assumption that $k_f = k_r$ because of the near resonant transfer, then we have:

$$\begin{aligned} -d(\text{CO}_2^*)/dt &= k(\text{CO}_2^*) - k(\text{N}_2^*) + K(\text{CO}_2^*) \\ -d(\text{N}_2^*)/dt &= k(\text{N}_2^*) - k(\text{CO}_2^*) \end{aligned} \quad (3-12)$$

where k is now given by:

$$k \cong k_f(N_2) \cong k_r(CO_2) \quad (3-13)$$

In the case of $^{12}CO_2$, the measured value of k_f is reported to be $6 \times 10^{-13} \text{cm}^3 \text{s}^{-1}$ (Taylor and Bitterman 1964). Therefore since for our experiments $(CO_2) = 0.3 \text{ torr}$, we expect a transfer rate of $k = 6,371 \text{ s}^{-1}$.

The solution of Eqs. (3-9) and (3-12) subject to the condition that at time $t = 0$ that $(N_2^*) = 0$ is:

$$(CO_2^*) = (CO_2^*)_{t=0} \frac{e^{-Kt/2}}{2\sqrt{\chi}} \left[(\sqrt{\chi} - k) e^{-\left(\frac{\sqrt{\chi}}{2} - k\right)t} + (\sqrt{\chi} + k) e^{-\left(\frac{\sqrt{\chi}}{2} + k\right)t} \right] \quad (3-14)$$

where

$$\sqrt{\chi} = \sqrt{K^2 + 4k^2}$$

In Fig. (3-4) and (3-5) we show calculated curves of the rate of emission of $4.3 \mu\text{m}$ radiation from excited CO_2^* as a function of time. These curves are calculated for a value of K given by Eq. (3-9) and various values of k of Eq. (3-13). The experimental results are then superimposed on these curves in order to determine the value of k which seems to give the best fit of the data. From Fig. (3-4) it is seen that the data appears to agree best with a value of $k = 6,371 \text{ s}^{-1}$ in agreement with our expectation for $^{12}CO_2$. In the case of Fig. (3-5), some of the data appears to lie closer to the curve with $k = 3186 \text{ s}^{-1}$ whereas one of the runs was a better match with the $k = 1,593 \text{ s}^{-1}$.

From the comparison given above, it appears likely that the rate of exchange of vibrational energy between CO_2 and N_2 slower by a factor of 2 or 3 for $^{13}CO_2$ as compared with $^{12}CO_2$. Unfortunately we cannot place a high degree of certainty on these results due to the fact that we know from our

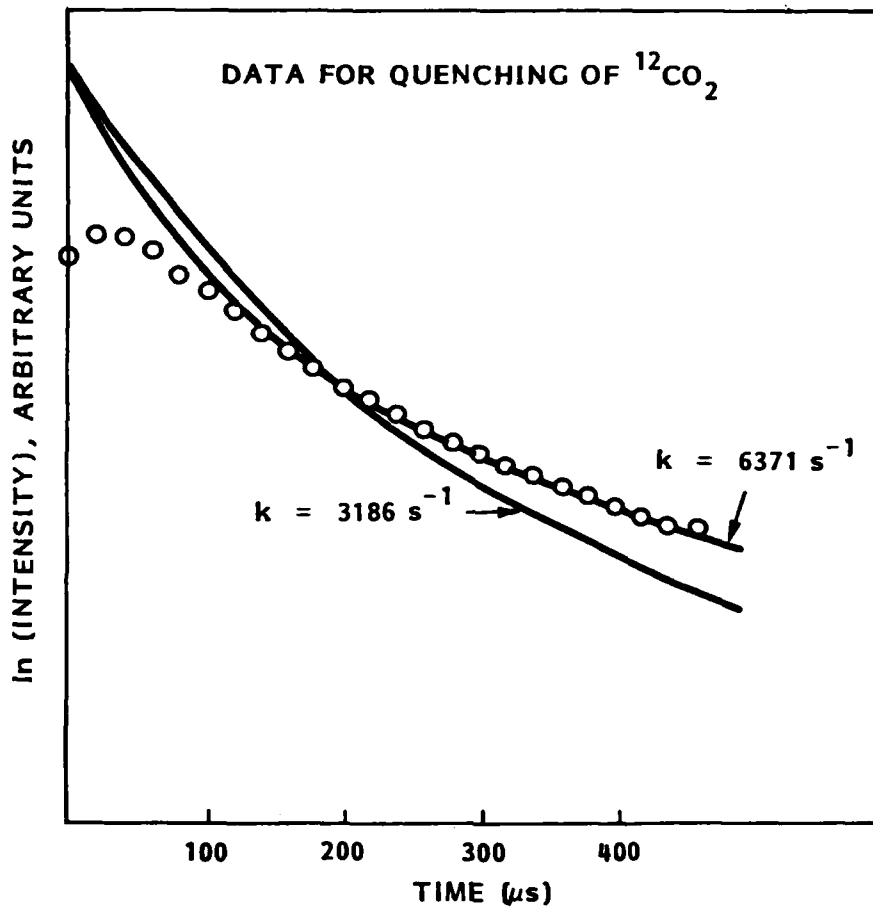


Fig. 3-4 Plot of the Rate of Emission of $4.3 \mu\text{m}$ Radiation as a Function of Time. The Solid Lines are Calculated from Eq. (7). The Circles Represent Experimental Data from Two Runs.

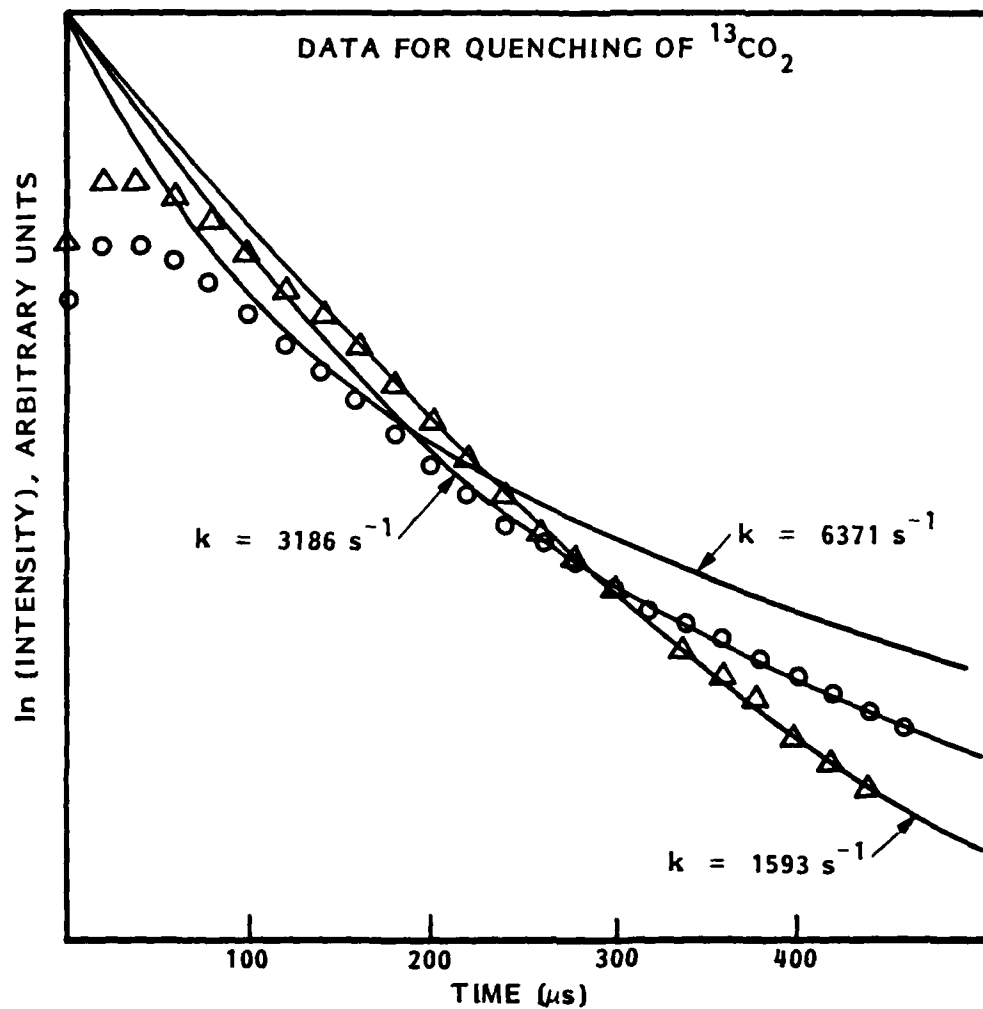


Fig. 3-5 Plot of the emission of $4.3 \mu\text{m}$ radiation as a function of time. The solid lines are calculated from Eq. (7). The Circles and Triangles Represent Experimental Data From Different Runs.

results with pure Argon that there must be some impurities in the system. Also this comparison does not adequately analyze the departure of the experimental results from the calculated curves at small times. This is presumably related to the overall temporal response of the electronic recording systems.

3.4 CONCLUSIONS AND SUGGESTIONS FOR FUTURE STUDIES

Our laboratory studies of the Fluorescence of CO_2 at $4.3 \mu\text{m}$ when excited by a $2.7 \mu\text{m}$ laser pulse have pointed to a number of useful studies which can be made using this technique. Our experience also points to a number of problems which can arise in studies of this type. In our attempts at measuring the branching ratio for decay of levels such as (101) via $4.3 \mu\text{m}$ emission and re-emission at $2.7 \mu\text{m}$ we encountered many problems associated with the need to separate the initial scattered $2.7 \mu\text{m}$ pulse from $2.7 \mu\text{m}$ resonance fluorescence following this excitation pulse. By suitable choice of infrared filters to isolate the $2.7 \mu\text{m}$ laser pulse from most of the reemitted fluorescence and fast electronics that would rapidly recover from a large burst of scattered $2.7 \mu\text{m}$ radiation, this separation should be achievable. Our efforts to do this were unsatisfactory because of the instability of our laser at $2.7 \mu\text{m}$. The initial exciting pulse at $2.7 \mu\text{m}$ did not always occur at the same wavelength which made it difficult to separate the $2.7 \mu\text{m}$ scattered pulse from subsequent resonance fluorescence at $2.7 \mu\text{m}$. Any attempts in the future to study the branching ration would have to be aware of this problem and we would stress the need for a stable $2.7 \mu\text{m}$ laser pulse which could be tuned to a wavelength in the $2.7 \mu\text{m}$ bands which could be isolated from much of the subsequent band emission via sharp cutoff infrared filters.

The study of $4.3 \mu\text{m}$ emission produced via reactions such as (3-1a) and (3-1b) is much simpler due to the fact that interference from the $2.7 \mu\text{m}$ laser pulse is not a problem. From a study of the time dependence of the decay of emission at $4.3 \mu\text{m}$ information can be gained concerning the quenching of the (001) level by various species and also the rate of transfer of energy between excited CO_2 and other species such as N_2 . In order to obtain accurate

results for rate constants from studies of this type it is necessary to have precise capability of measuring pressures and mixing ratios of gases in the pressure ranges from several microns to several torr. Contamination by small amounts of unwanted gases can completely destroy a set of measurements.

Earlier in this report we have mentioned that the initial excitation of the levels (101) and (02[°]1) results in population of the levels (100) and (02[°]0) as a result of 4.3 μm emission and also as a result of transfer of ν_3 excitation between excited and ground state CO_2 . In addition to these levels the level (02²0) is also expected to be formed because of collisions such as shown in Eq. (3-5) followed by 4.3 μm emission and also by similar collisions involving (100) and (02[°]0) with various collision partners. These processes should result in non-LTE populations of levels (100), (02[°]0), and (02²0) with resultant fluorescent pulses at 13.8 μm , 16.2 μm , and 14.98 μm as these states radiatively decay to the (01¹0) level.

A study of the relative intensity and time dependence of the emission from these three hands should provide information on the rate at which energy is redistributed between these various levels. The band at 14.98 μm is closely intermixed with the (01¹0) (000) band at 15 mm so that it will be more difficult to study than the 13.8 and 16.2 μm bands. It may prove feasible to isolate selected lines in the 14.98 μm band by a suitable etalon.

Alternatively, a filter consisting of CO_2 in an absorption cell may prove useful in distinguishing between radiation from the (02²0) (01¹0) band and the (01¹0) (000) band.

Based on our experience with the Chromatix laser which did not perform according to the manufacturer's specifications we would caution those interested in pursuing investigations of this type to make certain that they have a stable laser source which has a constant unchanging wavelength.

A pulsed laser at 2.7 μm does provide an excellent method for studying many fluorescent processes and related collisional quenching and energy transfer processes in CO_2 which are of importance in relation to the atmospheric radiance backgrounds occurring at many infrared wavelengths.

REFERENCES

4.0 REFERENCES

Abramowitz and Stegun, Handbook of Mathematical Functions, U. S. Dept. of Commerce, U.S. Printing Office, Washington, D.C., 1966.

Allen, D. C., T. Scragg, and C. J. S. M. Simpson, "Low Temperature Fluorescence Studies of the Deactivation of the Bend-Stretch Manifold of CO₂, Chem. Phys. (Netherlands) 51, No. 3, 279, 1980.

Caledonia, G. E.; B. D. Green and R. E. Murphy, "On the Self-Trapping of CO₂ Fluorescence, J. Chem. Phys., 77(10), 5247, 1982.

Degges, T. C., "Results for the Contribution of Resonance Scattering of Sunlight by H₂O to the Sunlit 2.7 μm earthlimb," presented at the DNA/RAEE Review Meeting held at DNA on 13-17 July, 1981.

Faire, A. C. and E. A. Murphy, "Neutral Density and Temperature Measurements," appears in Proceedings of COSPAR Symposium on Solar Particle Event of November 1969, Tech. Report AFCRL-72-04-74, edited by J. C. Ulwick, 1972.

Finzi, J. and C. B. Moore, J. Chem. Phys., 63, 2285 (1975).

Hays, P. B. and J. J. Olivero, "CO₂ Above the Troposphere," Planet. Space Sci., 18, 1729, 1970.

Hines, C. O., "Internal Atmospheric Gravity Waves at Ionospheric Heights," Can. J. Phys., 38, 1441, 1960.

Humphrey, C. H., R. M. Nadile, C. R. Phillbrick, D. R. Smith, T. C. Degges, S. M. Silverman, T. F. Tuan, and J. B. Kumer, "Atmospheric Infrared Variability, AFGL-TR-81-0207, edited by C. H. Humphrey, R. M. Nadile, C. R. Phillbrick, and D. R. Smith, 27 May 1981.

James, T. C. and J. B. Kumer, "Fluorescence of CO_2 Near $4.3 \mu\text{m}$; Application to Daytime Limb Radiance Calculations," J. Geophys. Res., 78, 8320, 1973.

Kumer, J. B., "Atmospheric CO_2 and N_2 Vibrational Temperatures at 40 to 140 km Altitude," J. Geophys. Res., 82, 2195, 1977a.

Kumer, J. B., "The $4.3 \mu\text{m}$ CO_2 Aurora and Related Phenomena," J. Geophys. Res., Vol. 82, 1977b, p. 2203.

Kumer, J. B., "Analysis of Non-LTE CO_2 SPIRE Earthlimb Data," paper AIAA-81-0425 presented at the AIAA 19th Aerospace Science Meeting, Jan 15, 1981.

Kumer, J. B. and T. C. James, " CO_2 (001) and N_2 Vibrational Temperatures in the $50 \leq z \leq 130$ km Altitude Range," J. Geophys. Res., 79, 638, 1974.

Kumer, J. B., A. T. Stair, Jr., N. B. Wheeler, K. D. Baker, and D. J. Baker, "Evidence for an $\text{OH}(\nu) \nu \nu \text{N}_2(\nu) \nu \nu \text{CO}_2(\nu_3) \rightarrow \text{CO}_2 + h\nu$ ($4.3 \mu\text{m}$) Mechanism for $4.3 \mu\text{m}$ Airglow," J. Geophys. Res., 83, 4743, 1978.

Nadile, R. M., 'SPIRE,' Presentation material from the Proceedings of the Second DNA Infrared Data Review Meeting, which was held 10-12 April 1979 at the Air Force Geophysics Laboratory, collected in the technical memorandum AFGL-TM-18, 1979.

Nadile, B. M. and W. Grieder, private communication, 1980.

Noxon, J. F., "Effects of Internal Gravity Waves Upon Night Airglow Temperatures," Geophys. Res. Lett. 5, 25, 1978.

Neuendorffer, A. C., "The Convolution-Modeling Approach to Infrared Atmospheric Line Absorption," Draft NOAA NESS report kindly supplied to us in Jan 1982.

Patterson, A. W., "Airglow Events Visible to the Naked Eye," Applied Optics, 18, 3390, Oct 15, 1979.

Simpson, C. J. S. M., private communications, 1980.

Rogers, J. W., A. T. Stair, Jr., N. B. Wheeler, C. L. Wyatt, and D. J. Baker, "LWIR (7-24 μm) Measurements From the Launch of a Rocketborne Spectrometer Into an Aurora (1973)," AFGL-TR-76-0274, 1976.

Rogers, J. W., A. T. Stair, Jr., N. B. Wheeler, C. L. Wyatt, and D. J. Baker, "LWIR (7-24 μm) Measurements From the Launch of a Rocketborne Spectrometer into a Quiet Atmosphere," AFGL-TR-77-0113, 1977.

Sharma, R., J. Chem. Phys., 49, 5195 (1968).

Sharma, R. and R. M. Nadile, "Carbon Dioxide (ν_2) Radiance Results Using a New Nonequilibrium Model," paper presented at DNA-AFGL Nuclear Weapon Effects Chemistry Conference, AFGL, Bedford, Mass., Jun 26 and 27, 1980.

Sharma, R. and R. M. Nadile, "Carbon Dioxide (ν_2) Radiance Results Using a New Nonequilibrium Model," paper AIAA-81-0426 presented at AIAA 19th Aerospace Meeting in St. Louis, Jan 15, 1981a.

Sharma, R. and R. M. Nadile, "Earthlimb Emission Analysis of SPIRE Data at 2.7 Micrometers," paper 304-17 presented at the 25th Annual SPIE International Technical Symposium and Exhibit, held in San Diego, Aug 22-28, 1981b.

Taylor, R. L., "Energy Transfer Processes in the Stratosphere," Can. J. Chem., 52, 1436, 1974.

Taylor, R. L., and Bitterman, Rev. Mod. Phys., 41, 26 (1964).

Weinreb, M. P., private communication, 1982.

Yardley, J. T. and C. B. Moore, J. Chem. Phys., 45, 1066 (1968).

DISTRIBUTION LIST

DEPARTMENT OF DEFENSE

Assistant to the Secretary of Defense, Atomic Energy
ATTN: Executive Asst

Defense Nuclear Agency
ATTN: RAAE, H. Fitz, Jr
ATTN: RAAE, W. McKechney
ATTN: RAAE, P. Lunn
4 cy ATTN: TITL

Defense Tech Info Ctr
12 cy ATTN: DD

Field Command
Defense Nuclear Agency, Det 1
Lawrence Livermore Lab
ATTN: FC-1

Field Command
Defense Nuclear Agency
ATTN: FCTT, W. Summa

Under Secretary of Defense for Rsch & Engrg
ATTN: Defensive Systems
ATTN: Strategic & Space Sys (OS)
ATTN: Strat & Theater Nuc Forces, B. Stephan

DEPARTMENT OF THE ARMY

US Army Electronics R&D Cmd
3 cy ATTN: DELAS-EO, F. Niles

BMD Advanced Technology Ctr
ATTN: ATC-O, W. Davies
ATTN: ATC-T, M. Capps

BMD Systems Cmd
2 cy ATTN: BMDSC-HW

Deputy Chief of Staff for Rsch Dev & Acq
ATTN: DAMA-CSS-N

US Army Ballistic Rsch Labs
ATTN: DRDAR-BLB, J. Mester
ATTN: DRDAR-BLA-S

US Army Combat Surv & Target Acq Lab
ATTN: DELCS-K, S. Kronenberg

US Army Foreign Science & Tech Ctr
ATTN: DRXST-SD

US Army Nuclear & Chemical Agency
ATTN: Library

US Army Research Ofc
ATTN: R. Mace

DEPARTMENT OF THE NAVY

Naval Electronics Systems Cmd
ATTN: PME 117-20

Naval Intelligence Support Ctr
ATTN: Doc Con

DEPARTMENT OF THE NAVY (Continued)

Naval Postgraduate School
ATTN: Code 1424, Library

Naval Rsch Lab
ATTN: Code 2627
ATTN: Code 6780, J. Fedder
ATTN: Code 2000, J. Brown
ATTN: Code 4239, D. McNutt
ATTN: Code 4128.2 J. Johnson
ATTN: Code 4700.1, W. Ali
ATTN: Code 6700, T. Coffey
ATTN: Code 4780, D. Strobel
ATTN: Code 4720, J. Davis
ATTN: Code 4780, S. Ossakow

Naval Surface Weapons Ctr
ATTN: Code F31
ATTN: Code X211

DEPARTMENT OF THE AIR FORCE

Air Force Geophysics Lab
ATTN: LKO, R. Huffman
2 cy ATTN: LKB, K. Champion
2 cy ATTN: LKD, R. Narcisi
2 cy ATTN: OPR, R. Nadille
2 cy ATTN: OPR, R. Murphey
4 cy ATTN: CA, A. Stair

Air Force Ofc of Scientific Rsch
ATTN: AFOSR/NC

Headquarters
Air Force Systems Cmd
ATTN: SDR
ATTN: DLTW
ATTN: DLXP
ATTN: OLS
ATTN: DLAE

Air Force Tech Applications Ctr
ATTN: TD
ATTN: TF
ATTN: Tech Library

Air Force Weapons Lab
ATTN: SUL

Air University Library
ATTN: AUL-LSE

Deputy Chief of Staff
Rsch, Dev & Acq
3 cy ATTN: AFRDS, Space Sys & C3 Dir

Rome Air Dev Ctr
ATTN: OCD, J. Simons

Space Div
ATTN: WE
ATTN: YGD
ATTN: YN, P. Sivgals

DEPARTMENT OF ENERGY

Department of Energy
Office of Military Application
ATTN: OMA, DP-22

OTHER GOVERNMENT AGENCIES

Central Intelligence Agency
ATTN: OSWR/NED

Department of Commerce
National Bureau of Standards
ATTN: A. Phelps

Department of Commerce
National Bureau of Standards
ATTN: Sec Ofc for S. Abramowitz
ATTN: Sec Ofc for R. Levine
ATTN: Sec Ofc for M. Krauss
ATTN: Sec Ofc for J. Devoe

Department of Commerce
National Oceanic & Atmospheric Admin
3 cy ATTN: F. Fehsenfeld
3 cy ATTN: E. Ferguson

Institute for Telecommunications Sciences
ATTN: W. Utlaut
ATTN: G. Falcon

NASA
ATTN: Code 6801, A. Tempkin
ATTN: Tech Library
ATTN: Code 900, J. Siry
3 cy ATTN: A. Aiken

NASA
ATTN: N. Stone
ATTN: W. Roberts
ATTN: J. Watts

NASA
ATTN: MS-168, C. Schexnayder

NASA
ATTN: N-245-3, R. Whitten

NASA
ATTN: J. Gray

NASA Headquarters
ATTN: I. Schardt, Code EE

OTHER AGENCY

Government Publications Library-M
ATTN: J. Winkler

DEPARTMENT OF ENERGY CONTRACTORS

University of California
Lawrence Livermore National Lab
ATTN: L-71, J. Chang
ATTN: L-262, D. Wuebbles
ATTN: L-10, H. Kruger
ATTN: L-48, E. Woodward
ATTN: L-325, G. Haugan

DEPARTMENT OF ENERGY CONTRACTORS (Continued)

Los Alamos National Lab
ATTN: MS670, J. Hopkins
ATTN: Librarian
ATTN: G. Smith
ATTN: MS362, Library
ATTN: R. Jeffries

Sandia National Labs
ATTN: T. Cook

Sandia National Labs
ATTN: Tech Library, 3141
ATTN: M. Kramm
ATTN: ORG 1250, W. Brown
ATTN: L. Anderson

DEPARTMENT OF DEFENSE CONTRACTORS

Aero-Chem Research Labs, Inc
ATTN: A. Fontijn

Aerodyne Research, Inc
ATTN: C. Kolb
ATTN: M. Camac

Aerospace Corp
ATTN: N. Cohen
ATTN: V. Josephson
ATTN: I. Garfunkel
ATTN: J. Reinheimer
ATTN: J. Straus
ATTN: T. Widhoph
ATTN: H. Mayer

AVCO Everett Research Lab, Inc
ATTN: A830
ATTN: C. Von Rosenberg, Jr
ATTN: Tech Library

Battelle Memorial Institute
ATTN: H. Lamuth
ATTN: Stolac
ATTN: R. Thatcher

Berkeley Rsch Assoc, Inc
ATTN: J. Workman

Boston College
ATTN: E. Heglom
ATTN: W. Greider

The Trustees of Boston College
2 cy ATTN: Chairman Dept of Chemistry
2 cy ATTN: Chairman Dept of Physics

University of California at Riverside
ATTN: J. Pitts, Jr

California Institute of Technology
ATTN: J. Ajello

Calspan Corp
ATTN: M. Dunn
ATTN: J. Grace
ATTN: C. Treanor
ATTN: W. Wurster

DEPARTMENT OF DEFENSE CONTRACTORS (Continued)

University of Colorado
ATTN: C. Lineberger-JILA
ATTN: G. Lawrence-LASP

Columbia University
ATTN: Security Officer for H. Foley

Computer Sciences Corp
ATTN: F. Eisenbarth

Concord Sciences
ATTN: E. Sutton

Cornell University
ATTN: M. Kelly

University of Denver
ATTN: Sec Officer for D. Murcray

University of Denver
ATTN: B. Van Zyl

Environmental Rsch Inst of Michigan
ATTN: IRIA, Library

EOS Technologies, Inc
ATTN: B. Gabbard

General Electric Co
ATTN: R. Edsall
ATTN: P. Zavitsanos

General Research Corp
ATTN: J. Ise, Jr

Geo Ctrs, Inc
ATTN: E. Marram

Institute for Defense Analyses
ATTN: H. Wolfhard
ATTN: E. Bauer

Kaman Sciences Corp
ATTN: J. Jordano

Kaman Sciences Corp
ATTN: T. Stephens

Kaman Tempo
ATTN: B. Gambill
ATTN: J. Devore
ATTN: K. Schwartz
5 cy ATTN: DASIAC

Kaman Tempo
ATTN: DASIAC

Lockheed Missilies & Space Co, Inc
ATTN: B. McCormac
ATTN: M. Walt
ATTN: J. Cladis
ATTN: J. Reagan
ATTN: J. Perez
ATTN: R. Sears
4 cy ATTN: J. Kumer

DEPARTMENT OF DEFENSE CONTRACTORS (Continued)

University of Lowell
ATTN: G. Best

Mission Research Corp
ATTN: M. Scheibe
ATTN: D. Archer
ATTN: F. Guigliano
ATTN: P. Fischer
5 cy ATTN: Tech Library

Lockheed Missiles & Space Co, Inc
ATTN: D. Davis

Pacific-Sierra Research Corp
ATTN: H. Brode, Chairman SAGE

PhotoMetrics, Inc
ATTN: I. Kofsky

Physical Dynamics, Inc
ATTN: A. Thompson

Physical Science Lab
ATTN: W. Berning

Physical Sciences, Inc
ATTN: R. Taylor
ATTN: K. Wray
ATTN: G. Calendoncia

Physics International Co
ATTN: Tech Library

University of the Commonwealth, Pittsburgh
ATTN: F. Kaufman
ATTN: M. Biondi
ATTN: W. Fite

Princeton University
ATTN: Librarian

R & D Associates
ATTN: F. Gilmore
ATTN: R. Turco
ATTN: R. Lindgren
ATTN: H. Ory
ATTN: P. Haas

R & D Associates
ATTN: B. Yoon
ATTN: J. Rosengren

Rand Corp
ATTN: P. Davis
ATTN: C. Crain

Rand Corp
ATTN: B. Bennett

Science Applications, Inc
ATTN: D. Sachs
ATTN: D. Hamlin

Space Data Corp
ATTN: S. Fisher

DEPARTMENT OF DEFENSE CONTRACTORS (Continued)

Spectral Sciences, Inc
ATTN: F. Bein

SRI International
ATTN: D. McDaniels
ATTN: W. Chesnut
ATTN: M. Baron
ATTN: R. Leadabrand
ATTN: J. Casper

SRI International
ATTN: C. Hulbert

Stewart Radiance Lab
ATTN: R. Huppi

Teledyne Brown Engrg
ATTN: MS-12, Tech Library
ATTN: F. Leopard
ATTN: N. Passino

Lockheed Missiles & Space Co, Inc
4 cy ATTN: T. James

DEPARTMENT OF DEFENSE CONTRACTORS (Continued)

Technology International Corp
ATTN: W. Boquist

Utah State University
Attention Sec Con Ofc for
ATTN: C. Wyatt
ATTN: D. Baker
ATTN: A. Steed
ATTN: K. Baker, Dir Atmos & Space Sci

VisiDyne, Inc
ATTN: W. Reidy
ATTN: C. Humphrey
ATTN: T. Degges
ATTN: H. Smith
ATTN: J. Carpenter

Wayne State University
ATTN: R. Kummier

Wayne State University
ATTN: W. Kauppila